Model for Predicting Creep of Cracked Steel Fibre Reinforced Concrete

by

Leo Mallett Pike

Thesis presented in partial fulfilment of the requirements for the degree of Master of Engineering in Civil Engineering in the Faculty of Engineering at Stellenbosch University

Department of Structural Engineering,

University of Stellenbosch,

Private Bag X1, Matieland 7602, South Africa.

Supervised by:

Prof. William Peter Boshoff

March 2018

Declaration

By submitting this dissertation electronically, I declare that the entirety of the work contained therein is my own, original work, that I am the sole author thereof (save to the extent explicitly otherwise stated), that reproduction and publication thereof by Stellenbosch University will not infringe any third party rights and that I have not previously in its entirety or in part submitted it for obtaining any qualification.

Signature: Leo Pike .....

Date: March 2018 .....

Abstract

The investigation of the creep of cracked fibre reinforced concrete has gained momentum over the past few years. However, there is still no proposed model of how to include the additional creep caused by the pull-out behaviour of fibres in the structural design of Steel Fibre Reinforced Concrete (SFRC) structures.

The purpose of this study was to create a preliminary design model that included this additional fibre pull-out behaviour. The Age Adjusted Effective Modulus (AAEM) method, used in the Fédération Internationale du Béton (*fib)* Model Code (2010), was used as a base model for predicting long-term deflections.

To reach this goal, time-dependent experimental investigations were performed at two levels, namely the macroscopic level and structural level. At the macroscopic level, uniaxial tensile creep tests were performed on cracked fibre reinforced specimens. At the structural level, flexural creep tests were performed on cracked reinforced concrete and SFRC beams, as well as cracked reinforced beams with a combination of fibres and steel bar reinforcing. This was performed to determine the experimental long-term deflections of each type of beam. A sustained stress level of 40% of the cracking tensile and flexural strengths was used.

The results of the uniaxial tensile creep tests were used to calculate the rate of fibre pull-out for the fibre reinforced specimens. These rates were used to calibrate an additional fibre pull-out factor that could be included in the AAEM method. A damage model for each beam type was developed to include the effect of pre-cracking. The long-term deflection results of the conventionally reinforced beams were used to verify the current *fib* Model Code's AAEM method. It was found that the adapted AAEM method could accurately predicted the long-term deflections of both cracked SFRC and combined reinforced beams.

Opsomming

Die ondersoek van die kruip van gekraakte veselversterkte beton het die afgelope paar jaar momentum gekry. Daar is egter steeds geen voorgestelde model oor hoe die addisionele kruip wat deur die vesels veroorsaak word, in die strukturele ontwerp van Staalvesel Versterkte Beton (SVVB) strukture ingesluit moet word nie.

Die doel van hierdie studie is om 'n voorlopige ontwerpmodel te skep wat hierdie addisionele veselkruip insluit. Die AAEM-metode (Age Adjusted Effective Modulus), wat in die *fib* Model Code 2010 gebruik word, is gebruik as basismodel vir die voorspelling van langtermyn-defleksie.

Om hierdie doel te bereik, is tydsafhanklike eksperimentele ondersoeke op twee vlakke uitgevoer, naamlik die makroskopiese vlak en strukturele vlak. Op makroskopiese vlak is eenassige trekkruip toetse op gekraakte veselversterkte proefstukke uitgevoer. Op strukturele vlak is buigtoetse op gekraakte gewapende beton- en SVVB-balke, sowel as gekraakte versterkte balke met 'n kombinasie van vesel- en staalstaafversterking, uitgevoer. Dit is uitgevoer om die eksperimentele langtermyn-defleksie van elke tipe balk te bepaal. ‘n Volgehoue belasting van 40% van die buigkraaksterkte is gebruik.

Die resultate van die eenassige trekkruip toetse is gebruik om die tempo van veseluittrekking vir die veselversterkte proefstukke te bereken. Hierdie is gebruik om 'n addisionele veseluittrekkingsfaktor te kalibreer wat by die AAEM-metode ingesluit kan word. ’n Skade-model is vir elke balk tipe ontwikkel om die effek van voorafkraking in te sluit. Die langtermyn-buigresultate van die konvensionele versterkte balke is gebruik om die huidige *fib* Model Code 2010 se AAEM-metode te verifieer. Daar is bevind dat die aangepaste AAEM-metode die langtermyn-defleksie van beide gekraakte SVVB en gekombineerde versterkte balke, akkuraat kon voorspel.

Acknowledgments

I would like to thank the following people for their guidance and support:

- Prof. W.P. Boshoff, my supervisor, for his mentorship throughout the course of this study.
- The Civil Engineering laboratory and workshop staff for their assistance.
- My family and friends, especially Nina Agnello, for their unwavering support and motivation throughout the course of this project.

.

Contents

List of Figures

List of Tables

Abbreviations

AAEM	Age Adjusted Effective Modulus
ASTM	American Section of the International Association for Testing Materials
BS	British Standards
CH	Calcium Hydroxide
CMOD	Crack Mouth Opening Displacement
CoV	Coefficient of Variation
EN	European Norms
fib	Fédération Internationale du Béton
FRC	Fibre Reinforced Concrete
HPFRC	High Performance Fibre Reinforced Concrete
ISO	International Organization for Standardisation
ITZ	Interfacial Transition Zone
LOP	Limit of Proportionality
LVDT	Linear Variable Displacement Transducer
NA	Neutral Axis
NC	Normal Concrete Mix, no Steel Fibres
RC	Reinforced Concrete
RH	Relative Humidity
SFRC	Steel Fibre Reinforced Concrete
SF30	Concrete Mix with a Steel Fibre Dosage of 30kg/m^3
SF60	Concrete Mix with a Steel Fibre Dosage of 60kg/m^3

Nomenclature

A_c	Cross-sectional Area of the Concrete
A_s	Cross-sectional Area of the Reinforcing Bar Steel
b	Width of the Beam Section
$CMOD_{e,s}$	Elastic Crack Mouth Opening Displacement due to Sustained Load
$CMOD_{fpc}$	Crack Mouth Opening Displacement due to Fibre Pull-out Creep
$CMOD_{max}$	Maximum Crack Mouth Opening Displacement due to Pre-cracking
$CMOD_p$	Permanent Crack Mouth Opening Displacement due to Pre-cracking
d	Position of the Reinforcing Bar Steel From the Top of the Beam
δ	Vertical Displacement
$\delta_{e,s}$ / $\delta_{e,s,exp}$	Elastic Mid-span Displacement due to Sustained Load
$\delta_{e,s,mod}$	Creep Model Elastic Mid-span Displacement due to Sustained Load
δ_{max}	Maximum Mid-span Displacement due to Pre-cracking
δ_p	Permanent Mid-span Displacement due to Pre-cracking
Δt_i	Number of Days that a Temperature T Prevails
E	Elastic Modulus of Concrete
E_c	Elastic Modulus of Cracked Concrete
$E_{eff}(t,t_0)$	Effective Elastic Modulus of Concrete
$E_{c,eff}(t,t_0)$	Effective Cracked Elastic Modulus of Concrete
E_s	Elastic Modulus of Reinforcing Bar Steel
$\varepsilon_{cds}(t,t_s)$	Drying Shrinkage Strain
f_{cm} / f_c	Mean Compressive Cylinder Strength of Concrete
$f_{cm,cube}$ / $f_{c,cube}$	Mean Compressive Cube Strength of Concrete

f_{r1}	Residual Flexural Tensile Strength at a CMOD of 0.5mm
f_{r2}	Residual Flexural Tensile Strength at a CMOD of 1.5mm
f_{r3}	Residual Flexural Tensile Strength at a CMOD of 2.5mm
f_{r4}	Residual Flexural Tensile Strength at a CMOD of 3.5mm
f_u	Ultimate Stress of Reinforcing Bar Steel
f_y	Yield Stress of Reinforcing Bar Steel
F	Applied Force
$F_{app,\delta=3mm}$	Applied Force at a Vertical Mid-span Displacement of 3mm
F_c	Internal Force of the Concrete
F_j	Applied Load Corresponding to the CMOD
F_L	Load Corresponding to the LOP
F_s	Internal Force of the Reinforcing Bar Steel
F_{st}	Internal Force of the Steel Fibre Reinforcing
h	Height of the Beam Section
h_c	Nominal Size of Concrete
h_{sp}	Distance between the Tip of the Notch and the Top of the Specimen
I	Moment of Inertia
k_a	Beam's Assumed Stiffness
k_e	Beam's Stiffness Before Cracking
k_u	Beam's Unloading Stiffness
L	Span Length
λ	Effective Height Factor of Concrete's Compression Zone
M	Bending Moment
$M_{app,\delta=3mm}$	Applied Moment at a Vertical Mid-span Displacement of 3mm
M_d	Ultimate Design Bending Moment
M_r	Ultimate Resisted Bending Moment

M_{sus}	Applied Sustained Bending Moment
ω	Damage Factor
P	Sustained Point Load
$\varphi_{bc}(t,t_0)$	Basic Creep Coefficient
$\varphi_c(t,t_0)$	Creep Coefficient
$\varphi_{dc}(t,t_0)$	Drying Creep Coefficient
$\varphi_{fpc}(t,t_0)$	Fibre Pull-out Creep Coefficient
σ_{max}	Maximum Tensile Stress
σ_{max}	Sustained Tensile Stress
t	Concrete Age at the Moment Considered
t_s	Concrete Age at the Beginning of Drying
t_T / $t_{0,T}$	Temperature Adjusted Concrete Ages
t_0	Concrete Age at Time of Loading
T	Temperature
$T(\Delta t_i)$	Temperature during the Time Period Δt_i
θ	Rotation
u	Exposed Perimeter of Concrete
V	Shear Force
V_t	Volumetric Fibre Content
w	Distributed Load
W_{sus}	Applied Sustained Weight to induce M_{sus}
x	Position of the Neutral Axis of the Beam Section
y	Horizontal Position of Centroidal Axis

Chapter 1
Introduction

1.1 Overview

Steel Fibre Reinforced Concrete (SFRC) is a concrete consisting of cement, aggregates, water, admixtures and small randomly distributed steel fibres. Steel fibre volumes in SFRC are typically less than 2%. Fibres were initially added to reinforced concrete as secondary reinforcement to allow for crack control. This is however changing in recent years as SFRC is being introduced to more structural applications.

Steel fibres have no effect on the tensile strength of concrete but do significantly influence its post-cracking behaviour (Bentur & Mindess, 2007). The fibres allow the bridging of cracks, leading to significant residual tensile strength of the concrete. The bridging mechanisms also provide the concrete with increased energy absorption capacity.

Cracked SFRC does however have an additional time-dependent characteristic to that of reinforced concrete. This behaviour has been identified as a result of fibre pull-out creep. The factors often cited to effect the rate of this additional creep are, fibre dosage, concrete type, curing conditions, relative humidity and loading characteristics (Van Bergen et al., 2016). Particular importance has been placed on the influence of magnitude and duration of the load on SFRC's fibre pull-out rate. Unfavourable loading conditions have been shown to be significant enough to result in the sudden failure of SFRC (Kusterle, 2016).

1.2 Problem Statement

Substantial research on the effect of fibre pull-out on axial and flexural creep of cracked SFRC has been published of late. The initial studies examined the material at a single fibre and macroscopic level. As a result of the increased use of SFRC in construction, time-dependent research at the structural level has become prevalent. None of this research

has however, at any level, addressed the problem of developing a design model predicting the long-term deflections of SFRC.

The primary goal of this study is the development of a preliminary design model for cracked SFRC that includes the additional fibre pull-out behaviour. In order to achieve this milestone, three objectives were defined. These objectives and a brief methodology are provided in the following section.

1.3 Objectives and Methodology

The key objectives of this study include:

- To evaluate and compare the structural creep deflections of SFRC, reinforced concrete and a combination of the two reinforcements.
- To understand the time-dependent behaviour of SFRC at a macroscopic level.
- To develop a preliminary design model that can predict the long-term deflections of cracked SFRC.

The methodology followed to reach each of these objectives are:

- The determination of the flexural long-term deflections of large scale pre-cracked SFRC beams.
- To record the time-dependent crack mouth opening displacement rates at different steel fibre dosages using uniaxial tensile creep tests.
- The verification of the reinforced concrete flexural creep results with the current Fédération Internationale du Béton *(fib)* Model Code's Age Adjusted Effective Modulus method.
- The modelling of the SFRC macroscopic level results to calibrate an adapted *fib* design model including fibre pull-out behaviour of SFRC at a structural level.

1.4 Thesis Layout

A background into the mechanical properties of SFRC is provided in Chapter 2. The time-dependent behaviour of both cement-based materials and cracked SFRC is also discussed.

Chapter 3 describes the experimental methodology used in this study. This section was divided into three sections, namely: the concrete mix properties, the mechanical properties, and the time-dependent properties.

The flexural design method used to design the reinforced beams is provided in Chapter 4.

Chapter 5 presents the results of the mechanical properties of the materials used. This includes: the compressive strength, density, modulus of elasticity of the concrete mixes; the tensile resistance of the reinforcing bar steel and SFRC; and the flexural resistances of the three beam types.

The time-dependent results of both cracked reinforced concrete and SFRC are presented and discussed in Chapter 6.

In Chapter 7 a design model is proposed for cracked SFRC. Three models are used to generate this design model. These include, a damage model, a creep load model, and an adjusted *fib* model to include the additional fibre pull-out behaviour of SFRC.

Chapter 8 provides the significant findings of this study. Recommendations for possible future research identified in this research are also presented.

Chapter 2
Mechanical and Time-dependent Behaviour of SFRC

2.1 Mechanical Behaviour of SFRC

The fibres in SFRC are activated once matrix cracking of the concrete composite has occurred. The overall mechanical performance of the material is highly dependent on the fibre distribution, fibre orientations, and the fibre arrangement within the bulk cement-based matrix. The interface between a fibre and the cement matrix is often the weakest zone and understanding the characteristics of this region is vital in understanding SFRC's structural behaviour. In this section the microscopic and macroscopic levels of SFRC and their influence on the material's overall behaviour are discussed.

2.1.1 Microscopic Level

Understanding the microstructure of SFRC is critical as it often governs the overall performance of the material (Löfgren, 2005). The microstructure of concrete is formed during the hydration process, where cement and water react to give concrete its strength and stiffness. The addition of steel fibres has no significant effect on the development of the bulk matrix of concrete (Bentur & Mindess, 2007). The pull-out behaviour of a fibre is however significantly influenced by the microstructure at the interface between the fibre and matrix. In this section the interface between the fibre and bulk matrix, bridging mechanisms, and the fibre pull-out behaviour of SFRC are discussed.

2.1.1.1 Fibre/Matrix Interface

The Interfacial Transitional Zone (ITZ) is the interface at which the fibre and bulk cement matrix is bonded to one another. These bonds form during the hydration process of cement. The properties of this bond are dependent on many factors, including the water/cement ratio, bleeding of fresh concrete and geometry of the fibre (Löfgren, 2005). The formation of the ITZ occurs due to a number of interconnected micromechanics (Bentur, 1991). One of these is what is known as the wall effect. This refers to inefficient packing of particles surrounding the fibre. Bleed water is also able to congregate in this region due to the fibre's significant size in comparison to the bulk matrix. The resulting water filled voids can only be partially filled with hydration products. This creates a zone with an increased amount of Calcium Hydroxide (CH) crystals and a high porosity, Figure 1. There are several other explanations for the formation of this zone. In spite of this, the main deduction is that the ITZ has a considerably lower strength and stiffness than that of the bulk cement matrix. The pull-out behaviour of a fibre is therefore significantly dependent on the ITZ (Löfgren, 2005).

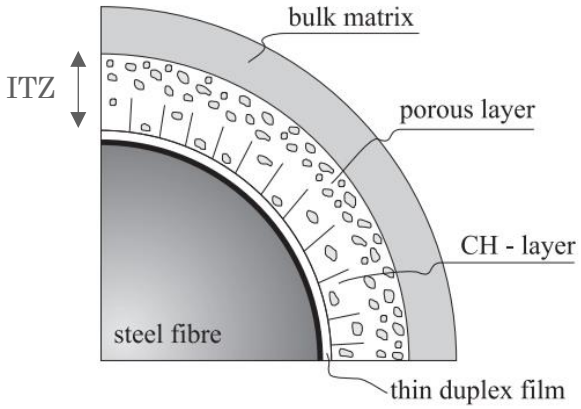

Figure 1: A schematic depiction of the Interfacial Transition Zone (ITZ) of a fibre (Cunha, 2010).

2.1.1.2 Crack Bridging Mechanisms

When a crack propagates in ordinary concrete, aggregates provide bridging traction in the crack. This mechanism is schematically represented in Figure 2. Micro-cracks grow at the ITZ between the aggregates and cement matrix. At peak stress (Point C) localisation of the crack forms, from which it then propagates further. It is in this propagation zone that

the bridging mechanism occurs. The traction gradually decreases to zero at a crack opening of 0.3mm (Löfgren, 2005), at which stage a macro crack has formed.

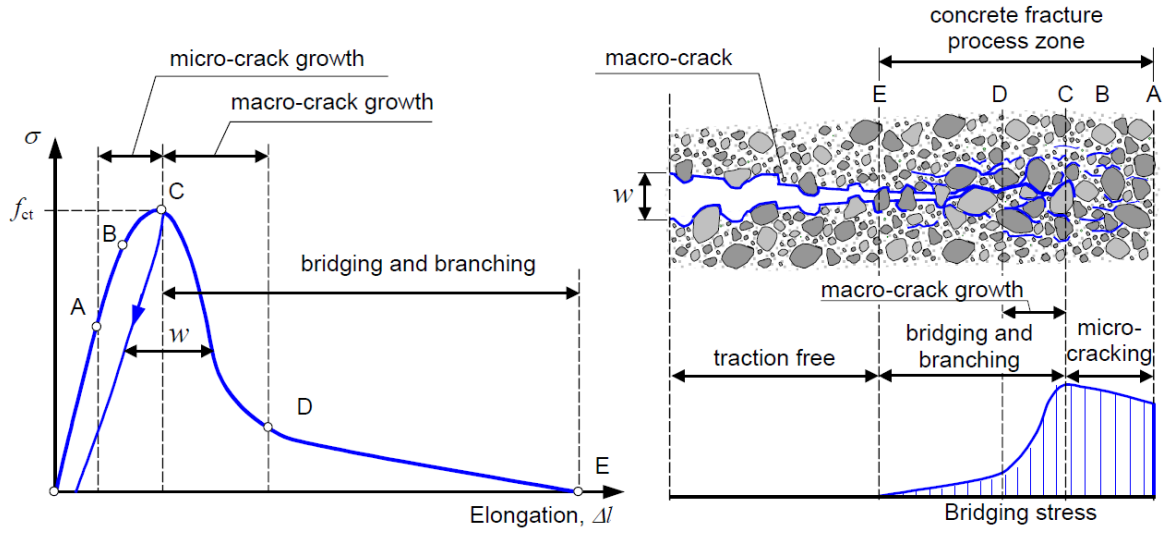

Figure 2: Crack bridging mechanisms and the stress-crack opening relationship of ordinary concrete (Löfgren, 2005).

Crack growth can be reduced by the addition of steel fibres. In SFRC there are two possible bridging mechanisms, namely the combined bridging of aggregates and fibres, and fibre only bridging mechanisms. Both these mechanisms help reduce the opening rate of the crack due to the stress transfer to the fibres. The crack width continues to increase with time but the SFRC composite is able to absorb a lot more energy, as seen in Figure 3. The amount of energy absorbed is highly dependent on the amount and orientations of the fibres, as well as the pull-out behaviour of the individual fibres (Löfgren, 2005).

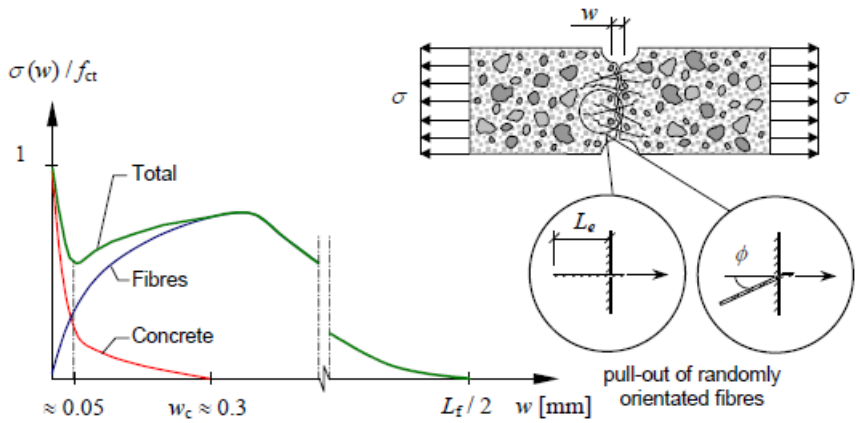

Figure 3: Combined fibre and aggregate bridging for SFRC in uniaxial tension (Löfgren, 2005).

2.1.1.3 Fibre Pull-out Behaviour

The transmission of forces between a fibre and the cement matrix is provided through the bond. This transmission can be improved by mechanical anchorage of the fibre (Bentur & Mindess, 2007), with hooked-end steel fibres being the most common example of this modification. The fibre pull-out behaviour of a hooked-end fibre can be divided into a number of phases (Ghoddousi et al., 2010). These phases are shown in Figure 4. The first phase is the partial (AB) to full debonding (BC) of the fibre. This is followed by the frictional slip (CD, DE) and eventual pull-out of the fibre (EF). A hooked-end fibre is required to fully straighten in order to allow pull-out. The increase in energy absorption of a fibre with mechanical anchorage can be seen in the pull-out response graph in Figure 4. A study by Robins et al. (2002) indicated that the pull out response of a hooked-end fibre is primarily influenced by three factors, namely, fibre orientation, fibre embedment length, and matrix strength.

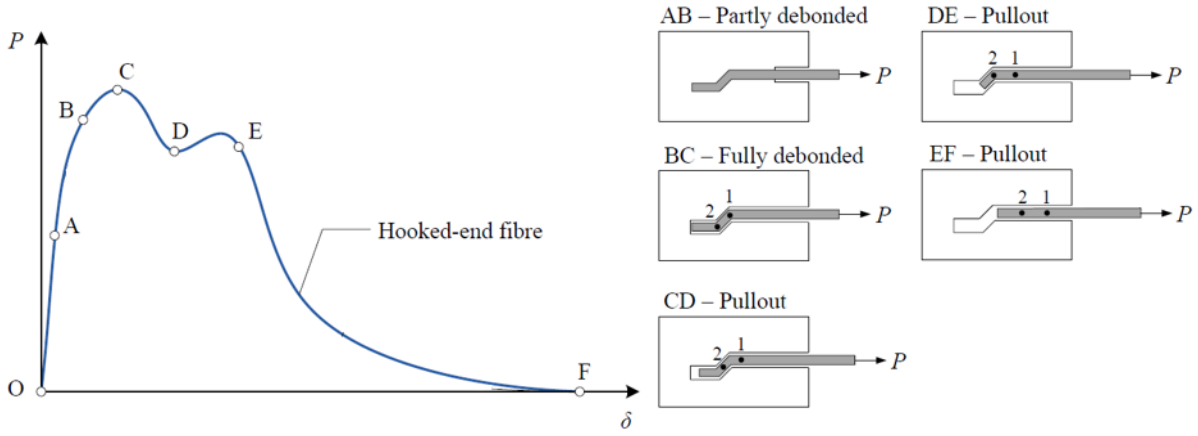

Figure 4: Typical pull-out response in hooked-end fibres (Ghoddousi, 2010).

2.1.2 Macroscopic Level

The macroscopic level of SFRC's structural properties is presented in this section. The influence of steel fibres on the compressive, tensile and flexural strength of concrete is discussed.

2.1.2.1 Compression Properties

The main influence of fibres on a composite's compressive strength, is an increased toughness of the material (Ou et al., 2012). This is as a result of the fibres bridging the longitudinal crack growth caused by lateral expansion of the concrete under compression (Löfgren, 2005), as seen in Figure 5.

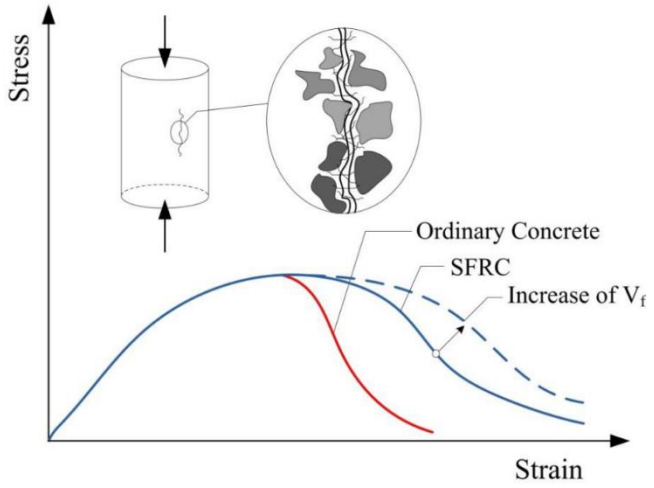

Figure 5: Schematic depiction of the compressive behaviour of ordinary concrete and SFRC (Löfgren, 2005).

The improved ductility of SFRC compared to ordinary concrete is also demonstrated in Figure 5. The performance of SFRC in compression can be further improved by increasing the volumetric fibre content *(V_f).* It is also highly dependent of the type of fibre used. Research by Ou et al. (2012) has suggested that the improvement of hooked-end fibres reached a limit at a fibre dosage of 2%.

2.1.2.2 Tensile Properties

The tensile response of SFRC is considerably more ductile in comparison to ordinary concrete's brittle failure, as shown in Figure 6. The initial tensile elastic response is similar for both SFRC and ordinary concrete. The fibres however provide the SFRC with a post-crack tensile residual strength, characterised by non-linear behaviour. The post-crack tensile behaviour of SFRC can either be classified as strain softening or strain hardening. The type of behaviour that SFRC exhibits is dependent on its critical fibre

volume (Fantilli et al., 2009). A SFRC containing a fibre dosage larger than the critical fibre dosage will experience strain hardening, whereas strain softening will occur if the dosage is less than the critical fibre dosage. Strain hardening is characterised by an increase in the post-cracking strength beyond the first crack strength. These materials typically allow the formation of multiple cracks and this response is generally seen in high performance fibre reinforced cement composites (Gustavo J., 2005).

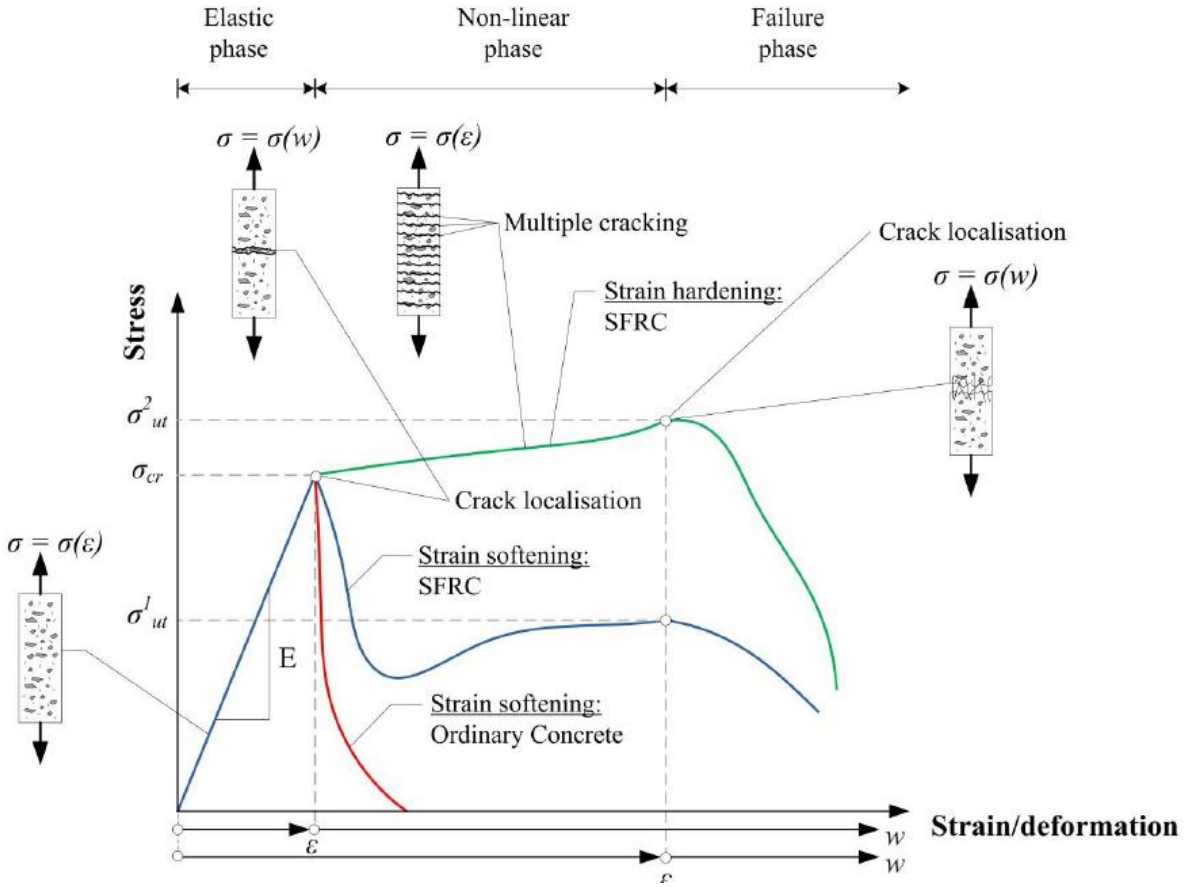

Figure 6: The tensile response of SFRC compared to that of ordinary concrete (Löfgren, 2005).

If the dosage is less than the critical dosage, the tensile response of SFRC is characterised by strain softening behaviour, in which the post-cracking strength is lower than the first crack strength. This behaviour is often characterised by the formation of a single localised crack. Failure of strain softening fibre composites occurs once the maximum post-crack strength has been obtained. The failure can be a consequence of two phenomena: the rupture of fibres or pull-out of fibres from the bulk matrix. The rupturing of fibres occurs when the fibre-matrix bond strength exceeds the tensile strength of the steel fibre (Bentur, 2007). This phenomena is usually observed in synthetic fibre reinforced concrete

as well as strain hardening composites. The result of this stress concentration usually results in a brittle failure of the material. Fibre pull out failure occurs when the fibre-matrix bond strength is exceeded and is characterised by a more ductile failure.

2.1.2.3 Flexural Properties

The behaviour of SFRC under increasing flexural load is characterised by three distinct phases, as represented in Figure 7. The linear elastic phases is similar to that of ordinary concrete. As soon as the first crack appears, the material's tensile capacity changes to the resistance provided by the fibres bridging the crack. This causes the neutral axis to shift to ensure that equilibrium is maintained. The increasing flexural load causes the crack to propagate further toward the neutral axis, thus continually changing the position of the neutral axis. The ultimate failure of the section occurs due to fibre rupture or fibre pull-out, as discussed in Section 2.1.2.2.

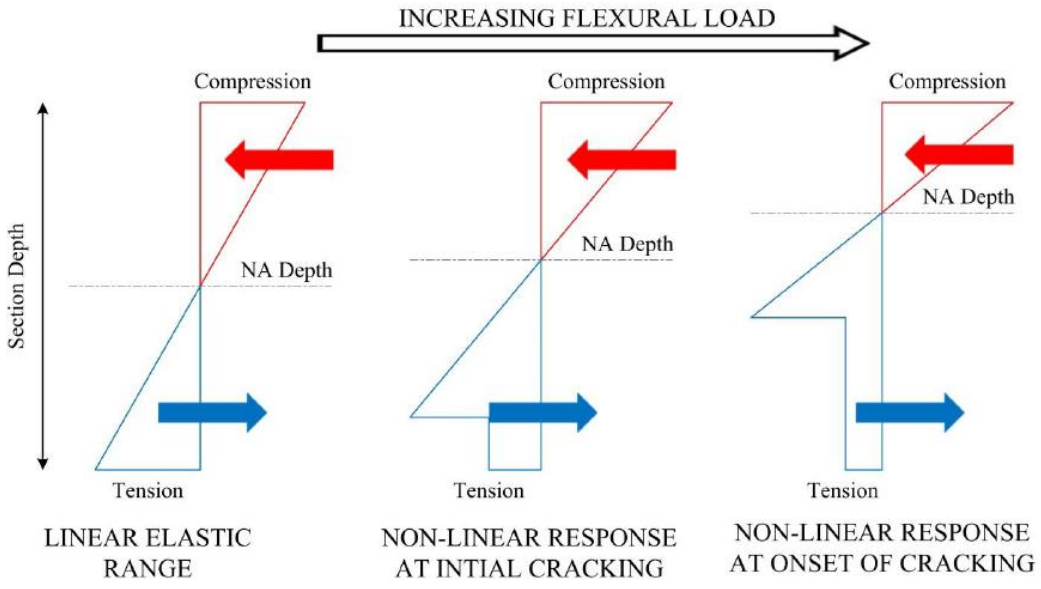

Figure 7: Schematic flexural stress distribution of SFRC (Jarratt, 2011).

An increasing flexural load can result in either deflection softening or deflection hardening. This behaviour is characterised in Figure 8. A material undergoing deflection softening requires no increase in the flexural load to cause failure. A deflection hardening material however can withstand an increase in flexural load due to the additional stiffness contributed by the fibre bridging mechanisms. A material with uniaxial strain hardening properties will cause a deflection hardening flexural response. A material showing uniaxial strain softening behaviour however can behave as a deflection softening or

deflection hardening material when a flexural load is applied. The flexural response largely depends on the fracture properties as well as the dimensions of the section (Löfgren, 2005).

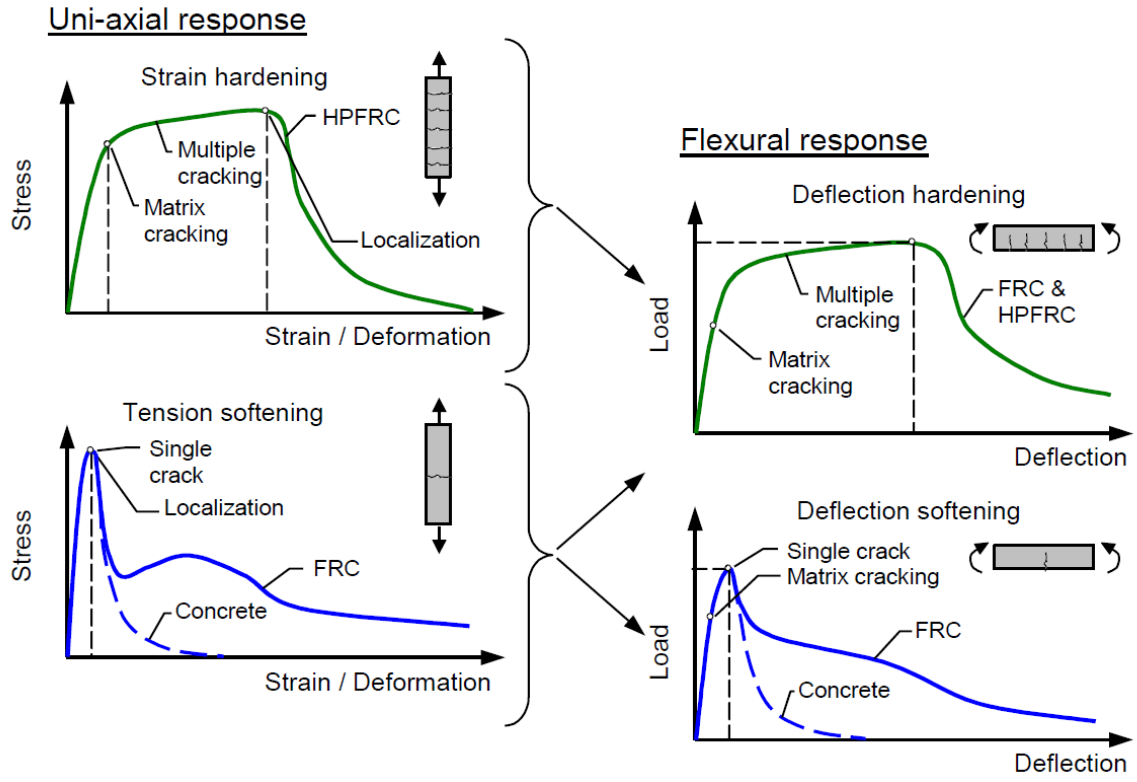

Figure 8: SFRC characterisation of tensile and flexural behaviour (Löfgren, 2005).

2.2 Time-dependent Behaviour of Cement-based Materials

The time-dependent behaviour of concrete is a result of two phenomena, namely: shrinkage and creep. These phenomena result in the gradual increase in deformation of concrete with time. The reason for this time-dependent behaviour can be attributed to several mechanisms present in cement-based materials. These shrinkage and creep mechanisms are presented in this section.

2.2.1 Shrinkage Mechanisms

Shrinkage results in a volumetric change in concrete which is attributed to several micro-mechanisms. When however observed from a macro-level, shrinkage can be divided into,

autogenous shrinkage, chemical shrinkage, carbonation shrinkage, and drying shrinkage (Nieuwoudt, 2016).

Autogenous shrinkage is a consequence of the hydration process. Unhydrated cement particles attract water present in capillary pores of the cement paste. It is this extraction process that causes a volume change in the concrete.

Chemical shrinkage occurs typically in the plastic phase and is a result of the chemical reaction between cement and water. The volume reduction is mainly due to the solidification of free water in the concrete.

Carbonation shrinkage is the result of hydrated cement particles reacting with moisture and carbon dioxide from the environment. This reaction takes place on the concrete's surface and causes the pH of the concrete to lower.

Drying shrinkage is commonly defined as the reduction in volume due to the loss of water from the concrete. Drying is initiated when the ambient relative humidity is lower that the internal relative humidity of the material. Initially, water migrates to the surface as bleed water and subsequently evaporates. This drying process then results in excess water being drawn from concrete's interior. This water is extracted from capillary voids causing shrinkage of the unrestrained hydrated cement paste.

2.2.2 Creep Mechanisms

Creep can be defined as the increase in a material's deformation under a constant load or stress over a period of time. The creep of cement-based materials is theorised to be a combination of three mechanisms (Neville, 1970).

The first is due to the migration of water in the capillary pores of the cement matrix. The stress imposed by loading causes the redistribution of this water. The water distribution occurs between hydrated products and unhydrated cement. The movement of water between hydrated particles is reversible, whereas it results in the hydration of unhydrated cement causing irreversible migration.

The second mechanism is attributed to the breaking and re-establishing of CH micro-bonds. The applied stress causes some of these bonds to break due to internal stress peaks. The redistributed moisture, described in the first mechanism, then allows the CH bonds to reform in their new positions. This causes irreversible permanent deformation.

The last mechanism is the formation of micro-cracks in the cement matrix due to the sustained loading. These cracks that can continue to grow over time and ultimately result in the failure of the material. This failure however only occurs at sustained load levels of greater than 70% (Neville, 1970).

2.2.3 Creep Behaviour

The creep behaviour of concrete due to a sustained load is presented in Figure 9. The sustained loading initially causes an instantaneous elastic deformation in the concrete. This is then followed by the initiation of creep. The rate of this creep tends to gradually decrease with time if no additional loading is applied. When the sustained loading is removed an instantaneous elastic recovery is experienced. A small amount of creep recovery is achieved over time. The remainder of the creep deformation is thus irreversible creep, resulting in permeant deformation.

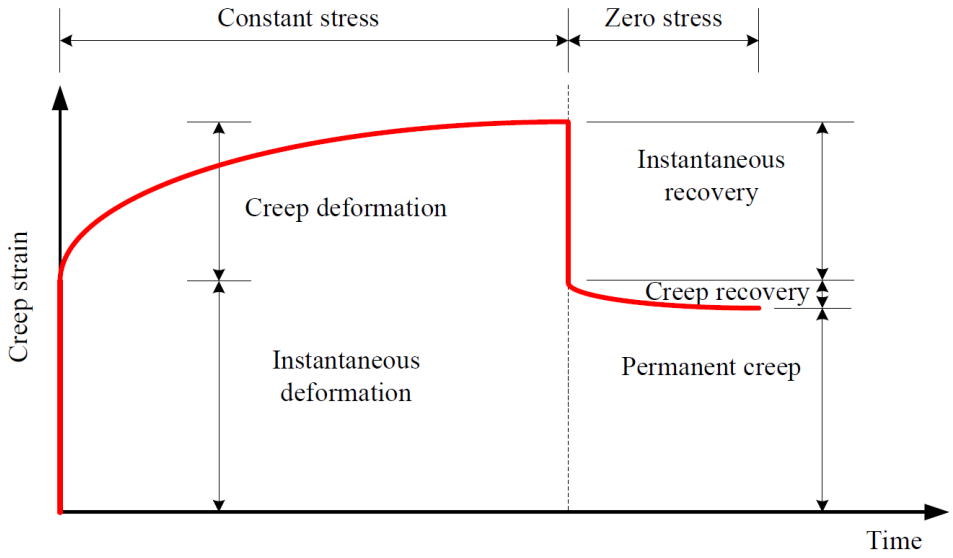

Figure 9: Schematic representation of concrete's creep response over time (Atrushi, 2003).

Creep deformations can be divided into three stages, namely, primary creep, secondary creep and tertiary creep (Nieuwoudt et al., 2017). Primary creep is defined as the initial increase in creep deformation. This is then followed by secondary creep, usually characterised by steady long-term deformation. Secondary creep usually tends to an asymptotic value over time. The third stage, tertiary creep, only occurs if creep failure is initiated.

2.3 Time-dependent Behaviour of Cracked SFRC

The understanding of the time-dependent behaviour of SFRC has increased rapidly over recent years. Extensive research has been published on the time-dependent responses of SFRC. There are however still no available design codes that take this behaviour into account. This study aims to propose an initial model that can be used in predicting the long-term deflections of SFRC. For this reason a study of the time-dependent behaviour of SFRC is presented and discussed.

2.3.1 Uniaxial Tensile Creep Response

The use of fibres in concrete can help eliminate the serviceability problems associated with crack propagation in conventionally reinforced concrete. SFRC has however also exhibited time-dependent properties, where crack widths increase with time (Kusterle, 2016). This additional crack width increase is due to a phenomena described as fibre pull-out (Mouton, 2012). Several methods exist in quantifying this behaviour, however it is widely acknowledged that the uniaxial tensile creep test provides the most reliable and accurate results (Mouton, 2012; Nieuwoudt et al., 2017). This study will therefore make use of the uniaxial tensile creep test in order to obtain the axial tensile time-dependent behaviour of the cracked SFRC.

Mouton (2012) performed uniaxial tensile creep tests on pre-cracked beam specimens. The specimens were pre-cracked to a Crack Mouth Opening Displacement (CMOD) of 0.5mm and a 50% residual tensile strength sustained load applied for 3 months. A large scatter in results were obtained with CMODs of between 0.07-1.23mm. These results showed the significant tensile creep experienced by cracked SFRC due to fibre pull-out.

Research by Nieuwoudt et al. (2017) showed that the concentration of fibres present on a crack plane significantly influences the creep response. The specimens with the highest fibre counts had the lesser time-dependent CMOD. The study found that the rate of tensile creep is highly dependent on the applied stress level. Micro-cracking, at the hooked-end of the fibre, was also observed at high stress levels. This indicates that the main mechanism for fibre pull-out behaviour in cracked SFRC is an increase in micro-cracking.

2.3.2 Flexural Creep Response

The investigation into the flexural creep behaviour of SFRC can be divided into the creep properties of the conventional concrete, discussed in Section 2.2.3, and the interface between fibres in the cement matrix. The creep experienced at this interface, i.e. fibre pull-out creep, is dependent on the factors discussed at SFRC's microscopic level. This additional fibre pull-out creep can be significant enough to result in the sudden failure of pre-cracked SFRC specimens (Van Bergen, 2016).

Flexural creep tests were performed by Kusterle (2016) on 150×150×500mm hooked-end steel fibre beams for a period of 7 years. The beams were loaded at several load levels of the residual load at a deflection of 1.75mm. The SFRC showed satisfactory results at low load levels, however at load levels of 75% and higher, fibres started slipping out of the matrix and creep rupture occurred.

Research by Garcia-Taengua et al. (2016) involved testing cracked SFRC specimens under sustained loading for a minimum of 90 days. During this testing three factors were observed to greatly influence the flexural creep response. These factors included, the compressive strength of the concrete, the applied stress level and the sum of the residual flexural strength values obtained using BS EN 14651 (2005). A study by Van Bergen et al. (2016) also demonstrated that higher fibre dosages can result in increased deflections.

Large scale cracked flexural beam tests were performed by Nakov et al. (2016). SFRC with dosages of 0kg/m^3, 30kg/m^3 and 60kg/m^3, and reinforcing bar steel were combined in beams with dimensions 150×280×3000mm. The beams were pre-cracked and then subject to continuous variable loading. The results indicated that the steel fibre reinforcing had a positive influence in reducing the flexural creep response. A reduction in fibre pull-out over time was also reported.

2.4 Concluding Summary

The mechanical behaviour of SFRC is studied in this chapter. The material is presented at both a microscopic and macroscopic level. A background of the time-dependent behaviour of cement-based materials and cracked SFRC is also reported. Specific focus is given to the additional time-dependent behaviour of cracked SFRC, namely fibre pull-out creep.

Research available on the fibre pull-out behaviour of cracked SFRC has increased substantially over the last few years. The understanding of the factors causing and influencing the additional crack opening over time are improving with time. There is still however no design model that can be used to predict the time-dependent behaviour of cracked SFRC.

With the increasing use of SFRC in construction it is therefore vital that a prediction technique is established in order to assure the long-term behaviour of the material.

Chapter 3
Experimental Framework

This chapter presents a description of the concrete mixes used, and the tests performed to obtain the mechanical and time-dependent properties of the applicable materials. A detailed description each test is provided along with its experimental programme.

3.1 Concrete Mixture

3.1.1 Concrete Mix Materials

One type of hooked-end fibre was used in this research project, namely DRAMIX RC-80/60-BN fibres. These macro steel fibres are mainly recommended for flooring and precast applications. Portland cement 52.5N CEM II/A-L (limestone extender content of between 6-20%), fine aggregate (natural pit sand, commonly known as Malmesbury sand) and coarse aggregate (9mm Greywacke stone) were also used. A CHYRSO Fluid Optima 206 superplasticiser was added at a dosage of 1% of the binder weight to improve the workability of the mix.

3.1.2 Mix Design

For this research three mixes were required: a normal concrete mix (NC) with no fibres; a concrete mix with a fibre dosage of 30kg/m^3 (SF30); and one with a dosage of 60kg/m^3 (SF60). All three mixes however had the same basic mix design, see Table 1.

Table 1: Basic mix design used for all concrete mixes.

Mix Design	kg/m^3
Cement (52.5N CEM II)	370
Water	203.5
Sand (Natural pit sand)	890
Stone (9mm Greywacke)	890
Superplasticiser (1% by weight of binder)	3.7
Steel Fibres (RC-80/60-BN)	0 / 30 / 60

3.1.3 Mixing Procedure

All mixes were performed in a 120l concrete pan mixer, unless otherwise specified. The constituents of each mix were measured off before mixing commenced. The following mixing procedure was used for each mix:

→ The pan mixer was wiped with wet tissue paper to decrease the water absorption of the pan.

→ The dry constituents were then added in the following order: stone, cement and sand. The constituents were then mixed for 30 seconds.

→ Water was then added to the mix and allowed to mix for 2 minutes.

→ The superplasticiser was added gradually and mixing continued for another 2 minutes.

→ Steel fibres were then added (if applicable) over a period of one minute. This was to ensure that no fibre-balling occurred.

→ After the last portion of fibres were added, the concrete was allowed to mix for another 2 minutes. If no fibres were added, the concrete was mixed for a total of 5 minutes after the superplasticiser was added to ensure consistency.

→ The mixer was then turned off, the concrete mix tipped into a wheelbarrow, and transported to the moulds.

3.1.4 Flowability

Fibres have a significant effect on the workability of concrete. The two fibre characteristics with the greatest influence on the workability of SFRC are the fibre aspect ratio, as well as the volume of fibres (Swamy & Mangat, 1974). An increase in either of these characteristics result in an increased fibre surface area. The consequence of this is that more cement paste is required to coat each fibre's surface area and therefore increases the concrete's resistance to flow. The effect of fibre volume was investigated in this research. The procedure described in BS EN 12350-2 (2009) was used in performing slump tests.

The normal concrete mix, without the addition of any fibres, obtained a slump of 130mm. The addition of 30kg/m^3 of 3D-60mm steel fibres resulted in a slump of 100mm. Thus resulting in a 23% slump reduction. A fibre addition of 60kg/m^3 to the basic concrete mix resulted in a slump of 60mm. This was a reduction of 54% in the concrete's slump value. The volume fraction of fibres in a SFRC mix therefore has a substantial influence on the workability of the mix.

3.2 Mechanical Properties

3.2.1 Compressive Strength

Compressive strength tests were performed on each mix to obtain the early age and design compressive strengths. A total of eight cubes, with dimensions 100×100×100mm, were cast for the 7 and 28 day strengths of each mix. The SF60 and SF30 cubes were cast from the same batches used in the notched beam tests, presented in Section 3.2.5. A 25l mixer was used to cast the NC cube specimens however the same procedure outlined in Section 3.1.3 was used. The specimens were tested in a Contest Compression Testing Machine, at a constant loading rate of 180kN/min (BS EN 12390-3, 2002). The load was applied perpendicular to the casting direction of the cubes. Control cubes were also cast for other selected tests and tested using the same method.

3.2.2 Density

The density of each mix was required in order to calculate the material's self-weight. The cubes cast for the compressive strength tests were used to obtain these values. The mass and dimensions of each cube was measured before crushing and the average density of each mix was reported. The density of each mix was of particular importance in both the reinforced beam tests and cracked reinforced beam creep tests. The flexural load produced by the self-weight of the beam had to be added to the applied flexural load in order to calculate the ultimate flexural capacity.

3.2.3 Modulus of Elasticity

The modulus of elasticity was an important property to obtain for the modelling purposes of this research. Three cylinder specimens, each with a diameter of 100mm and height of 200mm, were cast and tested at 28 days for each mix. The cylinders were cast from the same concrete batches produced for the cracked reinforced beam creep tests. The procedure detailed in BS EN 12390-13 (2013) was used to obtain the elastic modulus. In this test each specimen was loaded to 30% of the material's ultimate cylindrical compressive strength. Three consecutive loading repetitions were performed on each specimen. The gradient of the stress-strain relationship of the last repetition was used as the elastic modulus value of each cylinder. The ultimate cylinder compressive strength of each mix was obtained by multiplying the average 28 day compressive cube strength of each mix by a factor of 0.8 (BS EN 1992-1-1, 2004).

Before testing on the specimens began, the casting face of each cylinder was ground to obtain a smooth testing surface. This was done on a Matest Grinding Machine. The load was applied to each cylinder using a Contest Compression Testing Machine, at a constant loading rate of 180kN/min. The loading and deformation of each cylinder was recorded with a Spider8 data acquisition system. A compressive load cell was used to measure the loading. This was then divided by the cylinder's cross-sectional area in order to calculate the compressive stress. The vertical displacement was recorded using three Linear Variable Displacement Transducers (LVDT) at intervals of 120 degrees. The gauge length of each LVDT was 70mm. The average reading of all three LVDT's, obtained from the data acquisition system, was taken as the overall deformation.

3.2.4 Reinforcing Bar Tensile Strength

The reinforcing bar steel properties were obtained using the guidelines set out in the SANS 6892-1 (2010). Four specimens, each with a length of 300mm, were cut from four different reinforcement bars. Each specimen was clamped into a Zwick Universal Testing Machine. An extensometer, with a gauge length of 80mm, was attached to the specimen in order to measure the deformation. A pre-load of 1000N was applied to each bar before testing to ensure that it was properly secured. A constant loading rate of 600N/s was then applied. The test was terminated when the extensometer reached its maximum displacement of 2.5mm.

The elastic modulus of the reinforcing bar steel was calculated using the gradient of the linear section of the stress-strain curve. The steel's yield stress *(f_y)* was calculated using the offset method as specified in ASTM E8/E8M–09 (2010). A line with the gradient equivalent to the steel's elastic modulus and the x-intercept equal to a strain of 0.002 was plotted. The intercept of the plotted line and the steel's stress-strain curve was reported as the yield stress.

3.2.5 Notched Beam Test

3.2.5.1 Overview

A notched beam test, also referred to as a three-point bending test, was initially standardised by RILEM TC 162-TDF (2002). The test was revised by the European Standard Committee and it was this test method (BS EN 14651, 2005) that was used in this research. Notched beam tests were performed on both the SF30 and SF60 mixes. The tensile behaviour of SFRC was determined by applying a central point load on a simply supported notched SFRC beam. The flexure-CMOD curve acquired allowed the residual tensile strength properties to be calculated.

3.2.5.2 Test Specimens

Steel moulds were used to cast 150×150×550mm concrete beams. A 120l concrete pan mixer was used to cast six beams at a time. A slump test was performed on each mix to

ensure mix control. The casting moulds were oiled with mould release oil before mixing. A poker vibrator was used to compact the mix. The casting face of each mould was then levelled off with a hand-trowel. Eight control cubes were cast for the 7 and 28 day compressive strength of each mix. The beams and cubes were demoulded after ± 24h and placed in curing tanks.

The beam specimens were removed from the curing tanks 3 days before testing to be notched. The beam was placed with its casting face facing up and then rotated 90º along its longitudinal axis. This was to ensure that there were two smooth surfaces for the beam to be supported on, as well as the load to be applied on. A notch was then sawn at mid-span through the width of the specimen. Wet sawing with a diamond-tipped concrete blade was used to produce a notch with a width of 3.5mm and a depth of 25 ± 1mm. After notching the specimens were returned to the curing tanks.

All specimens were tested 28 days after mixing. The beams were removed from the curing tanks ± 3h before testing and allowed to dry. Once dry, two knife edges were positioned and glued, 10mm apart, at the midpoint of the notch. The knife edges were used to attach the displacement transducer, used to measure the CMOD.

3.2.5.3 Experimental Methodology

The notched beam tests were performed on an Instron 2000KPX Universal Testing Machine with a capacity of 2MN. Each beam was supported on two steel roller supports, with the distance between the centres of the rollers being equal to 500mm. A third roller located at the mid-span of the beam was used to apply the load, as seen in Figure 10. A crack opening displacement extensometer, with a gauge length of 10mm and travel of 4mm, was clipped between the two knife edges.

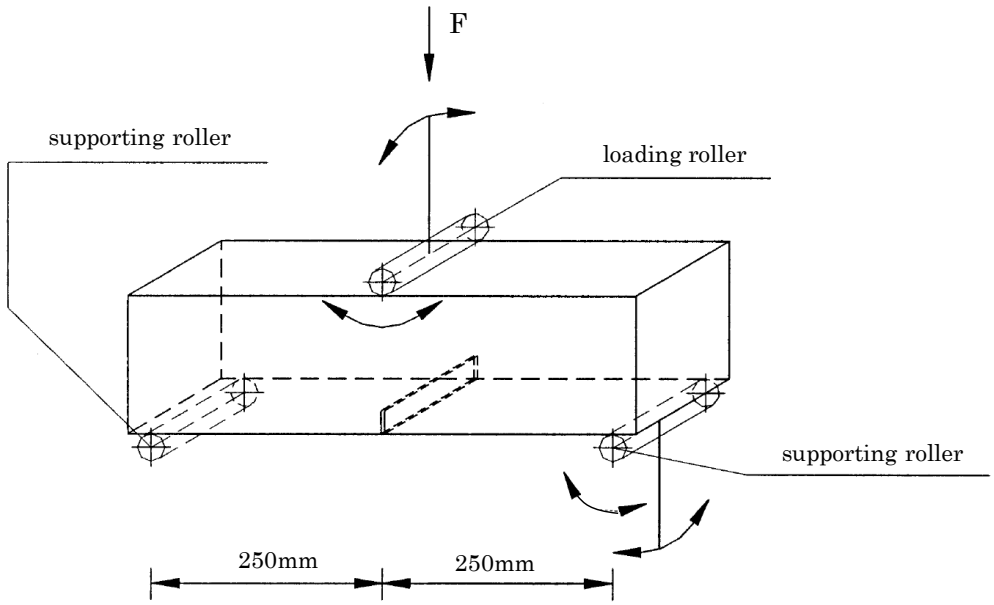

Figure 10: Loading arrangement of notched beam specimen (BS EN 14651, 2005).

The load was applied to ensure that the CMOD increased at a constant rate. Initially a CMOD rate of 0.05mm/min was used until a CMOD of 0.1mm was reached, from where a rate of 0.2mm/min was used. The test was terminated at a CMOD of 4mm.

3.2.5.4 Experimental Programme

A total of twelve specimens were prepared for each SFRC mix. The specimens were cast from two separate batches. The flexure-CMOD curve obtained from each specimen was used to record the Limit of Proportionality (LOP), as well as the residual flexural tensile strengths. The LOP is defined as the largest flexural value obtained between the CMOD interval of 0mm to 0.05mm. The following expression is used to determine the LOP:

$$LOP = \frac{3F_L l}{2bh_{sp}^2} \tag{3-1}$$

where: F_L is the load corresponding to the LOP, l is the span length, b is the width of the beam section, and h_{sp} is the distance between the tip of the notch and the top if the specimen. The residual flexural tensile strength values were determined at CMODs of

0.5mm (f_{r1}), 1.5mm (f_{r2}), 2.5mm (f_{r3}) and 3.5mm (f_{r4}). The flexural strengths are calculated with the following expression:

$$f_{r,j} = \frac{3F_j l}{2bh_{sp}^2} \tag{3-2}$$

where: F_j is the applied load corresponding to the CMOD.

3.2.6 Reinforced Beam Test

3.2.6.1 Overview

Reinforced beam tests were performed to compare the flexural resistance of SFRC and conventionally reinforced (RC) beams. The flexural capacity of a composite material with both reinforcing bars and steel fibres, referred to as combined beams, was also investigated. The test was performed by simply supporting a reinforced beam and applying a central point load. The resultant flexure-displacement curve was used to obtain the ultimate bending moment of each beam type. The cracking behaviour of each beam was also recorded by measuring the number of cracks, as well as crack widths, developed in each beam.

3.2.6.2 Test Specimens

The reinforced beams prepared in this study were intended to simulate a beam strip in a one-way reinforced suspended flat slab. The cross section of each beam was 450mm wide and 180mm deep, with an overall length of 3200mm. The SF60 concrete mix was used to cast the SFRC beams. The NC and SF30 concrete mixes were used to cast the RC and combined beams, respectively. Both the RC beams and combined beams were designed to equal the calculated ultimate flexural resistance of the SFRC beams, presented in Chapter 4. The reinforcing bars added to these beams were arranged using the layout in Figure 11. Plastic spacers were used to provide a cover of 20mm. Stirrups, transverse and top reinforcement were excluded, as these would not affect the longitudinal flexural resistance of the reinforced beam.

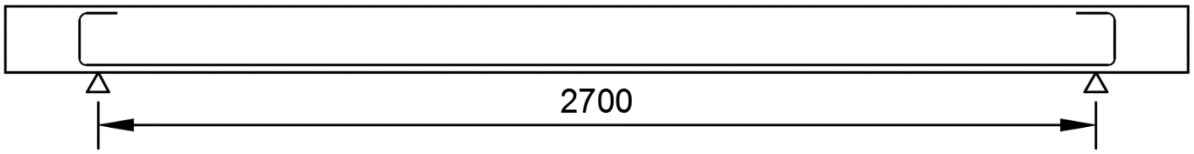

Figure 11: Reinforcement bar layout of the reinforced and combined beams.

Wooden moulds were constructed from 20mm chipboard, see Figure 12. Each mould was painted with two layers of waterproof sealer in order to minimise the absorption of water. This allowed improved curing conditions and ensured that each mould could be used multiple times. Hooks were cast into the beams to allow them to be moved with an overhead crane. The hooks were positioned 800mm away from each end, to ensure that no bending moment developed at the mid-span when each beam was demoulded or moved.

Figure 12: Reinforced beam specimen moulds.

Each mould was coated with mould release oil prior to mixing. Three batches in a 120l concrete pan mixer were required to fill a single mould. Two control cubes were cast from each concrete batch in order to assess the beam's compressive strength. A notched beam was also cast with each steel fibre reinforced beam. All the constituents required for the three batches were measured off before mixing commenced. The slump test of each mix was omitted to ensure no additional time was wasted. The pouring procedure of each specimen can be seen in Figure 13. A poker vibrator was used to compact the concrete into place. The casting face of each beam was levelled-off after adding the third batch. Plastic sheeting was then placed on top of the casting surface to minimise evaporation. After seven days of curing, the plastic sheets were removed and the specimen demoulded.

Blankets were wrapped around the concrete beam and wet once a day in order to ensure an appropriate curing environment.

Figure 13: The pouring procedure of a reinforced beam specimen

All the beams were tested after curing for 28 days. Before testing, 10mm smooth steel bars were drilled and glued into the sides of each concrete specimen to provide support for square steel tubing. The steel bars were positioned above the supports at heights provided in Figure 14. The square steel tubing, used to measure the central vertical deflection of the beam, is discussed further in Section 3.2.6.3.

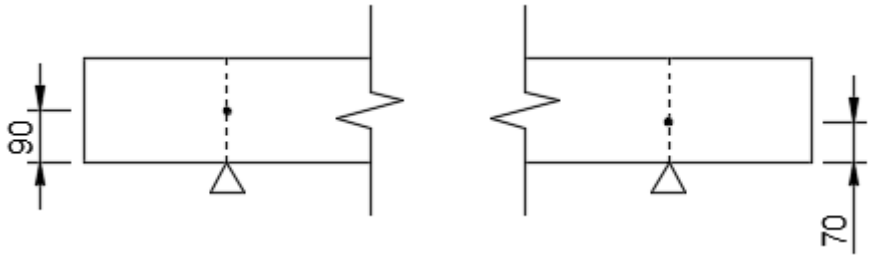

Figure 14: Position of steel bars at the reinforced beam ends.

3.2.6.3 Experimental Methodology

A central point load was applied to a simply supported beam with a span length of 2700mm. A 50kN Instron hydraulic actuator and spreader beam were used to apply the central concentrated load. The test setup is shown in Figure 15.

Figure 15: Reinforced beam test setup.

The vertical deflection was measured at the mid-span on both sides of each beam. An 11mm hole was drilled through the centre of a piece of 32×32×3000mm square steel tubing, 150mm from its end. The tubing was then fitted onto the steel bar which had been drilled and glued into the side of the reinforced beams. The other side of the steel tubing was placed on top of the steel bar, to allow the steel tube to slide over the support, as seen in Figure 16. The main purpose of the tubing was to maintain the original position of the beam's centroidal axis.

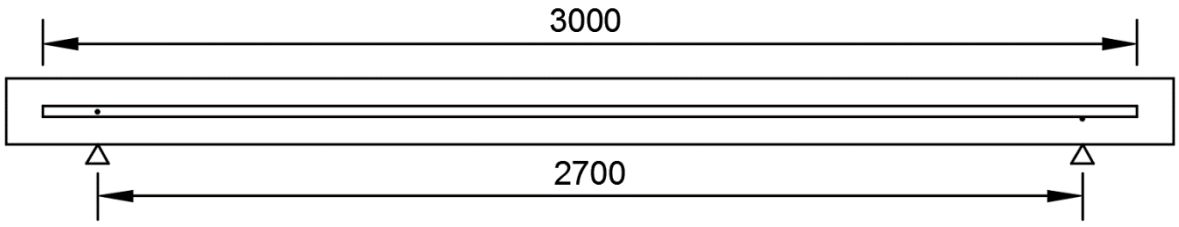

Figure 16: Position of the steel tubing on reinforced beams.

A small L-shaped steel plate was glued to the reinforced beam at its mid-span and 5mm from the top casting face. A magnetic clamp, used to hold a 50mm stroke LVDT, was attached to the steel tubing and positioned so that the LVDT rested perpendicularly below the L-shaped steel plate, see Figure 17. This process was then repeated on the other side of the reinforced beam. This setup allowed the vertical deflection to be measured with respect the beam's original centroidal axis.

Figure 17: Reinforced beam vertical deflection measurement setup.

An additional 50mm stroke LVDT was setup on the underside of the fibre reinforced beams. This was to ensure that if a beam exhibited deflection-softening behaviour, i.e. single crack formation, the strain on the tensile side of the beam was captured. The LVDT was not attached to the RC beams as a more dispersed cracking pattern was expected. An L-shaped steel plate, identical to that used in the vertical deflection measurement, and a PVC clamp were glued onto the underside of the beam. The steel plate and PVC clamp were positioned to lie in the centre of the beams tensile face, 100mm either side of the mid-span, as seen in Figure 18. This allowed the tensile strain of any crack forming within 100mm from the mid-span to be measured.

Figure 18: Tensile strain measurement setup on reinforced beams.

A displacement rate of 1mm/min of the Intron hydraulic actuator was used for all the reinforced beam specimens. A constant displacement rate was preferred over a constant force rate due to the typical decrease in load once fibre reinforced concrete has cracked. Each beam test was paused after testing intervals of 30, 60 and 120 seconds in order to examine the crack formations.

The first specimen of each beam type was used to analyse the overall behaviour of the material type. If the material exhibited a single central crack, the tensile face LVDT was added to the remaining specimens. The crack widths of the RC beams were measured just before the flexural load was removed, in order to record the maximum crack widths. The crack patterns of the second and third beam specimens of each beam type were recorded. The reinforced beam tests were terminated once a minimum crack width of 2.5mm had formed.

3.2.6.4 Experimental Programme

Three reinforced beam specimens were made for the RC, SFRC and combined beam types. Six control cubes were cast with each specimen. The crack formation, along with the flexure-displacement curve were reported for each specimen. The self-weight of each beam and force due to the spreader beam were added to the flexure-displacement curve obtained

for each test. The control cubes cast were used to obtain the average density and thus used to calculate the self-weight of each beam. The ultimate moment obtained in the experiment was used to compare and verify the design moment calculated through the specific design methods.

3.3 Time-dependent Properties

3.3.1 Cracked Reinforced Beam Creep Test

3.3.1.1 Overview

Cracked reinforced beam creep tests were performed to analyse and compare the time-dependent behaviour of normal reinforced concrete, SFRC, and a combination of the two. The beam specimens used in this test were produced in the same way as those used in the reinforced beam tests. The objective of pre-cracking the beams was to induce the fibre pull-out behaviour of SFRC. All three types of reinforced beams were pre-cracked to the same vertical mid-span deflection. After pre-cracking, the beams were placed on a simply supported setup in a climate controlled room, with a temperature of 22 ± 1°C and a relative humidity of 55 ± 5%. Each beam was loaded with a long-term load of 40% of the maximum applied flexural load during pre-cracking. The mid-span displacement due to the loading was measured.

3.3.1.2 Test Specimens

The test specimens used for the cracked reinforced beam creep tests were cast using the same procedure outlined in Section 3.2.6.2. The concrete batches used to cast the various reinforced beams were also used to cast cylinder specimens, uniaxial tensile creep specimens, as well as drying shrinkage specimens.

3.3.1.3 Experimental Methodology

The beams were pre-cracked using the setup described in Section 3.2.6.3. Prior research has suggested that at a crack width of 0.2mm, the combined bridging effect of aggregates

and fibres decreases and fibre bridging mechanisms takeover (Löfgren, 2005). It was therefore decided to pre-crack the SFRC specimens to a crack width of 0.5mm. This value ensured that the majority of the SFRC's creep behaviour would be due to fibre pull-out. Each beam was pre-cracked to a predetermined mid-span displacement of 3mm. This displacement corresponded to a total CMOD of 0.5mm on the tensile face of the SFRC beam specimens.

After pre-cracking, the beams were transported using an overhead crane to a climate controlled room. Three tested notched beams were stacked on top of one another to provide supports for each beam, as seen in Figure 19. The same span length of 2700mm, as in the pre-cracking phase, was used. A 10mm thick rubber strip was placed between the notched beam and reinforced beam, to ensure a suitable supporting condition.

Figure 19: Setup of the cracked reinforced beam creep tests.

A 50mm stroke dial gauge was used on both sides of each beam to manually measure the vertical mid-span displacement. The dial gauges were attached to steel tubing using PVC clamps. A 44×44×60mm wooden block was used to ensure that the PVC clamp was positioned at the correct height. A threaded steel bar along with two nuts were used to attach the PVC clamp and wooden block to the steel tubing. An L-shaped steel plate was used to connect the beam and dial gauge. The complete setup is shown in Figure 20.

Figure 20: Vertical mid-span displacement measurement setup.

The sustained load was applied to each beam using a combination of sand and 100kg lead weights. Wooden boxes were constructed to house the sand and weights. Two tested notched beams were used to place the wooden box on top of the reinforced beams, see Figure 19. The centre of each notched beam was placed 1100mm from each support, or 250mm from the mid-span. This setup was selected as it was the closest loading to emulate the central point load used in the pre-cracking phase.

3.3.1.4 Experimental Programme

A total of two beams each were made for the RC beams, SFRC beams and combination beams. All the beams were tested after 49 days of curing. The CMOD-displacement curves, obtained in the reinforced beam tests, were used to estimate the vertical displacement required for a CMOD of 0.5mm on the SFRC specimens. All the reinforced beams were pre-cracked to the same vertical displacement in order to ensure the comparability of the time-dependent results. A displacement rate of 1mm/minute was used. The elastic recovery of each beam was also captured. A damage model was generated in order to quantify the consequence of pre-cracking each specimen.

The cracked beam specimens were placed in a climate controlled room with a temperature of 22 ± 1°C and a relative humidity of 55 ± 5%. The sustained loading required for each beam was calculated using the flexural resistance curves obtained during the pre-cracking phase. The sustained flexural load applied in the beam creep tests was 40% of the maximum applied flexural load achieved by each specimen. After computing the long-

term flexural load required, the quantity of sand and lead weights was calculated. The weight of the wooden box, as well as the extra notched beams was also taken into account. Each beam was loaded over a period of one hour. The elastic response of each specimen, due to the loading was recorded.

The cracked reinforced beam creep test commenced as soon as the final addition of sand or lead weight. Dial gauge readings were taken once every 2 to 3 days for the first 100 days, and once a week from then on. For this study the first 120 days of creep data were analysed. The test will however continue to run for a period of one year. The humidity and temperature of the climate controlled room was also recorded each time readings were taken. The creep curve of each beam was reported.

3.3.2 Drying Shrinkage

The drying shrinkage strains of both fibre mixes were required in order to calculate the actual CMOD in the uniaxial tensile creep tests. The shrinkage behaviour was obtained with the use of the procedures described by the BS ISO 1920-8 (2009).

Three shrinkage beams, each measuring 100×100×500mm, were cast for both the SF30 and SF60 mixes. The same concrete batches used to cast the SFRC and combined creep beam specimens were used in casting the specimens. Demoulding took place after 24 hours of curing, after which the specimens were placed directly into curing tanks. The drying shrinkage tests were initiated at the same time as the uniaxial tensile creep tests, i.e. after 77 days of curing.

One pair of shrinkage targets was glued on each smooth face of a beam specimen. The casting face was avoided due to its uneven nature. A total gauge length of 100mm was ensured between the targets. The drying shrinkage specimens were then placed in an upright position, in the same climate control room used for the reinforced beam creep tests and uniaxial creep tests. A digital dial gauge was used to measure the relative deformation between the targets. A reference reading for each set of targets was recorded, after placing the specimens in the climate controlled room. Shrinkage readings were recorded every 2 to 3 days for a total of 120 days. The reference reading was subtracted from each subsequent shrinkage reading for each target. The value obtained was then divided by the gauge length in order to calculate the drying shrinkage strain. The average strain of all nine pairs of targets, for each fibre dosage, was calculated and reported.

3.3.3 Uniaxial Tensile Creep Test

3.3.3.1 Overview

The primary objective of the uniaxial tensile creep test was to obtain the CMOD rates of pre-cracked SFRC specimens, due to a sustained uniaxial tensile loading. The CMOD rates were an essential input for the time-dependent modelling of this research. The testing setup and procedure used in this research was based on that previously performed by Nieuwoudt et al. (2017).

In this test SFRC specimens were pre-cracked to a predetermined average CMOD of 0.2mm. The specimens were then moved to creep frames and a sustained long-term uniaxial load was applied. The creep frames were situated in a climate controlled room with a temperature of 22 ± 1°C and a relative humidity of 55 ± 5%. A sustained loading of 40% of the ultimate tensile strength of each specimen was used in this research. The CMOD due to the sustained loading was recorded.

3.3.3.2 Test Specimens

The moulds used to cast the SFRC specimens were the same as those used by Mouton (2012). Steel hooks, used to provide anchorage, were cast in at both ends of a standard beam mould with dimensions 100×100×500mm. The hooks were designed with eye-like loops at their ends to provide a pinned attachment point, see Figure 21.

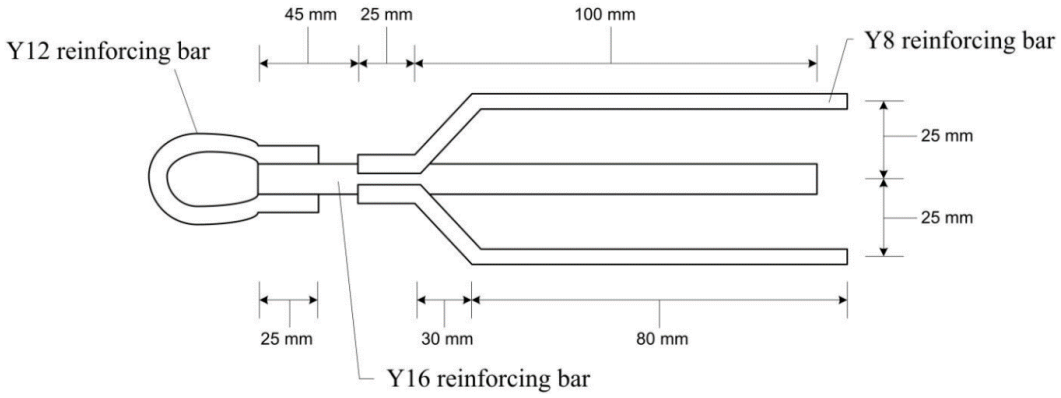

Figure 21: Design and dimensions of steel hooks (Mouton, 2012).

The moulds were oiled with mould release oil prior to the addition of the steel hooks. A wooden block measuring 100×100×200mm, with an 18mm diameter central hole was used to hold each steel hook in position. The wooden block was cut in half to allow the placement of the hook in the central hole. Additional wooden blocks, along with a spirit level, were used to ensure that the steel hooks were correctly aligned. Binding wire was then tied around each hook and attached to a supporting crossbar. This was done to ensure that the alignment of each hook was maintained when adding and vibrating the concrete mix. The additional wooden blocks were then removed. The full process is outlined in Figure 22.

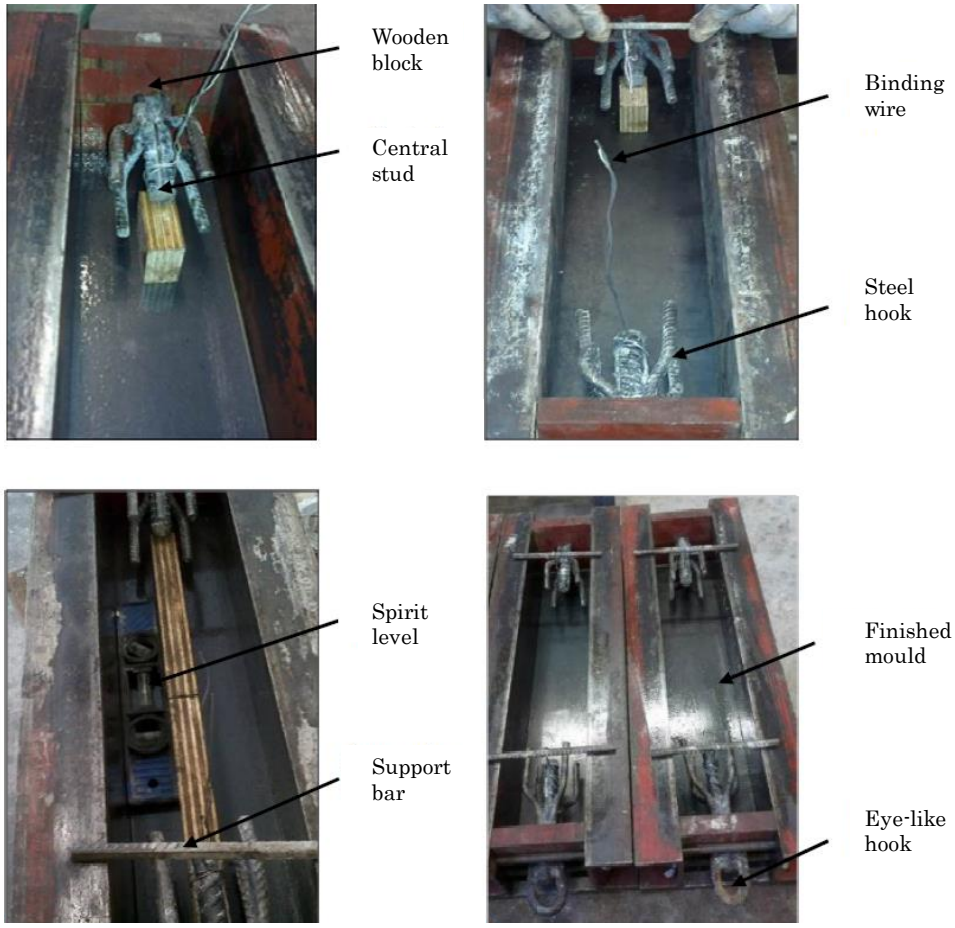

Figure 22: Preparation of uniaxial tensile creep test moulds (based on Babafemi, 2015).

The uniaxial creep specimens were cast from the same concrete batches used to cast the creep beam specimens. The moulds were filled in two layers. Fibre concrete was initially added in the middle portion of the mould and allowed to vibrate for about 30 seconds. This allowed the concrete to flow in between the steel hooks. The second layer of concrete was

then added immediately after and vibrated for another 30 seconds. The casting face was then levelled off with a trowel. The specimens were demoulded after 24 hours of curing and placed in curing tanks. Each uniaxial creep specimen was notched three days before testing. A 10mm deep peripheral notch was made in the centre of each specimen, using a 3mm thick diamond blade. The purpose of the notch was to control where cracking occurred and resulted in an effective cross-section of 6400mm^2 in the notched zone. The specimens were then placed back in the curing tanks and removed two hours before the pre-cracking test commenced.

3.3.3.3 Experimental Methodology

The pre-cracking phase of the uniaxial tensile creep specimens was performed using a 500kN Instron hydraulic actuator. Two steel plates were attached to the testing machine and a stiffened beam, used as a base, with four 16mm diameter bolts. The stiffened beam was anchored to the concrete floor with pre-stressed bolts. An additional 10mm thick vertical steel plate, with a 22mm diameter central hole was welded to the centre of each base plate. The central hole was used to link the eye-like loops on the steel hooks to the supports. Two 20mm diameter bolts along with two 10mm thick plates were used as the links, as seen in Figure 23. This type of connection was used to ensure that no moment developed at each support.

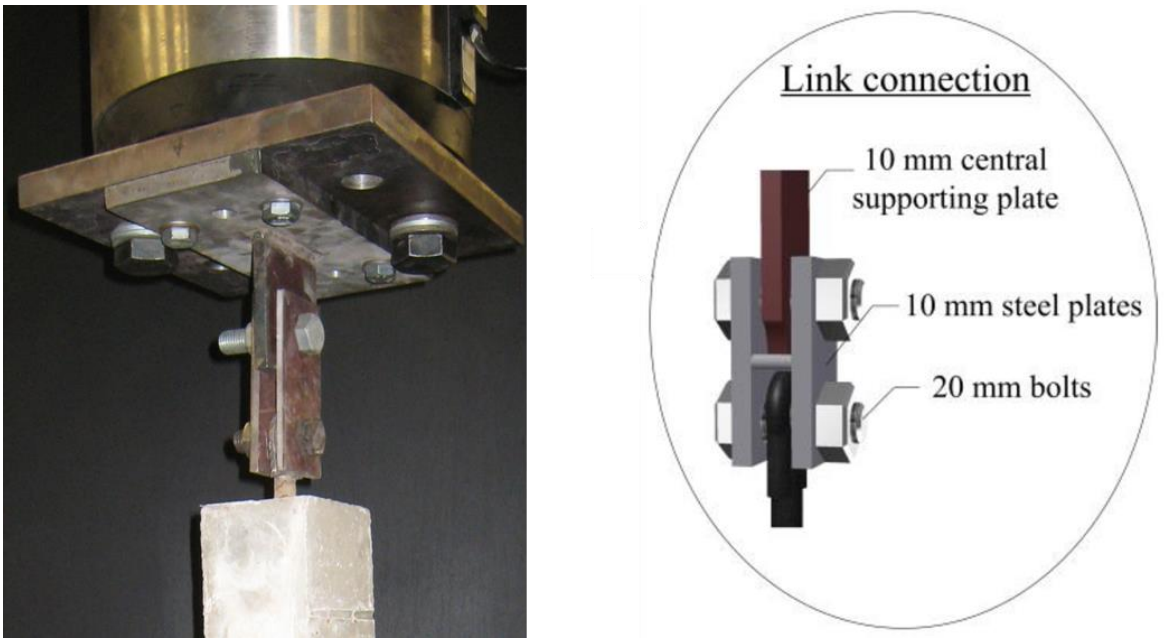

Figure 23: Steel base and link connection used to attach the uniaxial tensile creep specimens to the supports (based on Nieuwoudt, 2016).

The SFRC specimens were pre-cracked to an average CMOD value as close to 0.2mm as possible. Obtaining this value was challenging due to the large energy build up in the testing setup, when trying to crack a specimen. Once a crack forms, the energy built up is rapidly released. This energy is dissipated by widening the existing crack and thus, depending on the magnitude, can result in an instantaneous crack larger than 0.2mm. If this outcome occurred in the pre-cracking of a specimen, the test was immediately terminated and the average CMOD reported. This can however be overcome by using a faster reacting close loop system or increasing the stiffness of the setup.

An average CMOD of 0.2mm was selected to simulate an average CMOD value present in the pre-cracked beam specimens. This was necessary in order to obtain the average rate of fibre pull-out creep over the creep beam's crack. This rate of pull-out could then be used to generate a model predicting the results of the cracked reinforced beam creep test.

In previous research (Nieuwoudt et al. 2017) only two LVDTs were used to measure the CMOD when pre-cracking each test specimen. This has however come under criticism, as the crack developed in SFRC uniaxial tensile specimens often only opens in one half of the specimen, creating a hinge effect (also referred to as fish-mouthing). It is therefore recommended that a minimum of three LVDTs are used. For this research a total of four LVDTs were used for measuring the CMOD of each specimen. The main reason for the additional LVDT was due to the four-sided nature of the beam specimen. An LVDT was therefore placed near each corner of the specimen, as seen in Figure 24. A removable aluminium frame, with a gauge length of 100mm, was used to attach the LVDTs to the specimen. A circuit board that allowed the automatic average CMOD output of the four LVDT's was developed for this test. This was necessary in order to accurately pre-crack each specimen to a predetermined average CMOD using a closed loop system. The average CMOD output, as well as the load cell readings of the Instron, were recorded with an electronic data acquisition system. The full pre-crack setup is shown in Figure 24.

The test setup was pre-loaded to a value of 1kN, to ensure that the link connections between the specimen and the supports were sufficiently stiff. A CMOD rate of 0.01mm/second was then applied. Once the specimen had reached the required CMOD value the loading was removed. The elastic recovery of each specimen was also captured. The test was terminated once the specimen had unloaded to a value of 1kN. The stress-CMOD curve of each specimen was used to obtain the ultimate tensile stress resistance. This value was then multiplied by a factor of 0.4, in order to obtain the long-term sustained axial tensile stress required.

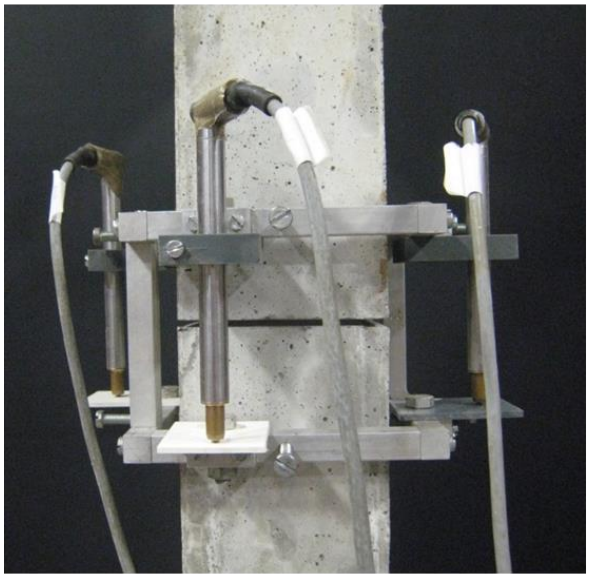

Figure 24: LVDT arrangement and full setup used in the uniaxial pre-cracking phase.

After pre-cracking, each test specimen was transferred to a creep frame. The creep frames, erected by Mouton (2012), were used for the sustained loading setup. A schematic representation of a creep frame is presented in Figure 25. The sustained load was applied by free hanging weights attached to two pivot beams. A stopper mechanism was used to ensure that the specimens could be inserted into the frames load free. After a specimen had been inserted, the stopper was unscrewed and the sustained load was transferred to the specimen. The stopper also functioned as a safety mechanism, in the case of a sudden drop of one of the pivot beams. The same links that were used in the pre-cracking phase of this test were used to attach the specimen to the supports.

The creep frames had to be calibrated to apply the necessary tensile load to each specimen. The calibration process was performed with a 50kN tensile load cell and a Spider8 data acquisition system. The load cell was attached to the creep frames in the position where

the specimens were to be attached. The frame's pivot beams were positioned by the stopper mechanism so that no load was transferred to the load cell. The load cell was then zeroed by the software program and the data acquisition commenced. The stopper mechanism was released and weights were placed on the cables connected to each pivot beam. Once the correct load output, within a tolerance of 0.1kN, had been reached, the test was terminated. The stopper mechanism was then returned to the positon were no load was transferred to the load cell. The load cell was then removed.

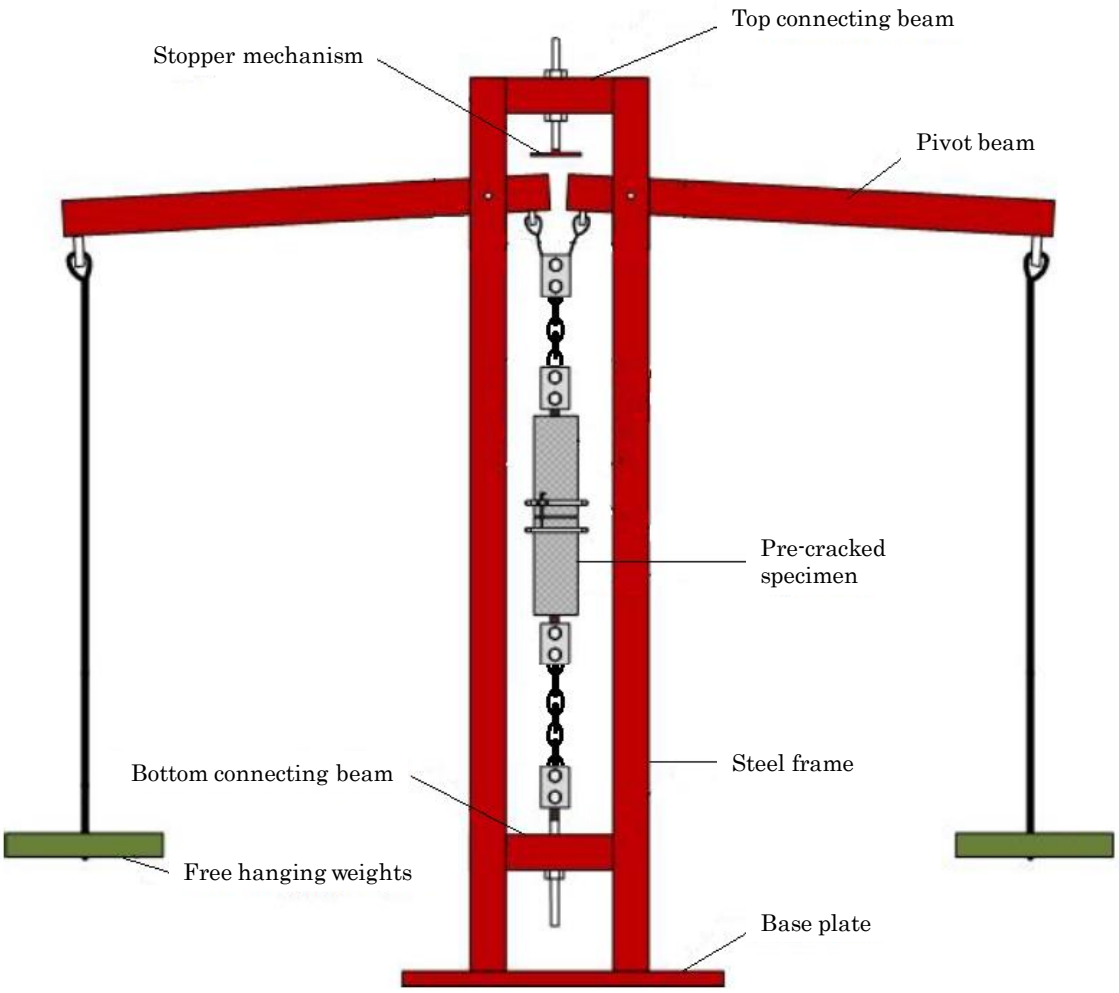

Figure 25: Schematic representation of the creep frames used in the uniaxial tensile creep tests (based on Nieuwoudt, 2016).

The displacement readings, taken over the pre-cracked notch, were obtained with a similar setup to that used in the pre-cracking phase. Four LVDTs each with a stroke length of 10mm were used. A removable aluminium frame, with a gauge length of 70mm, was used to attach the LVDTs to the specimen. The frame can be seen in Figure 26.

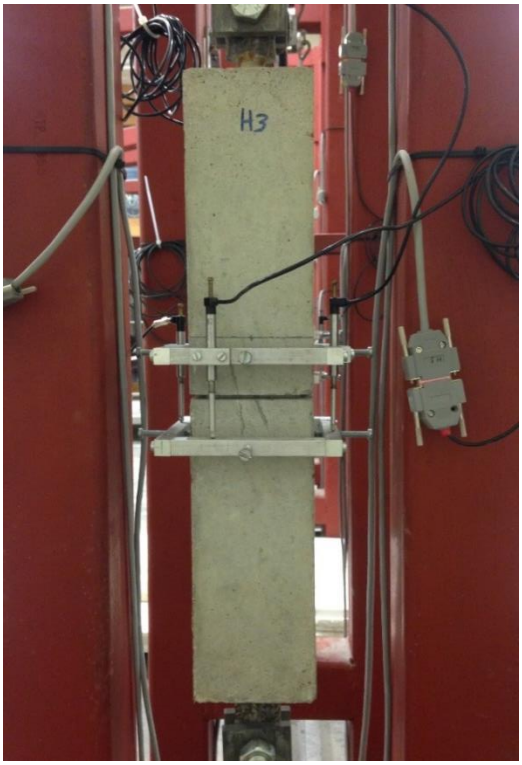

Figure 26: Removable aluminium frame used in the uniaxial tensile creep tests.

Once each specimen was securely attached to the creep frame, the LVDTs were positioned in the aluminium frame. A Spider8 data acquisition system was used to record each LVDT reading. The acquisition system was initiated before any of the loads were applied, at a rate of one reading/second for the first 30 minutes of the test. Each specimen was loaded by slowly releasing the stopper mechanism over a period of 60 seconds. The sample frequency rate was then reduced to one reading/hour for the rest of the test.

3.3.3.4 Experimental Programme

Two specimens were made for the SF30 and SF60 concrete mixes, respectively. Each was cast from the same batches used for the cracked reinforced beam creep tests. All the uniaxial creep specimens were pre-cracked after 77 days of curing. Ideally the specimens would have been pre-cracked at the same age as the creep beams, i.e. 49 days. This unfortunately was not possible as the creep frame setup took longer than anticipated. The extra 28 days of curing were however not predicted to cause any noticeable differences in the time-dependent results. The axial tensile stress-CMOD curve obtained during the pre-cracking phase was reported, along with the subsequent permanent deformations.

A sustained load level of 40% of the ultimate tensile strength was used for each sample. This was unconventional, as the post-crack residual strength is more commonly used. The reason for this, was to keep the method of calculating the sustained loads of both the beam and uniaxial creep tests consistent. The creep frames were situated in a climate controlled room with a temperature of 22 ± 1°C and a relative humidity of 55 ± 5%. The specimens were not sealed and therefore a combination of basic creep, crack widening, drying creep and drying shrinkage occurred. The drying shrinkage values of each concrete type were measured separately. These values were added to the recorded CMOD to obtain the actual CMOD of each sample. This is shown graphically in Figure 27.

The instantaneous elastic deformation of each sample, as a result of the sustained tensile load, was recorded. For this research, a total of 120 days of uniaxial tensile creep data was captured for each specimen. The test will however continue to run for one year. The CMOD-time curves obtained from the four LVDTs and shrinkage results of each specimen were analysed and the average plotted. The two average CMOD-time curves were then used to obtain an overall average CMOD-time curve for each steel fibre dosage. A power trend line of the each average was then plotted in order to predict the CMOD at any given time. This type of equation was selected as it is used by the *fib* Model Code (2010) in predicting the creep behaviour of normal concrete. Each SFRC's uniaxial creep power equation was used in the time-dependent modelling section of this study.

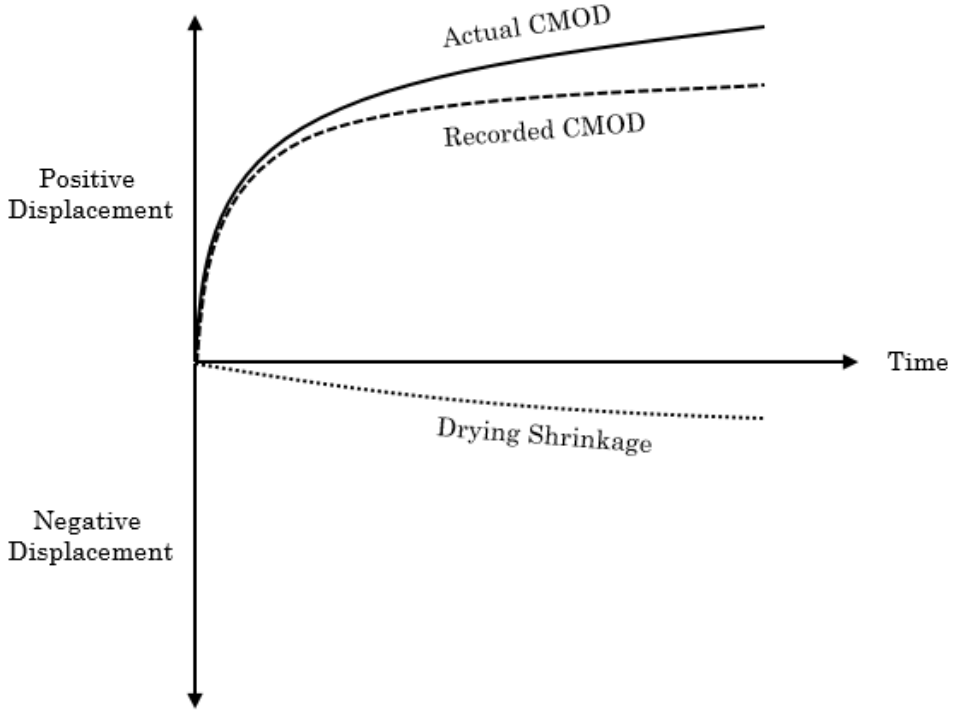

Figure 27: Difference between recorded CMOD and actual CMOD values.

3.4 Concluding Summary

This chapter presented a description of the concrete mixes used, and the tests performed to obtain the mechanical and time-dependent properties of the applicable materials. A detailed description each test was provided along with its experimental programme.

Standardised compressive and tensile resistance tests were performed to obtain design values for the specific materials. The composite behaviour of these materials was also investigated by means of the reinforced beam tests.

An investigation into the uniaxial and flexural time-dependent behaviour of SFRC was performed. The results and discussions of each test are presented in Chapters 5 and 6.

Chapter 4
Reinforced Beam Design

4.1 Flexural Beam Design

One flexural beam design method is used to design all three types of reinforcing beams, namely: the SFRC, combined, and conventionally reinforced beams. The method used is a combination between the BS EN 1992-1-1 (2004) and the *fib* Model Code (2010). The design comprises of same fundamentals used in normally reinforced concrete, with the tensile resistance of fibres added. The partial material factors used in the design codes are ignored. The *fib's* rigid-plastic model is used in calculating the tensile resistance of the fibres.

Consider a combined steel fibre and steel bar reinforced beam section subject to a bending moment, as presented in Figure 28. The design moment *(M_d)* is calculated by taking the moment of the internal forces (*F_c, F_{sf}* and *F_s*) about the Neutral Axis (NA):

$$M_d = F_c \cdot \left(x - \frac{\lambda x}{2}\right) + F_s \cdot (d - x) + F_{sf} \cdot \left(\frac{h - x}{2}\right) \tag{4-1}$$

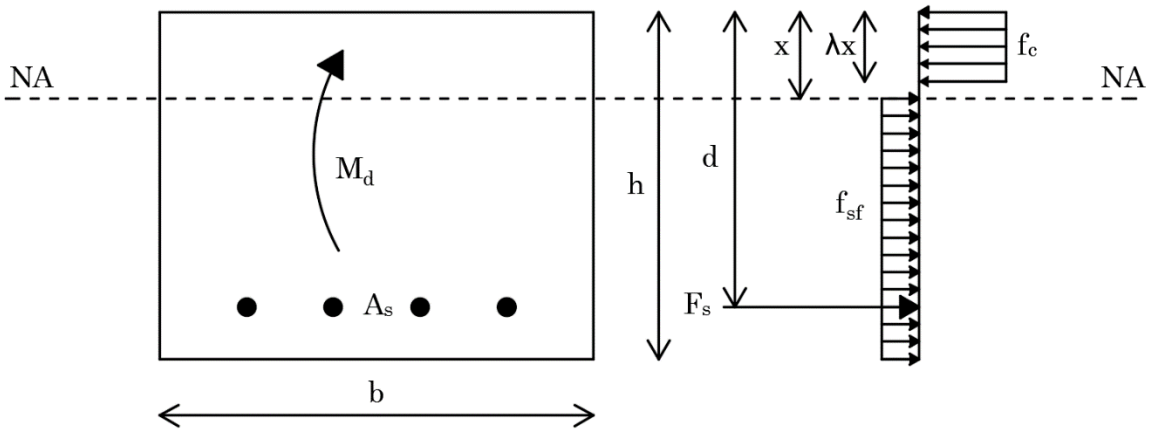

Figure 28: Beam section used for flexural design.

where: F_c is the concrete's internal force, F_s is the reinforcing bar steel's internal force, F_{st} is the steel fibre section's internal force, x is the position of the neutral axis, λ is the effective height of the compression zone, d is position of the reinforcing bar steel, and h is the beam's total height.

The internal forces within the section are calculated using the stresses in the concrete and reinforcement, and their respective areas. A rectangular compression stress block is assumed for the concrete. A factor λ is used to express the effective height of the compression zone. The BS EN 1992-1-1 (2004) defines this factor as 0.8 for concrete with a compressive cylinder strength of less than 50MPa. The internal force of the concrete is therefore given by:

$$F_c = f_c \cdot \lambda x \cdot b \tag{4-2}$$

where: f_c is the concrete's 28 day compressive cylinder strength, and b is the breadth of the beam section. The rigid-plastic model used in the *fib* Model Code (2010) defines a rectangular tensile stress block for the steel fibre reinforcing. The height of this tensile zone is calculated using the residual flexural tensile strength obtained in the BS EN 14651 (2005). The tensile resistance of steel fibre reinforcing is determined as:

$$f_{sf} = \frac{f_{r3}}{3} \tag{4-3}$$

where: f_{r3} is the residual flexural tensile strength at a CMOD of 2.5mm. The internal force of the steel fibre reinforcing is therefore given by:

$$F_{sf} = f_{sf} \cdot (h - x) \cdot b \tag{4-4}$$

The internal force due to the steel bar reinforcing is calculated with:

$$F_s = f_y \cdot A_s \tag{4-5}$$

where: f_y is the tensile yield stress of reinforcing bar steel, and A_s is the total cross-sectional area of reinforcing bar steel in the beam.

The horizontal equilibrium of the internal forces was used to determine the position of the neutral axis:

$$F_c = F_s + F_{sf} \tag{4-6}$$

Once the position of the neutral axis is known, Equation (4-1) can be applied to calculate the design moment M_d of the beam.

This method was used in its entirety when considering the design of the combined beams used in this research. In designing of the SFRC beams the resistance of the reinforcing bar steel was set to zero, and in the RC beams the steel fibre reinforcing resistance was set to zero. The flexural design values obtained for each beam type were compared to the results obtained in both the reinforced beam tests and the cracked reinforced beam creep tests.

4.2 Concluding Summary

The flexural behaviour of SFRC and RC can be predicted with the use of design codes. The BS EN 1992-1-1 (2004) and *fib* Model Code (2010) were applied in this chapter to setup a design method to calculate the flexural resistance of beams with both steel fibre reinforcing and reinforcing bar steel. The design values were used to compare the predicted structural behaviour of the reinforced beams to the experimentally obtained values.

Chapter 5
Results and Discussion: Mechanical Behaviour

5.1 Compressive Strength

The compressive strengths as tested per Section 3.2.1 of the normal and steel fibre reinforced concrete are presented in Table 2, along with each value's Coefficient of Variance (CoV). The strength gain of all the concrete mixes was fairly rapid, with each mix obtaining approximately 90% of its 28 day compressive strength within 7 days. This early age characteristic was highly advantageous when considering the applied stresses arising from demoulding the reinforced beams, discussed in Section 3.2.6.

Table 2: Average 7 and 28 day compressive strength of the concrete mixes.

Compressive Strength	NC	SF30	SF60
7 Day Average [MPa]	38.8	40.8	45.1
7 Day CoV	4.0%	6.8%	3.9%
28 Day Average [MPa]	42.6	45.9	51.0
28 Day CoV	6.5%	7.3%	4.2%

The addition of 30kg/m^3 and 60kg/m^3 of 3D-60mm steel fibres resulted in an increase of 8% and 20% in 28 day compressive strength, respectively. This increase is as a result of the increased toughness that longer steel fibres provide (Ou, 2012). Each mix obtained a CoV below 10% for both the 7 and 28 day strengths. This indicates a good repeatability and consistency of each mix. The values shown in Table 2 were used as the compressive design strength used in the reinforced beam design.

5.2 Density

The densities obtained by the compressive strength test cubes are shown in Table 3. It can be seen that the addition of fibres to the mix increased the densities marginally. This is due to the higher density of the steel fibres, in comparison to that of the cement paste and aggregates.

Table 3: Average density of the 28 day compressive cubes.

Density	NC	SF30	SF60
Average [kg/m^3]	2298	2324	2419
CoV	0.8%	1.2%	1.4%

5.3 Modulus of Elasticity

The modulus of elasticity test results are provided in Table 4. The addition of fibres had no effect on the elastic modulus of the mixes. This was expected as the modulus of elasticity is determined prior to cracking and therefore the fibres have not been activated yet (Ou, 2012). The elastic modulus value used to model the different concretes in Chapter 7 was taken as 37.5GPa for all three mixes due to the similar averages, as well as acceptable CoVs.

Table 4: Average elastic modulus of the concrete mixes.

Modulus of Elasticity	NC	SF30	SF60
Average [GPa]	37.6	37.6	37.4
CoV	3.9%	0.4%	2.2%

5.4 Reinforcing Bar Tensile Strength

The reinforcement used in this study was 6mm diameter ribbed high tensile steel supplied by D&E Steel, Western Cape. The small diameter steel was selected to allow easy manipulation of the amount of reinforcement in both the RC beams, and combined steel fibre and reinforcing bar steel beams. This was necessary in order to accurately match the flexural design capacity of the SFRC beams.

Figure 29 shows the stress-strain relationship used to obtain the elastic modulus and yield stress of the steel. The line used to find the yield stress of the steel was initially required to begin at an x-intercept of 0.002. This was however offset due to the preload force used to hold the bar in place before the test had commenced.

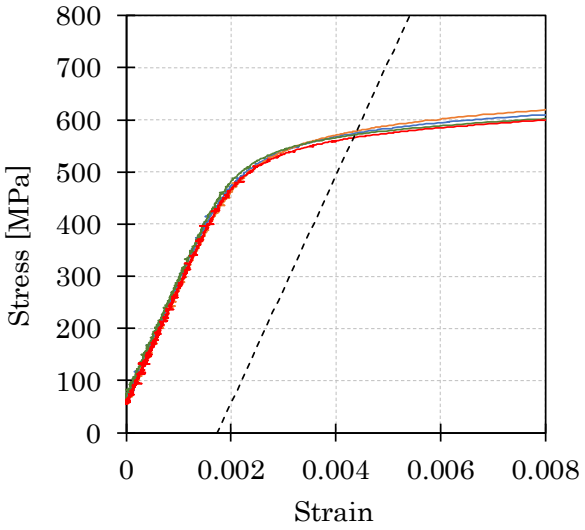

Figure 29: Stress-strain relationship of reinforcing bars.

A digital calliper was used to measure the diameter of each steel bar, between the ribs. An average diameter of 5.8mm was recorded and this value was used when calculating the elastic modulus and yield stress of the steel. The steel properties of the reinforcing bars are summarised in Table 5. It should be noted that the stress in the reinforcing bars continued to increase after the yield stress value, as defined by the ASTM E8/E8M-09 (2009), was reached.

Table 5: Diameter, elastic modulus and yield stress of reinforcing bars.

Steel Properties	Diameter [mm]	E_s [GPa]	f_y [MPa]
Average	5.8	218	580
CoV	5.0%	2.8%	0.8%

5.5 Notched Beam Test

The notched beam test was conducted to investigate the mechanical post-cracking behaviour of the SFRC, as well as to obtain the steel fibre design values. Fifteen specimens

were tested for each fibre dosage, twelve specimens from the notched beam test and three specimens cast with the reinforced beam test. A specimen for both the SF30, and SF60 mix cracked outside the notch and the subsequent results were rejected. None of the specimens failed due to the rupture of the steel fibres. The average residual flexural tensile strengths are presented in Table 6, along with the resulting stress-CMOD curves, Figure 30 and Figure 31. Both mixes obtained satisfactory overall residual strength capacity.

Table 6: Average residual flexural tensile strength values for SFRC mixes.

Residual Flexural Tensile Strength	*LOP*	f_{r1}	f_{r2}	f_{r3}	f_{r4}
SF30 Average [MPa]	4.48	3.95	4.47	4.48	4.36
SF30 CoV	7.8%	23.2%	24.7%	24.0%	24.7%
SF60 Average [MPa]	5.30	6.50	7.01	6.87	6.39
SF60 CoV	10.2%	26.5%	25.2%	23.3%	23.5%
CMOD [mm]	≤ 0.05	0.5	1.5	2.5	3.5

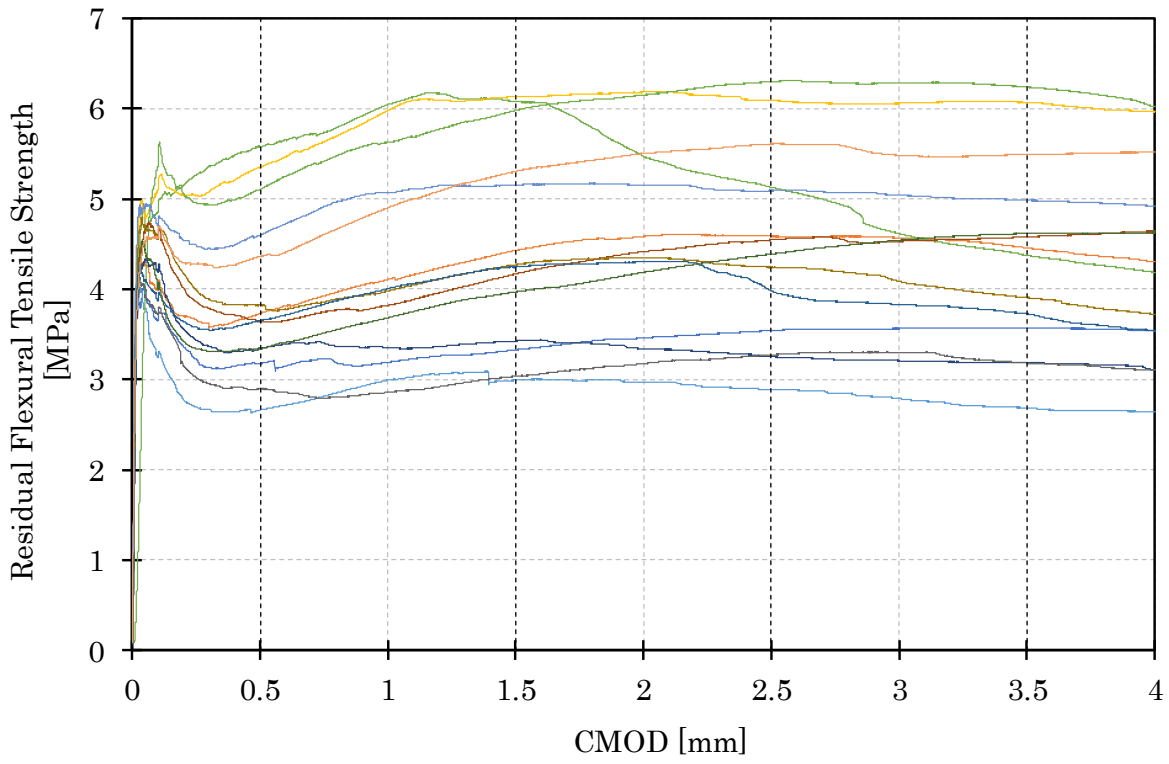

Figure 30: Residual flexural tensile strength vs. CMOD of the SF30 mix.

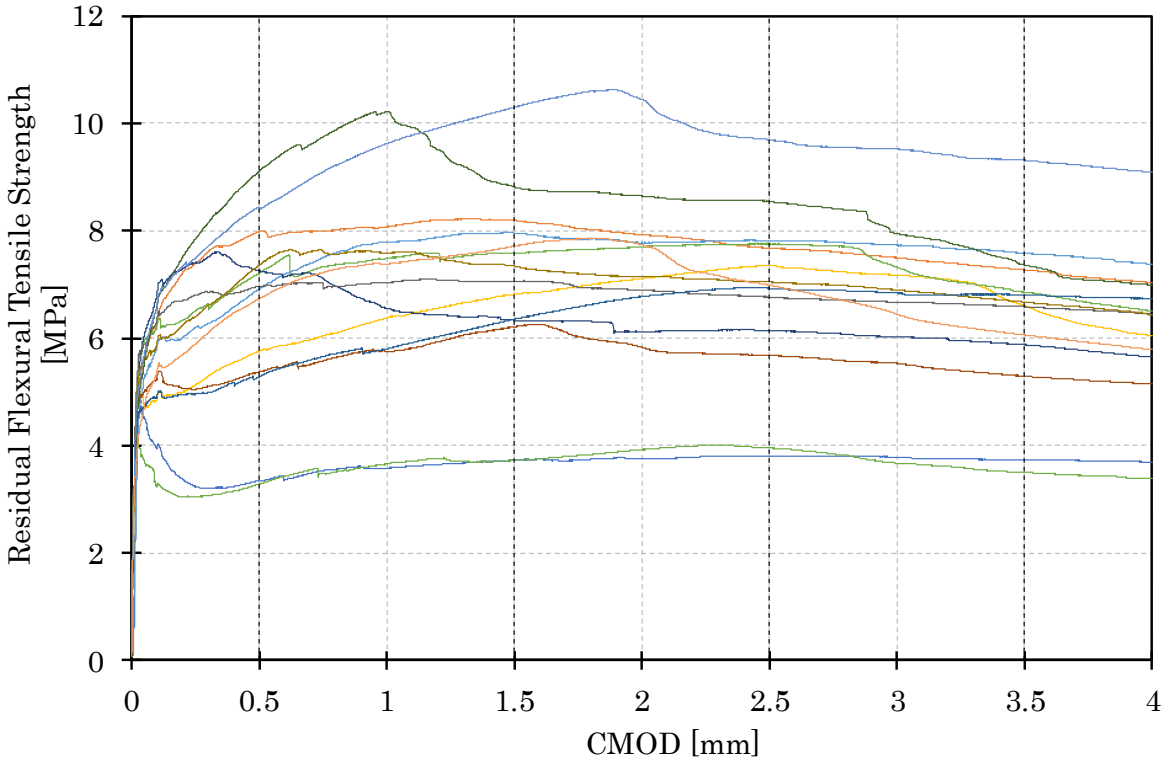

Figure 31: Residual flexural tensile strength vs. CMOD of the SF60 mix.

The majority of the SF30 specimens demonstrated deflection softening behaviour, while the majority SF60 specimens displayed deflection hardening. This suggests that the critical fibre volume of the concrete mix, as described in Section 2.1.2.2, exists between a fibre dosage of 30kg/m^3 and 60kg/m^3. There were however a few specimens in both mixes that displayed the opposite behaviour. This is likely a consequence of the varied fibre distribution of SFRC, which results in some specimens containing more or less fibres bridging the crack than others.

The average residual strengths obtained for the SF30 mix were similar to the LOP value. This is an indication that on average, there are a sufficient number of fibres bridging the crack. The average residual strengths obtained for the SF60 mix were all larger than LOP value, due to the higher volume of fibres. Both mixes showed excellent ductility as the residual strengths were maintained at large crack widths.

Steel fibre reinforced concrete's shortcoming can be seen in the coefficient of variance values obtained by both mixes. The large variability of results can generally be attributed to the mixing and casting procedures used. These factors significantly affect the distribution of the fibres. Vibration with a poker vibrator can result in unfavourable fibre

distribution, while a vibrating table can be used to improve the distribution. Due to this, the use of SFRC may be better suited to a precast application, where large vibrating tables can be used for compaction. If however SFRC is to be applied to in situ construction, a thorough understanding of the material's performance is required. The current partial safety factor prescribed by the *fib* Model Code (2010) for SFRC design is 1.5 for ultimate limit state. This factor may need to be revised, or an extra reliability factor added, in order to account for the casting procedure used.

5.6 Reinforced Beam Test

The structural performance of SFRC was investigated and compared to that of conventionally reinforced concrete. The design method presented in Chapter 4 was used to obtain the design values shown in Table 7. The RC and combined beams were designed to obtain similar flexural capacities as the SFRC. This was acquired by adjusting the number of 6mm diameter reinforcing bars in both beams. The difference in flexural design strength, in comparison to that of the SFRC beam, is also provided in Table 7. A concrete cover of 20mm was used in the design. The densities and compressive strengths used in the beam calculations were obtained from the control cubes cast with each beam specimen. The average compressive cube strengths were multiplied by a factor of 0.8 to obtain the cylinder strength, when used in the design (BS EN 1992-1-1, 2004). The experimental flexural behaviour was represented by the bending moment-deflection curve obtained at mid-span. The ultimate experimental bending moment (M_r) was taken as the maximum bending moment recorded for the each beam specimen.

Table 7: Design bending moments for the reinforced beam tests.

Specimen	$f_{cm,cube}$ [MPa]	No. Bars	Design Moment [kN.m]	% Difference
SFRC Beam	51.0	0	15.80	
RC Beam	42.6	7	16.14	2.2%
Combined Beam	45.9	2	14.94	-5.4%

5.6.1 RC Beams

5.6.1.1 General Behaviour

The behaviour of reinforced concrete elements can be divided into distinct events, shown in Figure 32. The first event is the cracking of the concrete (A). This is then followed by the yielding of the tensile reinforcement (B). The steel continues to yield until the concrete in the compression zone is crushed (C), representing the ultimate load achieved. This is then followed by the failure of the beam (C') to (D).

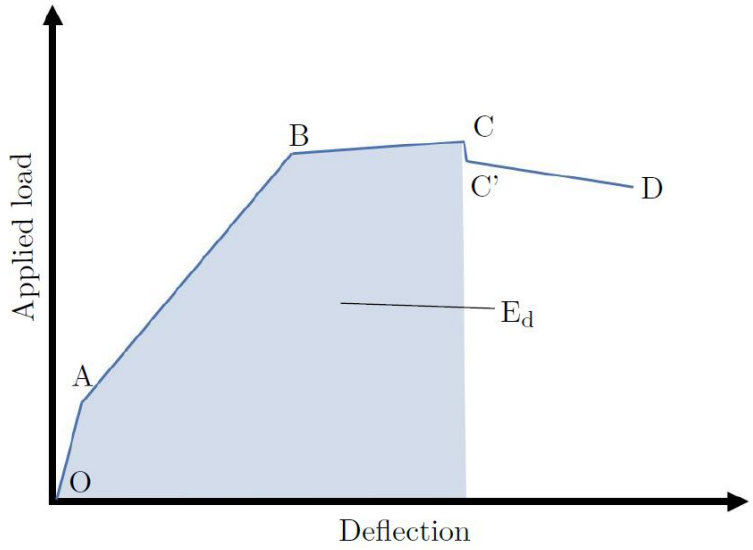

Figure 32: Idealised load-deflection curve at mid-span (Robberts & Marshall, 2010).

The bending moment-deflection curves for all three RC specimens are presented in Figure 33. The beam's flexural response was comparable to that expected in Figure 32. The beam tests were however terminated before concrete crushing occurred. Similar responses were obtained by all three RC beam specimens, exhibiting the good repeatability of reinforced concrete. The RC beams cracked at an average bending moment of 10.1kN.m and the steel yielded at approximately 17kN.m. RC Beam 2 was tested to a maximum mid-span deflection of 39.7mm, at which the steel continued to yield. This displays the reinforcing bar steel's beneficial ductile behaviour. The RC beams' design and experimental bending moments are presented in Table 8.

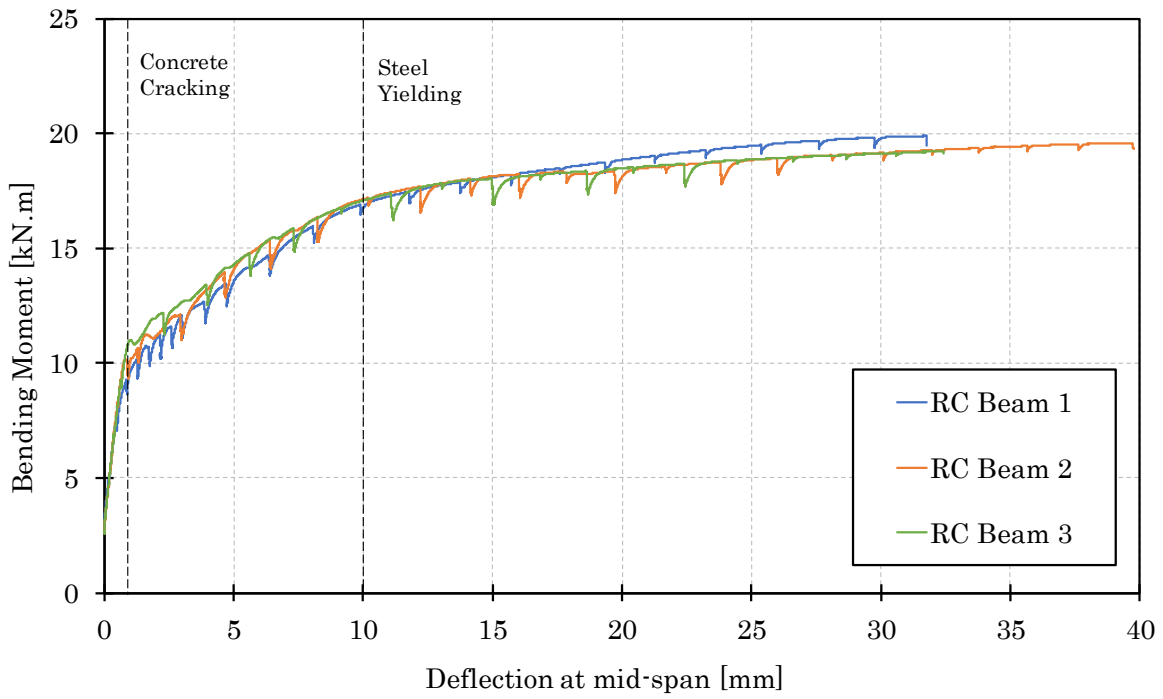

Figure 33: Bending moment-deflection curves for RC beams.

Table 8: Comparison of design and experimental bending moment values for RC beams.

Specimen	Density	$f_{cm,cube}$	Ultimate Bending Moment [kN.m]		
	[kg/m^3]	[MPa]	Design (M_d)	Experimental (M_r)	% Error
RC Beam 1	2298	41.2	16.14	19.89	23.2%
RC Beam 2	2320	41.0	16.14	19.59	21.4%
RC Beam 3	2317	42.6	16.15	19.23	20.8%

As can be seen in Table 8, the bending moments achieved by the tested beams where substantially larger than the design values. This consequence is hypothesised to be due to the yield stress defined by the ASTM E8/E8M–09 (2010). The stress-strain curves of the reinforcing bars, obtained in the reinforcing bar tensile strength tests, were therefore replotted in order to observe the extended behaviour of the steel. This behaviour is shown in Figure 34.

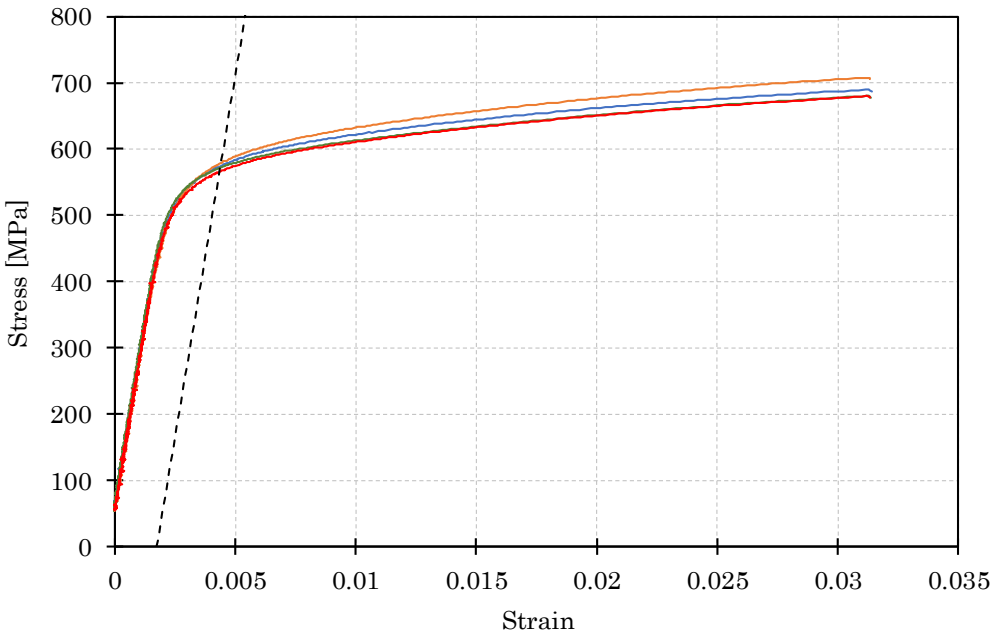

Figure 34: Extended stress-strain relationship of reinforcing bars.

Figure 34 shows that the yield stress value defined by the ASTM E8/E8M–09 (2010) is not applicable to the steel bars used in this research. The steel bars begins to yield at a stress of approximately 490MPa but continue to increase gradually in stress, as the strain increases. Each test was terminated at a total strain of 0.031mm/mm, once the extensometer had reached its full travel. At this value the steel still exhibited a slight increase in stress. For the purpose of this research the stress at this point was taken as the reinforcing bar steel's ultimate stress. The average ultimate stress and CoV is presented in Table 9.

Table 9: Yield stress and ultimate stress of reinforcing bars.

Steel Properties	f_y [MPa]	f_u [MPa]
Average	580	689
CoV	0.8%	1.9%

The design values were recalculated using the reinforcing bar's ultimate stress instead of its yield stress. The recalculated values can be seen in Table 10. The updated design values were far more comparable to those obtained in the test, with an average error of only 3.0%. The flexural design method used in this study was therefore verified. The ultimate stress of the reinforcing bars was used in all subsequent designs for this reason.

Table 10: Recalculated design and experimental bending moment values for RC beams.

Specimen	Density [kg/m³]	$f_{cm,cube}$ [MPa]	Ultimate Bending Moment [kN.m]		
			M_d	M_r	% Error
RC Beam 1	2298	41.2	19.09	19.89	4.2%
RC Beam 2	2320	41.0	19.09	19.59	2.6%
RC Beam 3	2317	42.6	19.11	19.52	2.1%

5.6.1.2 Crack Formations

The crack patterns observed, once RC Beams 2 and 3 had been tested, are shown in Figure 35 and Figure 36, respectively. The crack widths were measured just prior to unloading, and the largest crack width measured was 2.5mm on both beams.

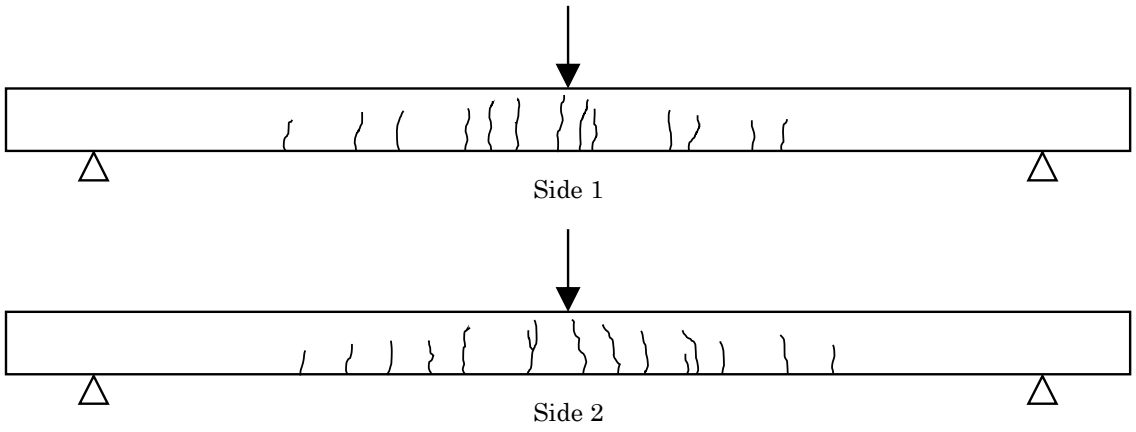

Figure 35: Crack patterns for RC Beam 2.

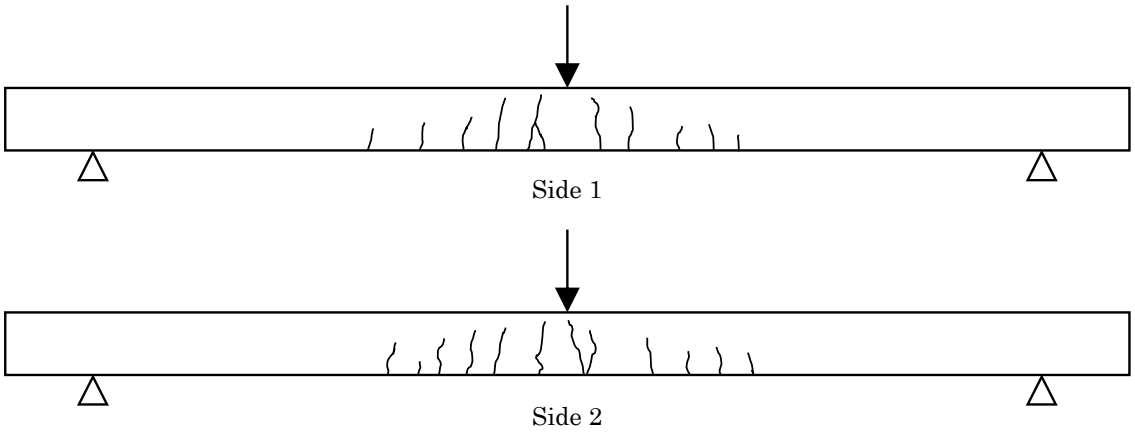

Figure 36: Crack patterns for RC Beam 3.

Initially cracking occurred near the mid-span of each beam. These primary cracks propagated spontaneously to a height just below the neutral axis. As the load increased, cracks began developing further from the applied load, while the existing cracks continued to propagate. These secondary cracks are a result of the redistribution of internal stresses. The tensile stress in the steel is at a maximum at a crack, and the concrete's stress is at a maximum between cracks. Once the stress reaches the tensile capacity of the concrete a crack forms. This relationship is shown in Figure 37. Both beams displayed cracking patterns typically expected for reinforced concrete. The RC Beam 2 had noticeably more cracks that RC Beam 3 due to the extra 7.4mm mid-span deflection it had undergone.

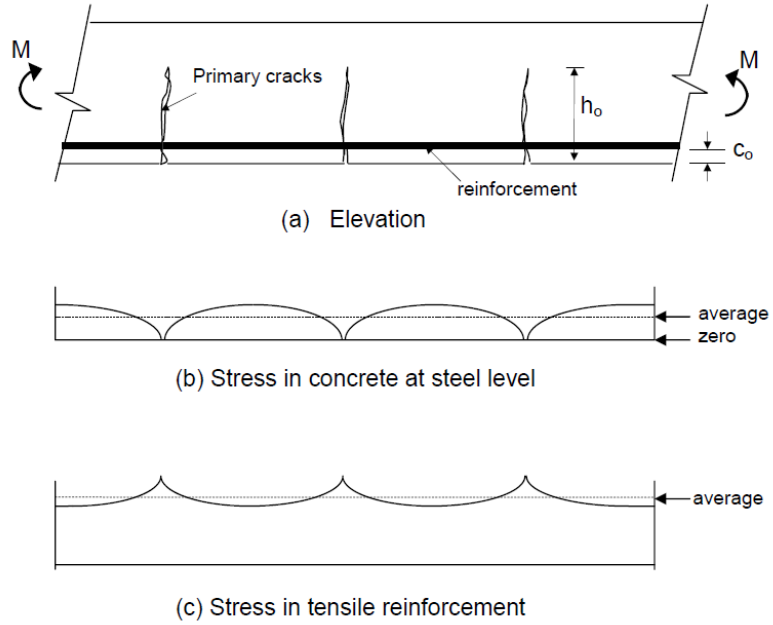

Figure 37: Stresses in a cracked reinforced concrete member (Gilbert & Nejadi, 2004).

5.6.2 SFRC Beams

5.6.2.1 General Behaviour

The flexural behaviour obtained by the reinforced beams with only steel fibre reinforcing is shown in Figure 38. By definition the beams exhibited slight deflection hardening behaviour, although only a minor increase in flexural resistance was observed once cracking had occurred. This suggests that the fibre dosage of 60kg/m^3 was only slightly less than the critical fibre dosage of the concrete mix. The average residual flexural strength obtained for each beam was in general similar to that of the cracking resistance.

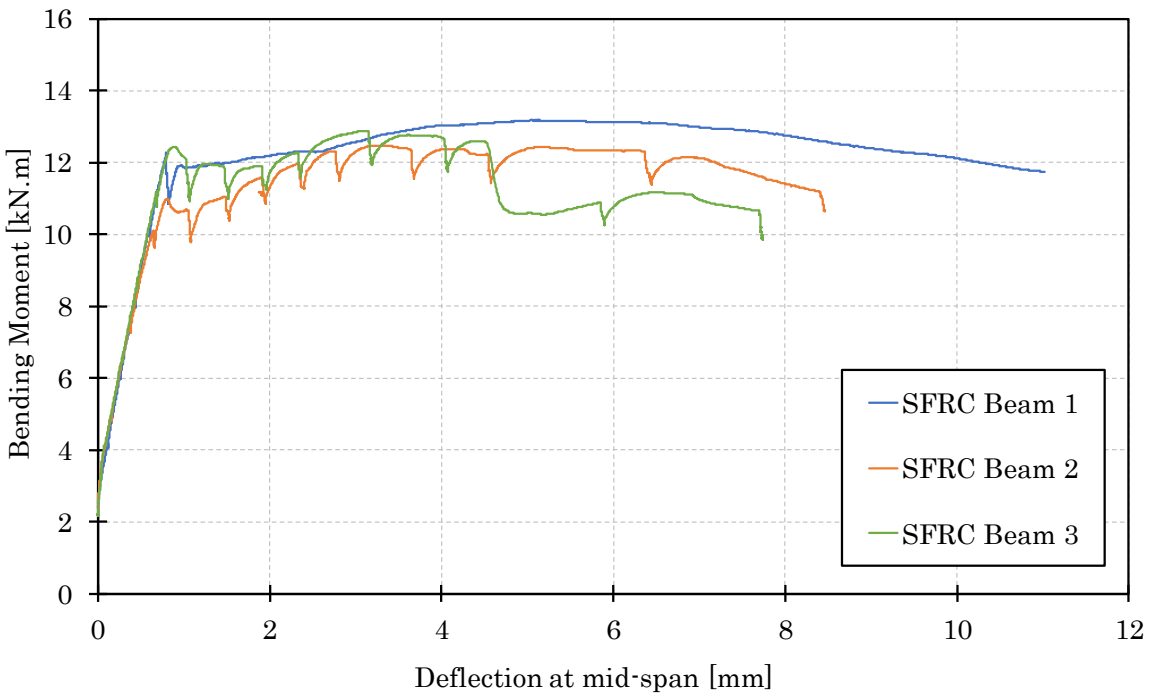

Figure 38: Bending moment-deflection curves for SFRC beams.

The comparison between the design values and resisted values are presented in Table 11. The bending moments obtained in the SFRC beam tests were considerably less than those designed with the *fib* Model Code (2010). The design values were on average 18.7% larger than the ones obtained in the test. This demonstrates that the SF60 notched beams were not a good representation of the tensile resistance of the SFRC beams. It is hypothesised that this could be due to the different areas of both beams. The notched beams had a width of 150mm, while the SFRC beams' width was 450mm. This could cause a dissimilar fibre distribution along each beam's width, resulting in different resistances. It may therefore be necessary to introduce a design factor that includes the effects of different beam cross-sections, in comparison to that of the standardised notched beams.

Table 11: Comparison of design and experimental bending moment values for SFRC beams.

Specimen	Density	$f_{cm,cube}$	Ultimate Bending Moment [kN.m]		
	[kg/m^3]	[MPa]	M_d	M_r	% Error
SFRC Beam 1	2419	50.5	15.80	13.17	-16.6%
SFRC Beam 2	2401	50.7	15.80	12.47	-21.1%
SFRC Beam 3	2400	48.8	15.77	12.87	-18.4%

5.6.2.2 Crack Formations

All the SFRC beams exhibited central crack formations, with one exception in SFRC Beam 3. The crack patterns are provided in Figure 39 and Figure 40.

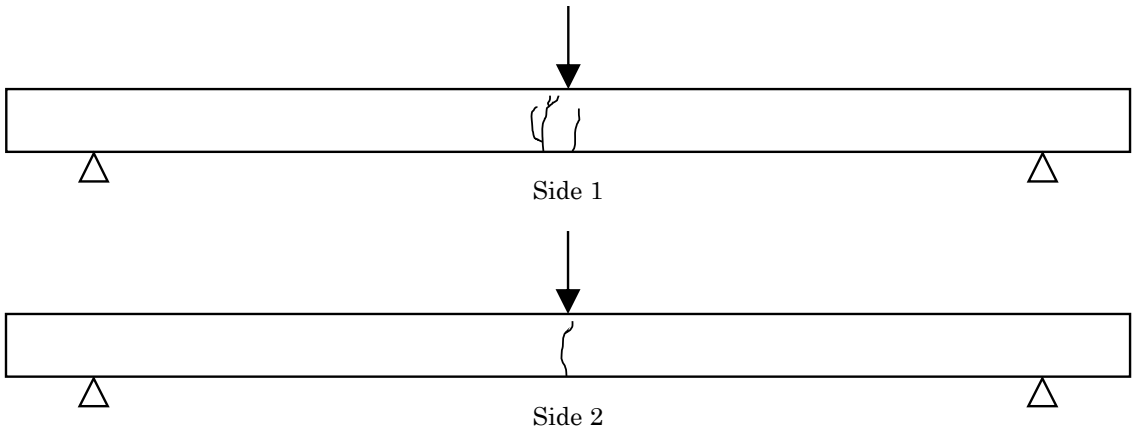

Figure 39: Crack patterns for SFRC Beam 2.

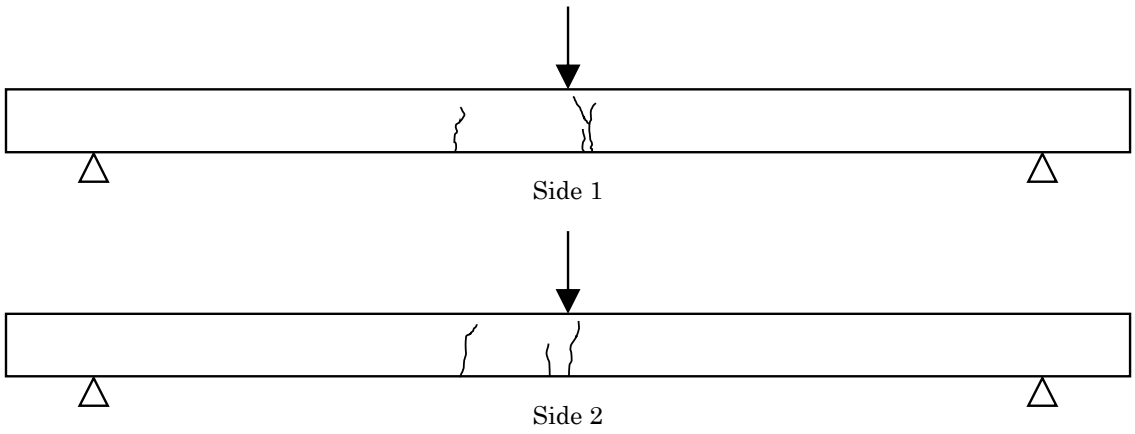

Figure 40: Crack patterns for SFRC Beam 3.

The measurement of the CMOD of SFRC Beams 2 and 3 was challenging due to the crack formations. The additional tensile face LVDT was added however, the positions at which the cracks formed were not ideal. A crack on SFRC Beam 2 formed next to the PVC clamp securing the additional LVDT. The test was therefore terminated prematurely in order to prevent the any damage to LVDT due to it detaching.

A crack on SFRC Beam 3 formed outside the measuring range of the tensile face LVDT after a mid-span displacement of 4.5mm. This crack can be seen on the left-hand side of

the central cracks in Figure 40. The cause of this crack is likely due to the behaviour of a concrete mix near its critical fibre dosage. Thus the fibres bridging the primary central crack provided enough resistance for a new crack to form. The SFRC Beam 3 test was terminated when the sum of LVDT CMOD and the additional crack width was 2.5mm. The bending moment-CMOD curves obtained are presented in Figure 41.

The SFRC's flexural response was far less ductile than that of the RC beams. SFRC Beam 2 obtained a maximum CMOD of a 1.86mm at a mid-span deflection of only 8.4mm. This is in comparison to the maximum crack width of 2.5mm obtained by the RC beams, at a mid-span deflection greater than 30mm.

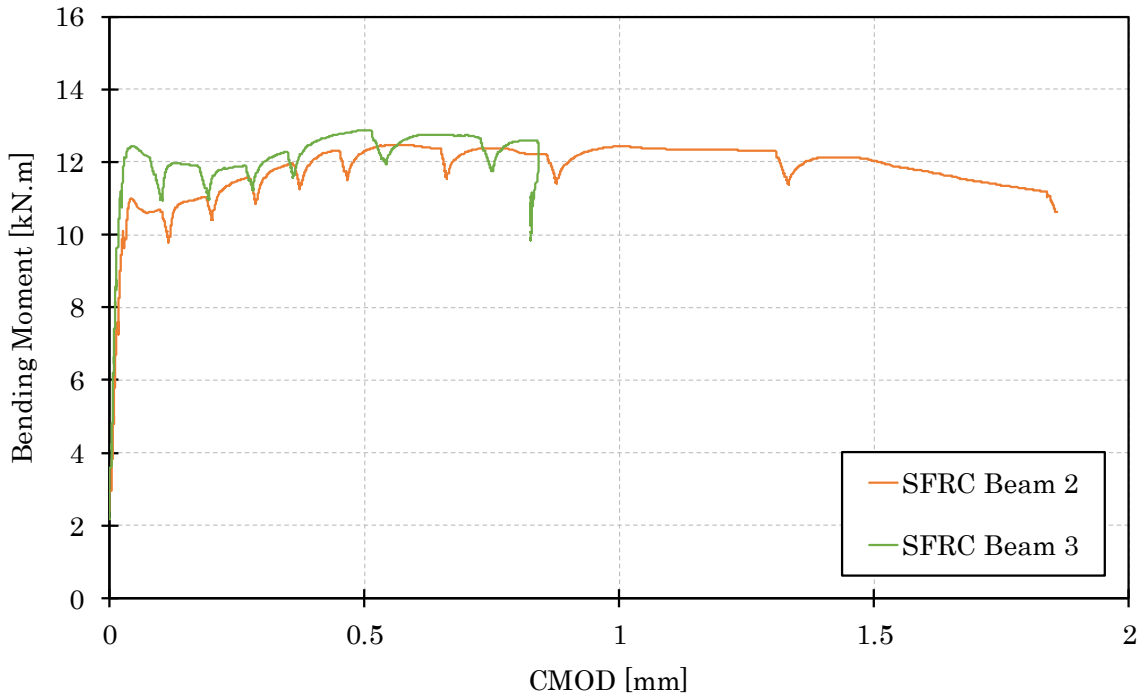

Figure 41: Bending moment-CMOD curves for SFRC beams.

5.6.3 Combined Beams

5.6.3.1 General Behaviour

The flexural response of the combined beams is presented in Figure 42. The combined beams demonstrated distinctive deflection softening behaviour.

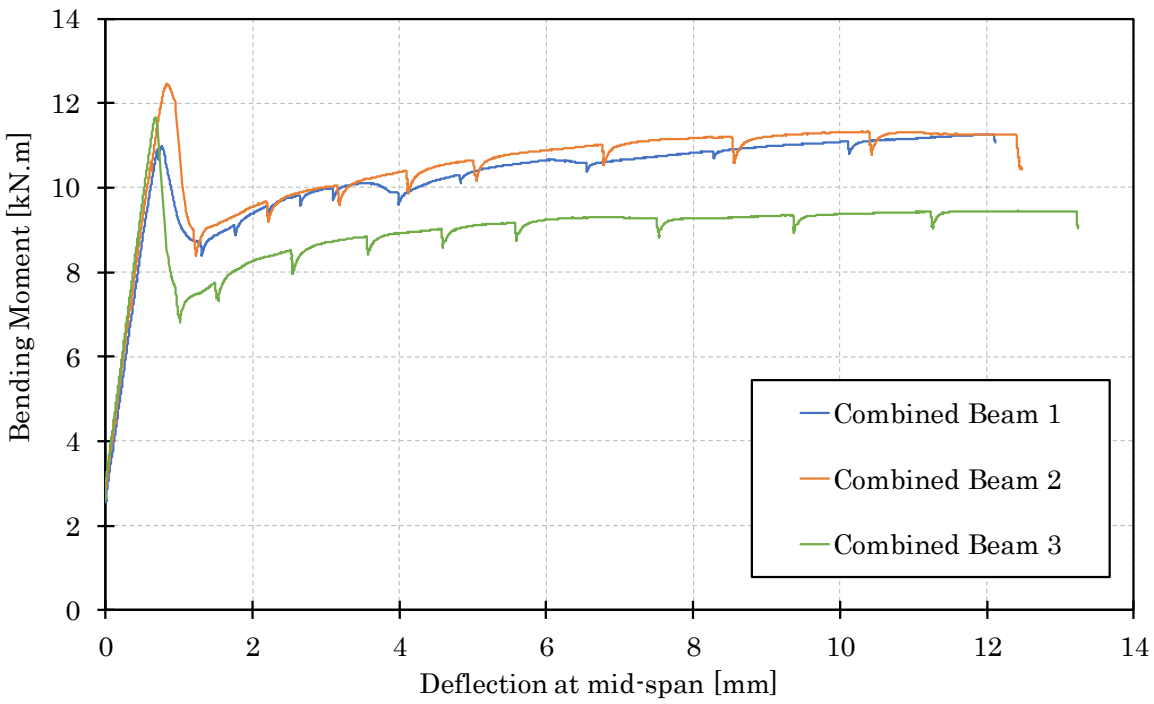

Figure 42: Bending moment-deflection curves for combined beams.

The evaluation of the combined beams' flexural strengths is provided in Table 12. The ultimate tensile stress of the reinforcing bar steel was used in the combined beams' flexural design. The average ultimate bending moment achieved by the combined beams was 25.2% less than its average design value. This error indicates that the SF30 notched beams were also not a good representation of the steel fibre reinforcing's tensile strength. This further illustrates the possible need for a factor to account for the different beam cross-sections, as presented in Section 5.6.2.1.

Table 12: Comparison of design and experimental bending moment values for combined beams.

Specimen	Density [kg/m^3]	$f_{cm,cube}$ [MPa]	Ultimate Bending Moment [kN.m]		
			M_d	M_r	% Error
Combined Beam 1	2324	45.3	15.77	11.27	-28.5%
Combined Beam 2	2352	44.4	15.75	12.45	-21.0%
Combined Beam 3	2326	45.8	15.77	11.66	-26.1%

5.6.3.2 Crack Formations

The combined beams displayed typical localised crack formation expected from a deflection softening material. The locations of the cracks can be seen in Figure 43 and Figure 44.

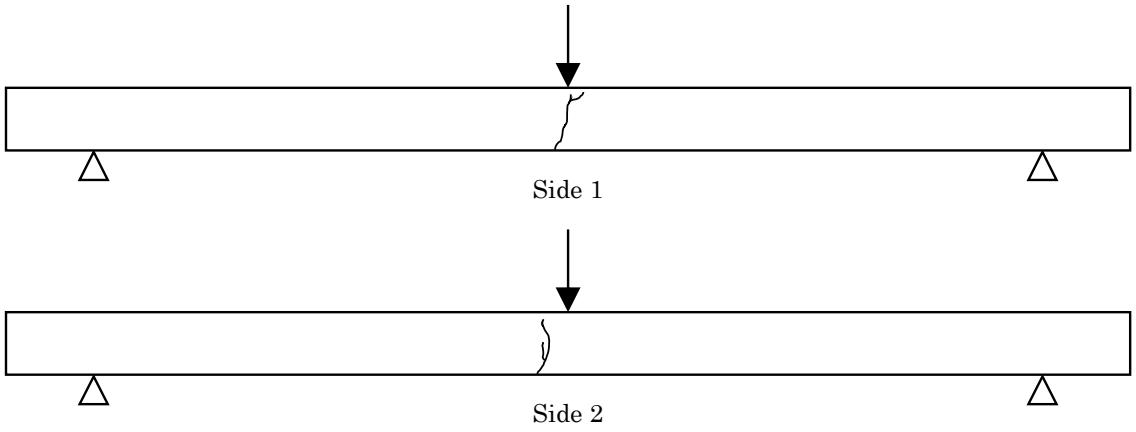

Figure 43: Crack pattern for Combined Beam 2.

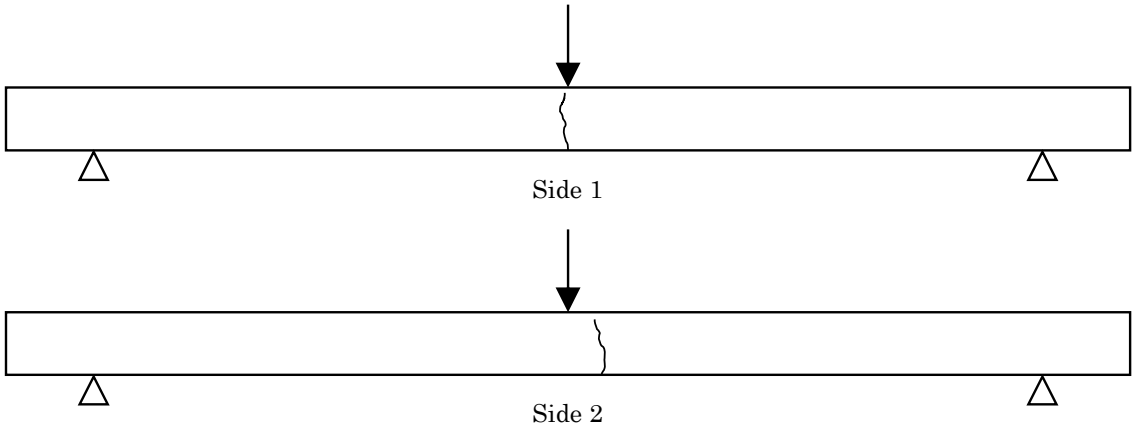

Figure 44: Crack pattern for Combined Beam 3.

The bending moment-CMOD curves obtained by Combined Beams 2 and 3 are presented in Figure 45. The ductility obtained by the combined beams was again much lower than that of the RC beams. This is mainly due to the reinforcing bar steel having no significant effect on the cracking pattern of the beam. The localised crack due to the steel fibres, resulted in the reinforcing bar steel only yielding at the crack position. The redistribution of internal stresses, as described in Figure 37, was therefore not possible. The

advantageous ductility of the reinforcing bar steel was therefore lost. Further research is necessary in order to optimise a combined reinforced concrete in which steel fibres and reinforcing bar steel work simultaneously.

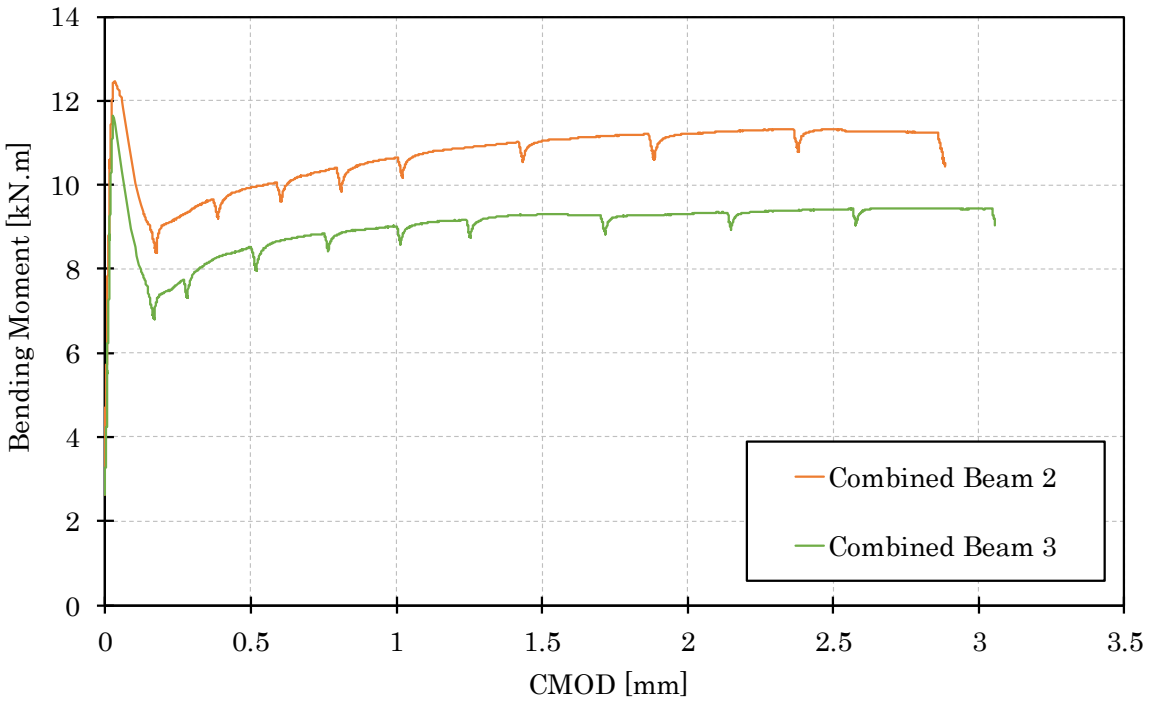

Figure 45: Bending moment-CMOD curves for combined beams.

5.6.4 Analysis for Cracked Reinforced Beam Creep Test

The deflection-CMOD curves for the combined and SFRC beams were examined in order to obtain a mid-span displacement that correlated to a CMOD of 0.5mm. The reason for this CMOD value is discussed in Section 3.3.1.3. The deflection-CMOD used are shown in Figure 46. A linear relationship was found to exist between the mid-span deflection and CMOD, of all the fibre beams, after a CMOD of approximately 0.03mm. Using the curves presented, it was decided to pre-crack all the reinforced beam creep test specimens to a mid-span deflection of 3mm. This would result in a CMOD of approximately 0.5mm in both the SFRC and combined beams.

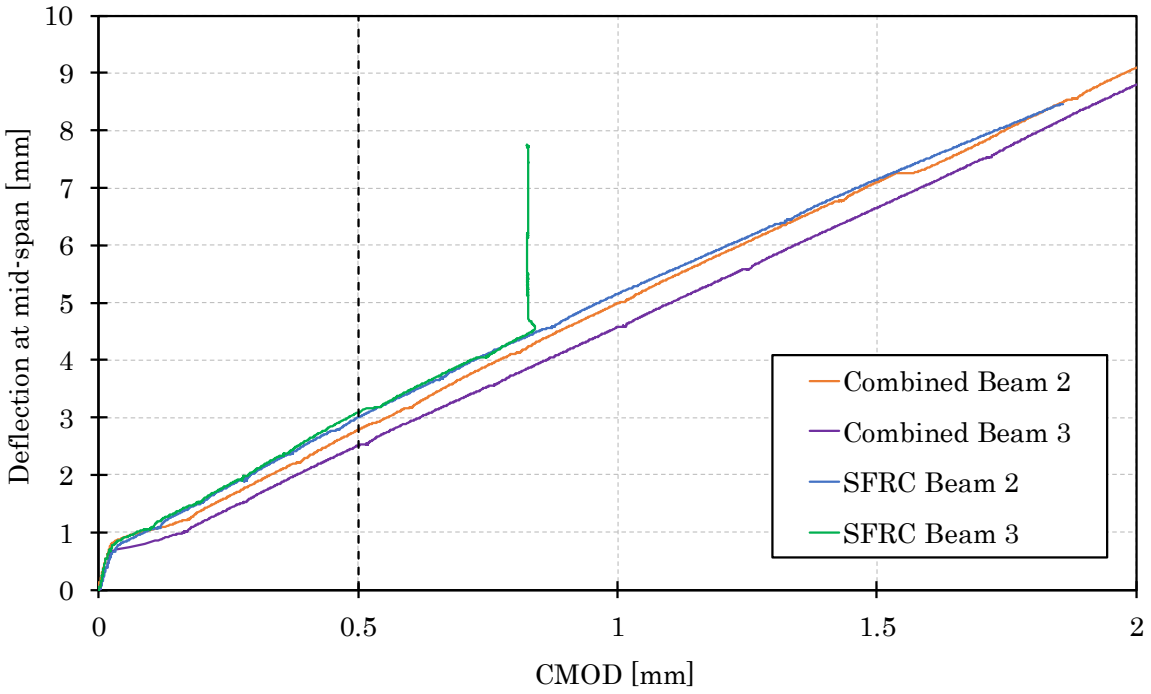

Figure 46: Deflection-CMOD curves for SFRC and combined beams.

5.7 Concluding Summary

In this chapter the compressive strengths, densities and elastic moduli of all three concrete mixes were presented. An increase in both the compressive strengths and densities was observed in the steel fibre concrete mixes. The steel fibres had no effect on the elastic modulus values obtained.

The tensile resistance of both the reinforcing bar steel and steel fibre mixes were calculated for the flexural design purposes. The steel fibre tensile design strength's obtained large CoV's, thought to be a consequence of the casting procedure used. This result indicates that an extra reliability factor may need to be added, in order to account for the casting procedure used in SFRC.

The flexural design method proposed in Chapter 4 was verified through the RC beam test results. The ultimate bending moment averages are presented in Table 13. The SFRC and combined beams obtained bending moments far smaller than the design values. This result demonstrated that the notched beams used to calculate the steel fibre reinforcing's tensile strength were not good representations of the reinforced beams. A method of relating the different beam cross-sections may be required.

Table 13: Average design and experimental bending moment values for reinforced beam tests.

Overall Averages	M_d [kN.m]	M_r [kN.m]	% Error
RC Beams	19.10	19.67	3.0%
SFRC Beams	15.79	11.90	-18.7%
Combined Beams	15.76	11.70	-25.2%

The combined and SFRC beams demonstrated far less ductile behaviour that the RC beams. This was particularly evident in the cracking patterns recorded for the beam specimens.

The required mid-span deflection to induce a 0.5mm in the SFRC beams was found to be 3mm. This value was used in the cracked reinforced beam creep tests presented in Chapter 6.

Chapter 6
Results and Discussion: Time-dependent Behaviour

6.1 Cracked Reinforced Beam Creep Test

In this section the bending moment-deflection curves due to pre-cracking are analysed and the sustained loading calculated. The creep of each beam over a period of 120 days is then discussed.

The flexural design of the RC beams used in the creep tests were revised in order to account for the increased tensile resistance of the reinforcing bar steel. The number of reinforcing bars cast in the RC beams was reduced in order to allow for all three types of beams to obtain similar flexural capacities. This would allow for a fair creep comparison between the reinforced beams. The flexural design values for the reinforced beam creep tests are provided in Table 14. The difference in flexural resistance, compared to that of the SFRC creep beams, is also presented.

Table 14: Flexural design values for the cracked reinforced beam creep tests.

Specimen	$f_{cm,cube}$ [MPa]	No. Bars	M_d [kN.m]	% Difference
SFRC Beam	51.0	0	15.80	
RC Beam	42.6	5	13.76	-12.9%
Combined Beam	45.9	2	15.78	-0.1%

6.1.1 Pre-cracking Phase

The flexural responses of the SFRC creep beams are presented in Figure 47, along with the responses of the previous SFRC beams. The bending moment comparison is shown in Table 15. The SFRC creep beams achieved higher flexural resistances than the SFRC

beams in Section 5.6.2.1. This suggests that the SFRC creep beams' fibre distributions were closer to that of the SF60 notched beams, with the average error of only 6.4%.

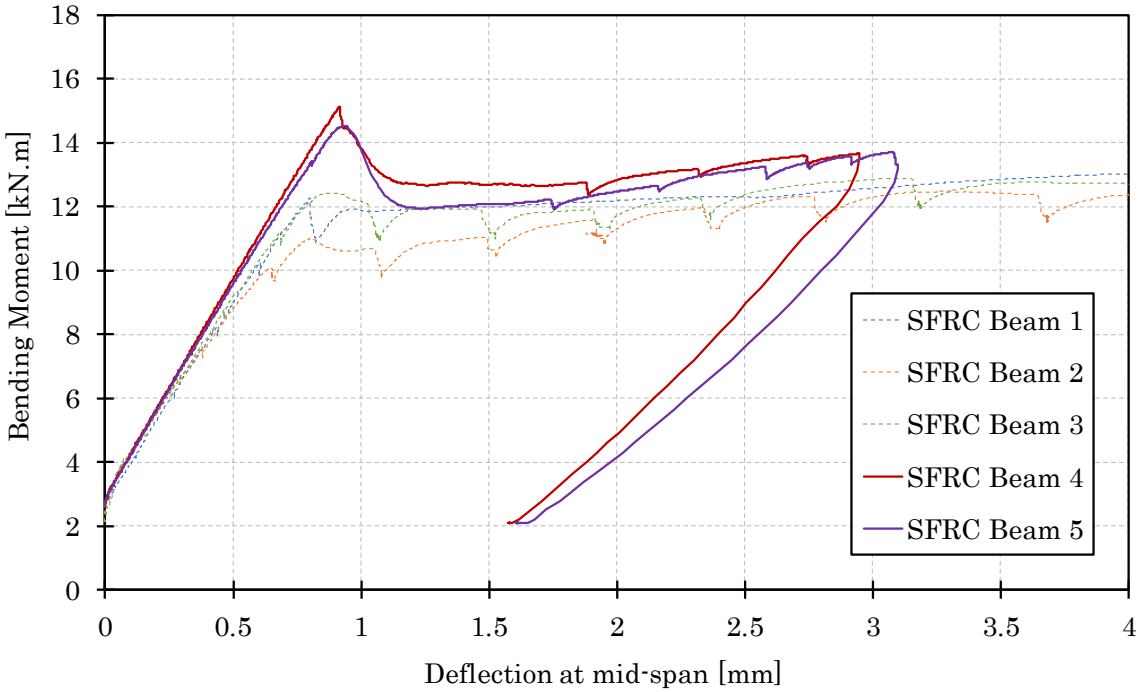

Figure 47: Bending moment-deflection curves for SFRC creep beams.

Table 15: Comparison of design and experimental bending moment values for SFRC creep beams.

Specimen	Density [kg/m³]	$f_{cm,cube}$ [MPa]	Ultimate Bending Moment [kN.m]		
			M_d	M_r	% Error
SFRC Beam 4	2382	51.5	15.81	15.12	-4.4%
SFRC Beam 5	2392	54.2	15.85	14.54	-8.3%

The bending moment-deflection curves of the combined creep beams are displayed in Figure 48, along with the bending moment values presented in Table 16. Combined Beam 4 also showed a marked improvement in flexural response, achieving an error of only 12.5%. Combined Beam 5 however obtained a similar error to those obtained in to Section 5.6.3.1.

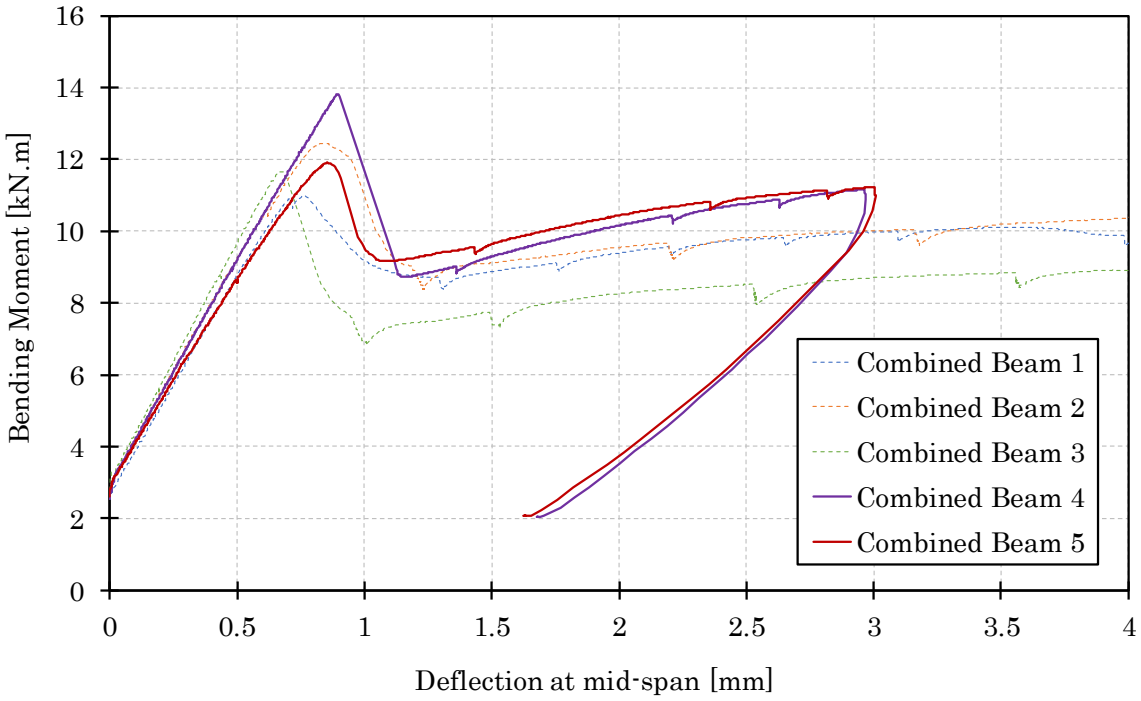

Figure 48: Bending moment-deflection curves for combined creep beams.

Table 16: Comparison of design and experimental bending moment values for combined creep beams.

Specimen	Density [kg/m³]	$f_{cm,cube}$ [MPa]	Ultimate Bending Moment [kN.m]		
			M_d	M_r	% Error
Combined Beam 4	2283	46.7	15.79	13.82	-12.5%
Combined Beam 5	2336	49.2	15.82	11.90	-24.8%

The flexural response of the RC creep beams is presented in Figure 49. The previous results of the RC beams containing seven reinforcing bars were also plotted. The cracking value of the RC beams remained the same. Both RC creep beams cracked in two locations. This can be observed in the sudden decreases in flexural resistance, due to the redistribution of internal forces. The maximum bending moment achieved by each RC creep beam can be seen in Table 17. It can be seen that after applying a mid-span deflection of 3mm to RC Beams 4 and 5, the beams had obtained 87.8% and 81.9% of their design bending moments, respectively. Although both RC creep beams had not reached their ultimate bending moments, the maximum experimental bending moments obtained were still used to calculate the sustained loading of each beam.

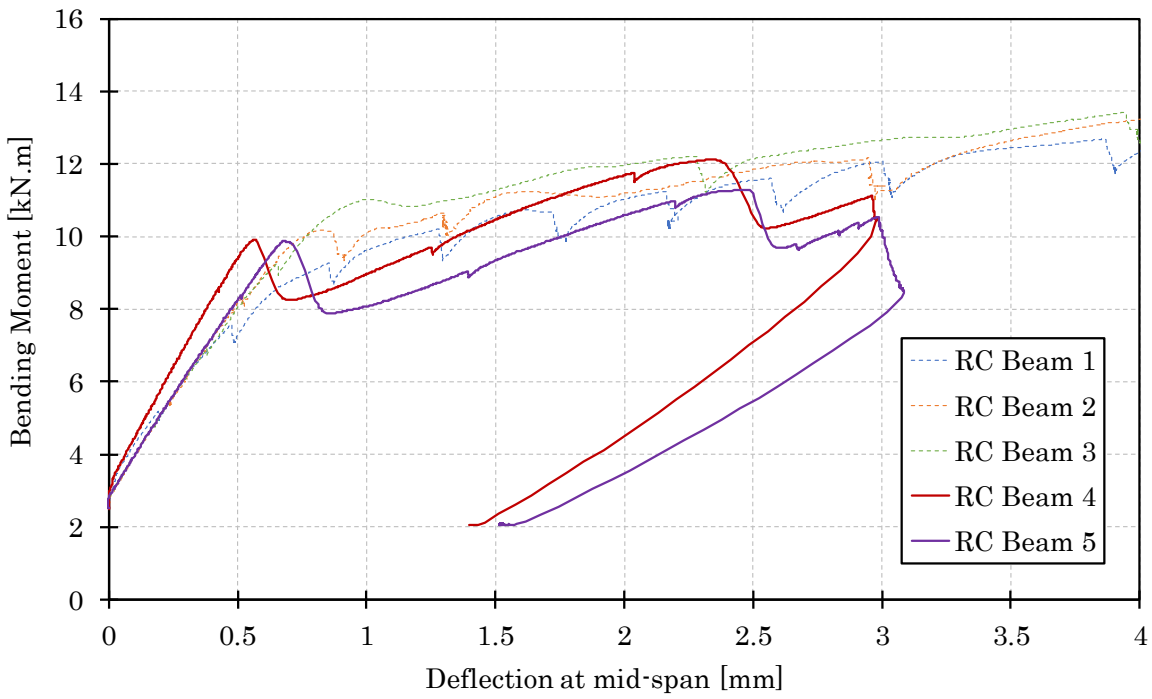

Figure 49: Bending moment-deflection curves for RC creep beams.

Table 17: Comparison of design and experimental bending moment values for RC creep beams.

Specimen	Density [kg/m³]	$f_{cm,cube}$ [MPa]	Ultimate Bending Moment [kN.m]		
			M_d	M_r	% M_d Obtained
RC Beam 4	2304	48.0	13.79	12.11	87.8%
RC Beam 5	2336	49.6	13.79	11.30	81.9%

Both the SFRC and combined creep beams displayed deflection softening behaviour, resulting in one localised central crack. The bending moment-CMOD curve of each beam was therefore again obtainable. Figure 50 presents the curves obtained for both SFRC and combined creep beams. Both fibre reinforced beam types obtained CMODs of approximately 0.5mm, as required in the cracked reinforced beam creep test. This result implied that fibre bridging mechanisms were now dominant in bridging the central crack of each beam. The consequence of this would be that the majority of creep experienced by the fibre reinforced beams would be due to fibre pull-out behaviour.

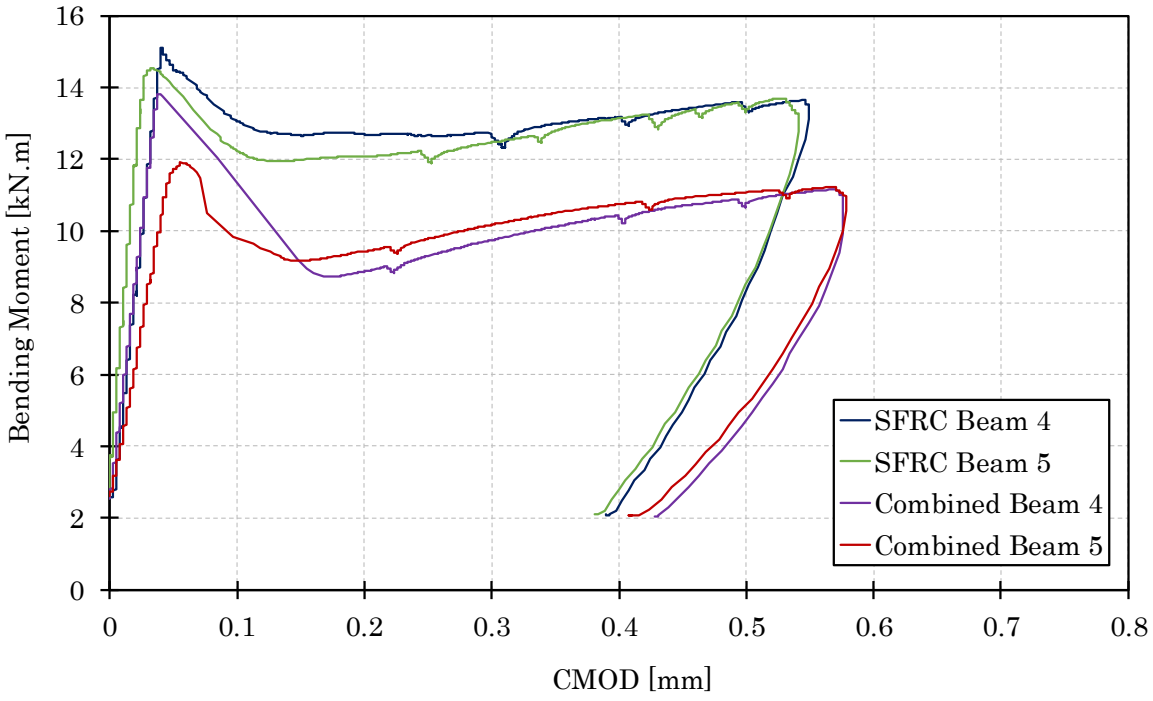

Figure 50: Bending moment-CMOD curves for SFRC and combined creep beams.

Once pre-cracking was completed, the sustained flexural loading was calculated. The applied bending moments *(M_{app})* were used in calculating the sustained loading *(M_{sus})* required for each beam. The self-weight loading of each beam was subtracted in order to calculate the applied bending moments *(M_{app})*. A sustained load level of 40% of the maximum applied load was used. Two tested notched beams, used in Section 5.5, along with a wooden box carrying sand and lead weights, were used in applying each load. The total weight required *(W_{sus})* to load each beam to 40% of its maximum flexural load, was calculated and is presented in Table 18.

Table 18: Sustained loading values used for the cracked reinforced beam creep tests.

Specimen	M_{app} [kN.m]	M_{sus} [kN.m]	W_{sus} [kg]
SFRC Beam 4	13.67	5.47	1013
SFRC Beam 5	13.09	5.24	970
Combined Beam 4	12.45	4.98	923
Combined Beam 5	10.50	4.20	778
RC Beam 4	10.73	4.29	795
RC Beam 5	9.89	3.96	733

The permanent (δ_p) and elastic ($\delta_{e,s}$) deflections due to the pre-cracking and sustained loading, respectively, are shown in Table 19. The maximum deflection (δ_{max}) obtained by each creep beam is also presented. The results show that the SFRC achieved larger permanent deformations than the RC. This is likely to be caused by the pull-out of fibres bridging the crack, during loading. Frictional resistance exists between the concrete matrix and steel fibres when the beam is unloaded. This results in the fibres providing an opposite resisting force, thus increasing the unloading stiffness. It is also this stiffness that also allows the SFRC beams to achieve smaller reloading deflections ($\delta_{e,s}$).

Table 19: Reinforced creep beam deflections due to pre-cracking and initial sustained loading.

Specimen	δ_{max} [mm]	δ_p [mm]	$\delta_{e,s}$ [mm]
SFRC Beam 4	2.95	1.58	0.77
SFRC Beam 5	3.10	1.61	0.77
Combined Beam 4	2.97	1.68	0.97
Combined Beam 5	3.01	1.63	0.89
RC Beam 4	2.98	1.40	0.88
RC Beam 5	3.08	1.52	1.03

6.1.2 Creep Behaviour of Cracked Reinforced Beams

The creep curves of all three beam types are presented in normal and logarithmic time scales in Figure 51 and Figure 52, respectively. The primary creep phase of the RC beams lasted approximately 13 days, 21 days for the combined beams, and 26 days for the SFRC beams. This was then followed by a secondary creep response in all the beams, with no beams experiencing any tertiary creep. A small variance in creep response was obtained for the SFRC and RC beams, with the combined beams obtaining the largest difference with an average CoV of 10%. Both the SFRC and combined beams showed creep deflections larger than that of the RC beams. This was expected due to the additional fibre pull-out creep experience by the fibres. The RC beams obtained an average creep deformation of 2.43mm after 4 months of sustained flexural loading. This was in comparison to the 3.07mm average obtained by the SFRC beams, 26% larger than the RC beams. The combined beams obtained an average of 3.36mm, showing that marginally more deflection was occurring due to the lower fibre volume. This deflection was 38% larger than the RC beams, and 9% larger than the SFRC beams.

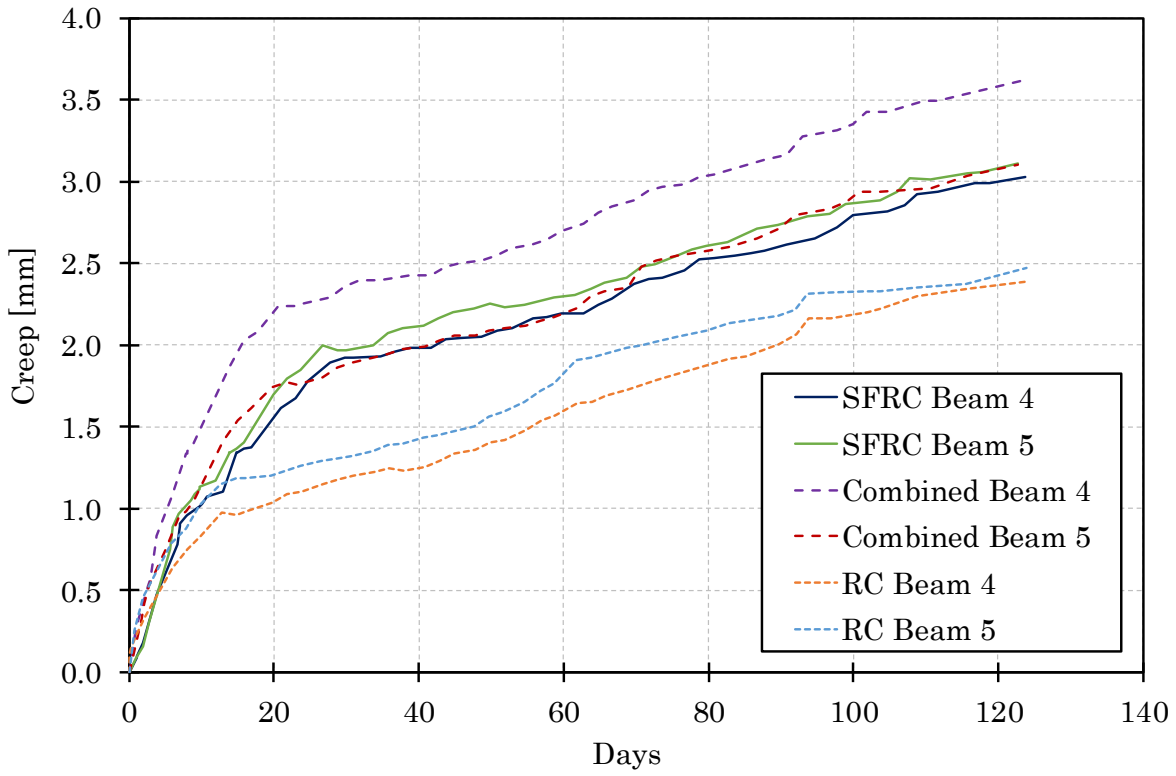

Figure 51: Creep curves for cracked reinforced beams.

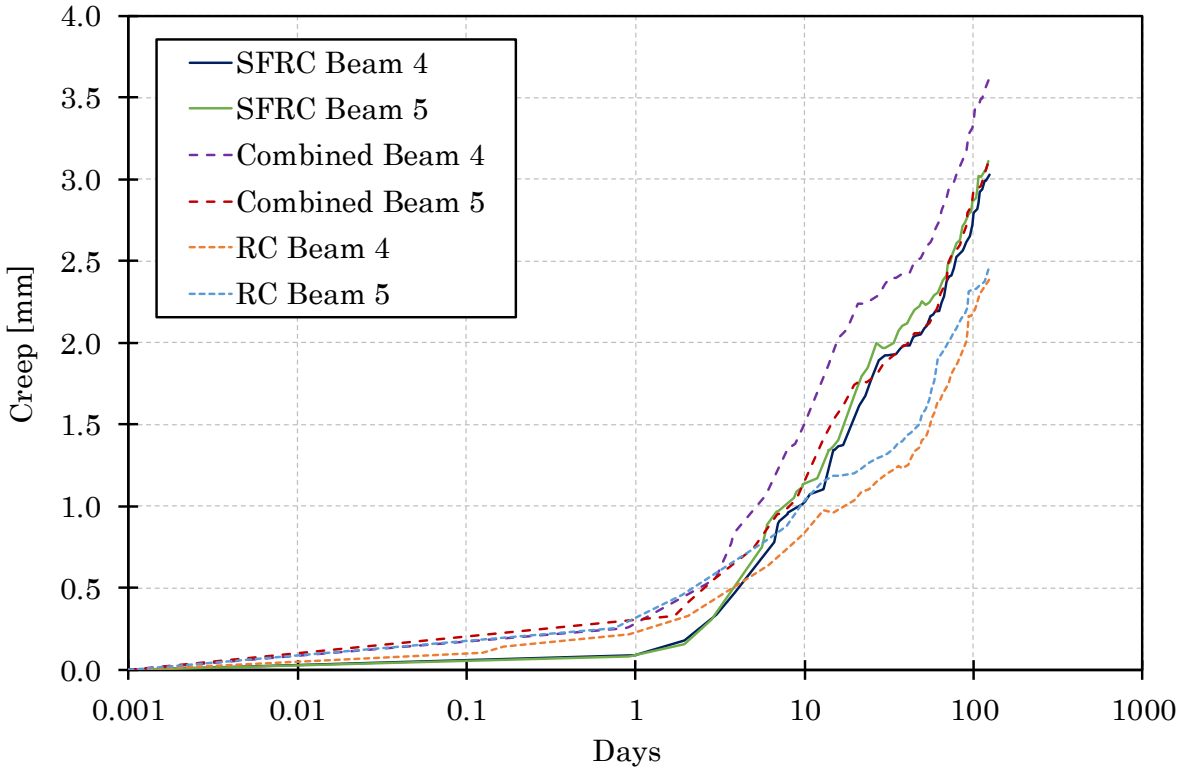

Figure 52: Logarithmic creep curves for cracked reinforced beams.

6.2 Drying Shrinkage

The average drying shrinkage strains obtained for the SF30 and SF60 mixes are presented in Figure 53(a). The shrinkage values were compared to those obtained by Nieuwoudt (2016) in a similar test, shown in Figure 53(b). It can be seen that the shrinkage values obtained were far larger than those obtained by Nieuwoudt (2016). The shrinkage strains recorded were also uncharacteristically large for drying shrinkage strains at a concrete age of greater than 77 days. The reason for these unusual strains is thought to be due to a malfunction in digital dial gauge. The shrinkage strains obtained were therefore disregarded, and the *fib* Model Code (2010) was used to calculate the theoretical drying shrinkage strains needed. Research by Nieuwoudt (2016), as seen in Figure 53(b), has shown the accuracy of the *fib's* drying shrinkage model.

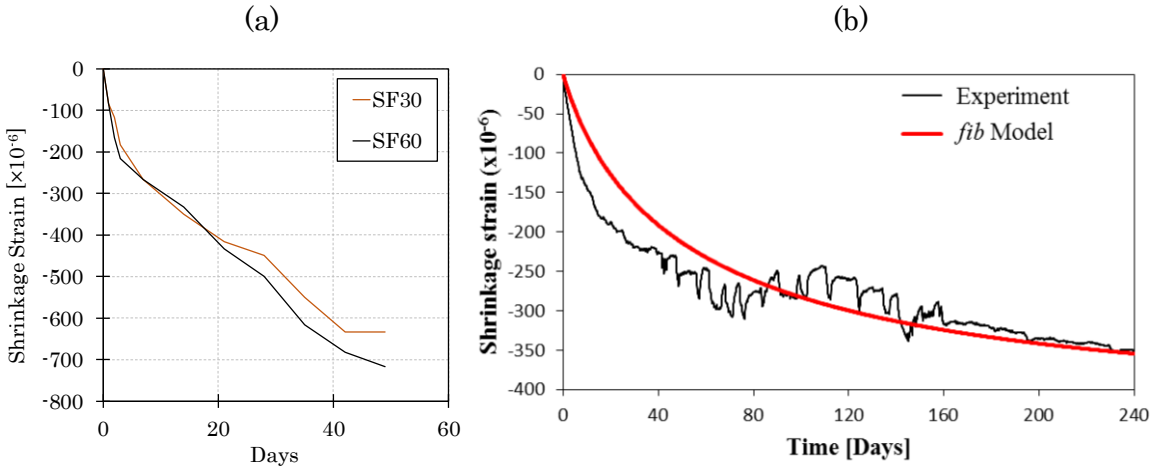

Figure 53: (a) Drying shrinkage results, (b) drying shrinkage results (Nieuwoudt, 2016).

The *fib* defines the drying shrinkage strain of concrete as:

$$\varepsilon_{cds}(t, t_s) = \varepsilon_{cds0}(f_{cm}) \cdot \beta_{RH}(RH) \cdot \beta_{ds}(t - t_s) \tag{6-1}$$

with

$$\varepsilon_{cds0}(f_{cm}) = \left(880 \cdot exp(-0.012 \cdot f_{cm})\right) \cdot 10^{-6} \tag{6-2}$$

$$\beta_{RH} = -1.55 \cdot \left(1 - \left(\frac{RH}{100}\right)^3\right) \cdot \left(\frac{35}{f_{cm}}\right)^{0.1} \tag{6-3}$$

$$\beta_{ds}(t - t_s) = \left(\frac{(t - t_s)}{0.035 \cdot {h_c}^2 + (t - t_s)}\right)^{0.5} \tag{6-4}$$

where: $\varepsilon_{cds}(t,t_s)$ is the drying shrinkage strain, t is the concrete age, t_s is the concrete age at the beginning of drying, f_{cm} is the mean compressive cylinder stress at an age of 28 days, RH is the relative humidity of the ambient environment, the nominal size of the member $h_c = 2A_c/u$, where A_c is the concrete's cross-sectional area and u is the exposed perimeter in contact with the environment.

The drying shrinkage strain was calculated from the first day of curing. The compressive strengths obtained in Section 5.1 were used for the respective fibre mixes. The cross section and exposed perimeter of the uniaxial tensile creep specimens, i.e. 100×100mm with all sides exposed, was used in calculating h_c. The resulting drying shrinkage strain curves can be seen in Figure 54(a). Testing on the uniaxial tensile creep specimens was initiated at a concrete age of 77 days and therefore the shrinkage strains from 77 days onwards were used in obtaining the actual CMODs of the uniaxial tensile creep specimens. These drying shrinkage strains are presented in Figure 54(b) for both mixes.

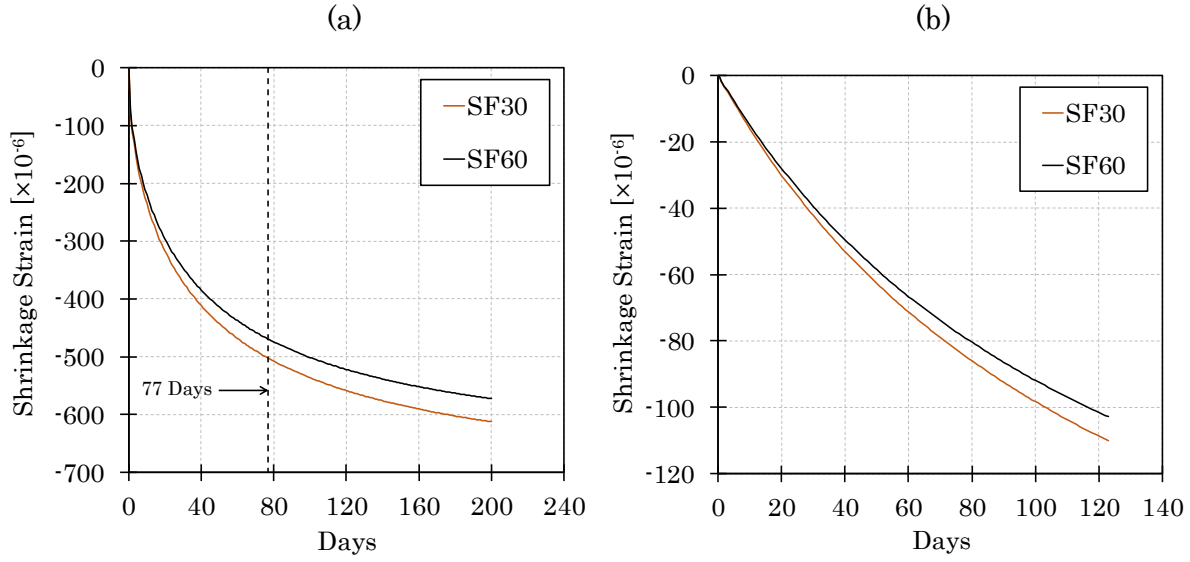

Figure 54: (a) *fib* Model drying shrinkage results for SF30 and SF60 mixes, (b) *fib* model drying shrinkage strains used in uniaxial tensile creep tests.

6.3 Uniaxial Tensile Creep Test

The stress-CMOD obtained by the pre-cracking of the uniaxial creep specimens can be seen in Figure 55. It can be seen that the both SF30 specimens and SF60 Specimen 1 were successfully cracked close to an average CMOD of 0.2mm. The energy build up in SF60 Specimen 2, as discussed in Section 3.3.3.3, caused an instantaneous CMOD of 0.248mm.

This value was still acceptable for the purpose of this research. All four uniaxial creep specimens displayed tension softening behaviour. The maximum and permanent CMODs due to pre-cracking are shown in Table 20.

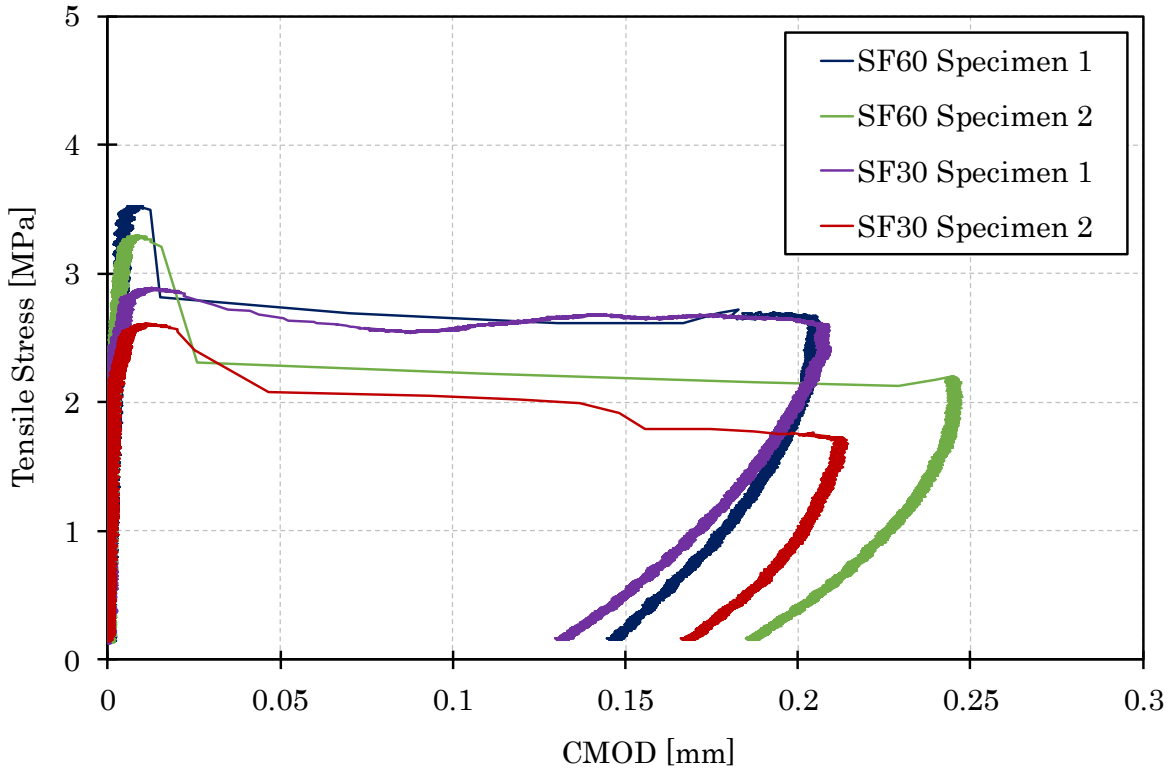

Figure 55: Tensile stress-CMOD curve for pre-cracked uniaxial creep specimens.

Table 20: Maximum tensile stress and deflections due to pre-cracking.

Specimen	σ_{max} [MPa]	$CMOD_{max}$ [mm]	$CMOD_p$ [mm]
SF60 Specimen 1	3.52	0.207	0.146
SF60 Specimen 2	3.29	0.248	0.188
SF30 Specimen 1	2.89	0.210	0.133
SF30 Specimen 2	2.61	0.215	0.168

The long-term loads were calculated using the maximum tensile stress obtained for each specimen, presented in Table 20. The calculated sustained stresses applied to each uniaxial tensile creep specimen is shown in Table 21. The average instantaneous elastic CMOD measured due to the loading is also displayed.

Table 21: Sustained tensile stresses and elastic deflections due to the loading.

Specimen	σ_{sus} [MPa]	$CMOD_{e,s}$ [mm]
SF60 Specimen 1	1.41	0.038
SF60 Specimen 2	1.32	0.034
SF30 Specimen 1	1.16	0.032
SF30 Specimen 2	1.04	0.036

The CMODs due to the sustained loadings for the SF60 mix can be seen in Figure 56(a) and (b). The four LVDT CMOD curves are plotted along with the average for each specimen. The two SF60 uniaxial tensile creep specimens obtained varied CMOD responses. SF60 Specimen 1 displayed far greater resistance to the loading than SF60 Specimen 2. This is likely due to a greater fibre concentration present bridging the crack in Specimen 1. The average CMOD of Specimen 1 had increased by 22% at 120 days, in comparison to the instantaneous elastic CMOD. Specimen 2 had increased by 101%. The average CMOD curve of the SF60 mix, due to fibre pull-out creep, is presented in Figure 57. Both specimens exhibit behaviour suggesting that they are near their asymptotic creep values, associated with SFRC.

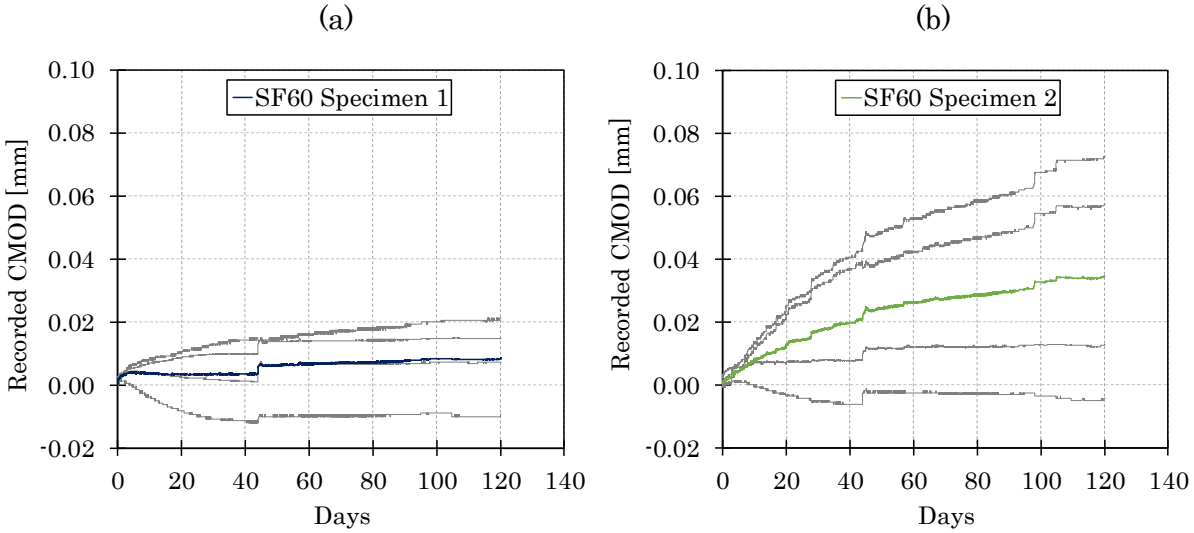

Figure 56: (a) LVDT readings for SF60 Specimen 1, (b) LVDT readings for SF60 Specimen 2.

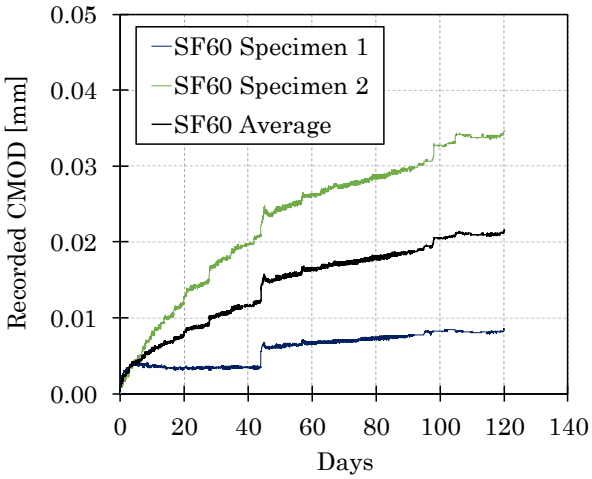

Figure 57: Average recorded CMOD curve for SF60 mix.

The average CMODs, along with each LVDT's CMODs, are presented in Figure 58(a) for SF30 Specimen 2. A large jump in the all the LVDT readings is shown 14 days after the test commenced. It is thought that this jump was as a result of a knock to the frame. This jump was therefore removed as it was not a true reflection of the rate of CMOD. The corrected CMOD response for SF30 Specimen 2 is provided in Figure 58(b). The average CMOD of SF30 Specimen 2 had increased by 54% after 4 months of testing, in comparison to the instantaneous elastic CMOD obtained. SF30 Specimen 2 displayed a typical SFRC creep response and was exhibiting characteristics of secondary creep. The specimen was therefore near its asymptotic creep value.

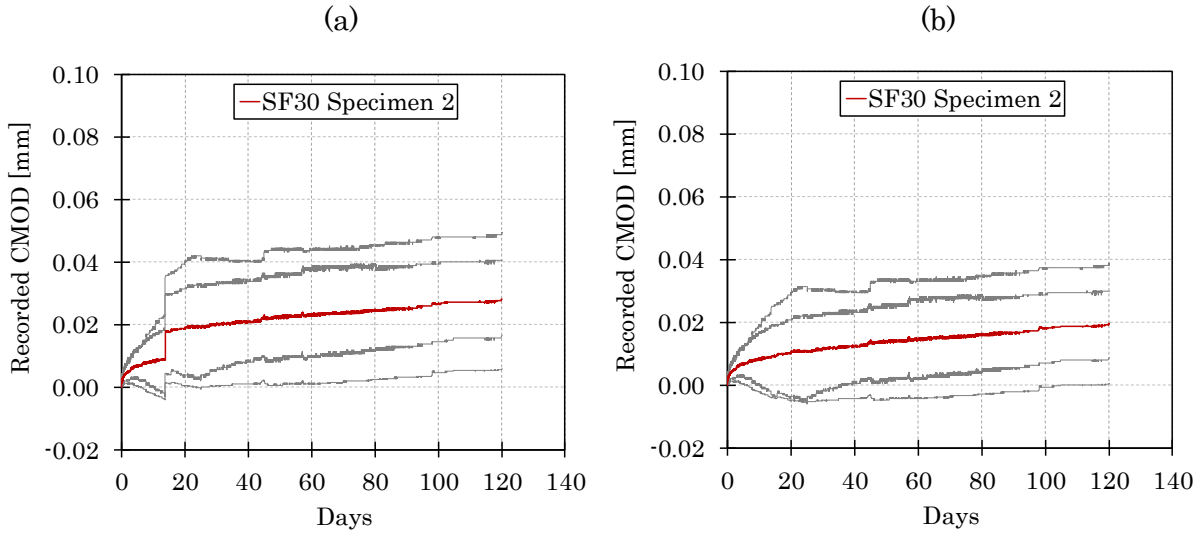

Figure 58: (a) LVDT readings for SF30 Specimen 2, (b) corrected LVDT readings for SF30 Specimen 2.

The CMODs due to the sustained loadings for SF30 Specimen 1 can be seen in Figure 59(a). The average CMOD of SF30 Specimen 1 had increased by 116% at 120 days, in comparison to the instantaneous elastic CMOD obtained. It can also be seen that the specimen had not decreased in the rate of CMOD, implying that the asymptotic CMOD creep value had not yet been reached. Figure 59(b) displays the overall average creep response of the SF30 mix. The SF30 mix obtained far less variable results than the SF60 mix. This behaviour can be seen when obtaining the average CMOD for each mix in Figure 57 and Figure 59(b).

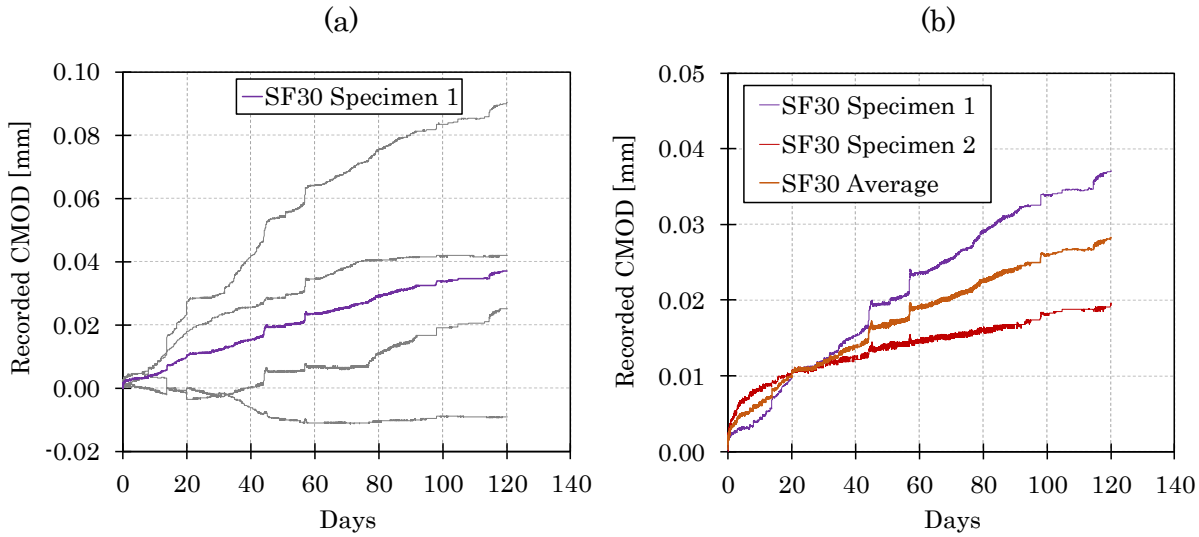

Figure 59: (a) LVDT readings for SF30 Specimen 1 (b) average recorded CMOD curve for SF30 mix.

The average CMODs, with drying shrinkage added, for each fibre mix are presented on both a normal and logarithmic time scale in Figure 60. The creep response of the SF60 mix suggests it is closer to reaching its asymptotic creep value, than the SF30 mix. It can be seen that the mix with a higher fibre dosage obtained a marginally smaller CMOD creep response. The average CMOD, obtained after 4 months, in comparison to the average instantaneous elastic CMOD was 80% and 105% for the SF60 and SF30 mixes respectively. It can therefore be deduced that the extra 30kg/m^3 of fibres present in the SF60 mix resulted in a 25% reduction in fibre pull-out creep.

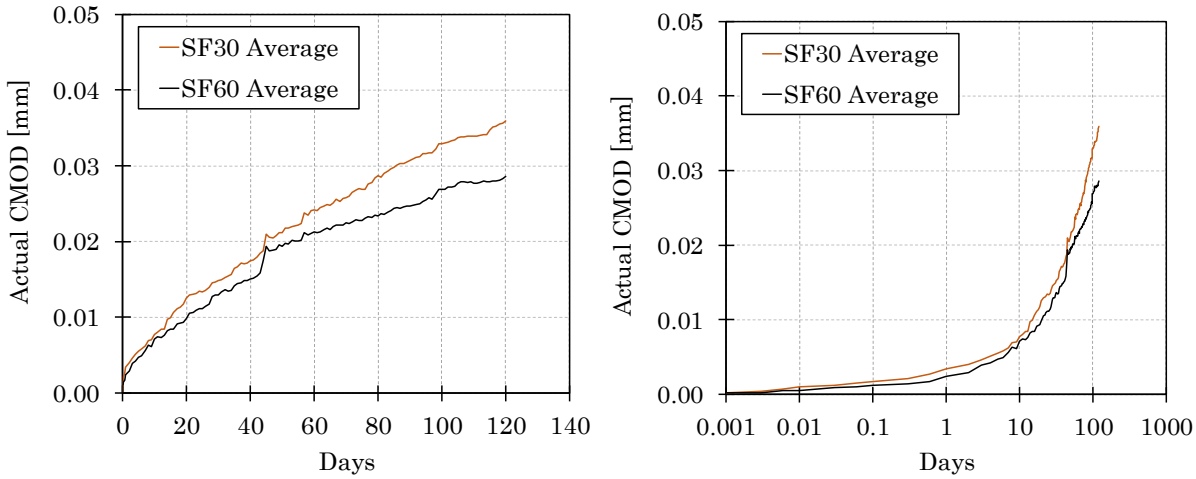

Figure 60: Actual CMOD curves for SF30 and SF60 mixes with drying shrinkage added.

6.4 Concluding Summary

In this chapter the time-dependent results of cracked SFRC were presented. Each reinforced creep beam was pre-cracked to a mid-span displacement of 3mm. This ensured that fibre bridging mechanisms were now dominant in bridging the SFRC's cracks. The creep deformation curve for each reinforced beam was presented. It was found that the SFRC beams deflected 26% more than the RC beams due to the additional fibre pull-out creep after 120 days. The combined beams deflected 38% more after 120 days of sustained flexural loading.

The drying shrinkage values obtained in this study were too high and thus unrealistic. This is thought to be due to the digital dial gauge malfunctioning. The *fib's* drying shrinkage model was therefore used to obtain the shrinkage strains necessary for the uniaxial creep tests.

The uniaxial tensile creep tests suggested that a reduction in fibre pull out creep is obtained at a higher fibre dosage. The time-dependent CMOD rate of both steel fibre mixes decreased with time, but neither displayed an asymptotic creep value. The creep responses obtained for each mix allowed for the prediction of the CMOD rates, to be used in Chapter 7.

Chapter 7

Time-dependent Modelling of Cracked SFRC in Flexure

7.1 Cracked Reinforced Beam Models

7.1.1 Damage Model

A damage model was created to calculate the elastic modulus damage factors as a result of pre-cracking the reinforced beams. The Bernoulli–Euler beam theory was used in developing the model. The equations used to obtain the various relationships over the length of a beam, $0 \leq x \leq L$, are:

$$V(x) = \int w(x)dx \tag{7-1}$$

$$M(x) = \int V(x)dx \tag{7-2}$$

$$\theta(x) = \int \frac{M(x)dx}{EI} \tag{7-3}$$

$$\delta(x) = \int \int \frac{M(x)dx^2}{EI} \tag{7-4}$$

where: $w(x)$ is the function of the applied distributed load, $V(x)$ is the function of the shear loading, $M(x)$ is the function of the bending moment, $\theta(x)$ represents the beam's rotation, $\delta(x)$ is the elastic curve of the beam, I is the moment of inertia of the cross-section with respect to y, and E is the material's modulus of elasticity.

The beam model used to represent the cracked reinforced beams is presented in Figure 61. Two different elastic moduli were assumed to exist after applying a central point load (F) to each beam, namely: the concrete's uncracked elastic modulus (E), and a cracked concrete elastic modulus (E_c). The length of the cracked elastic modulus section

was accepted to exist 250mm either side of the beam's mid-span. This assumption was based on the crack patterns observed in the reinforced beam tests, see Section 5.6. The self-weight of the beam *(w)* is also included in Figure 61.

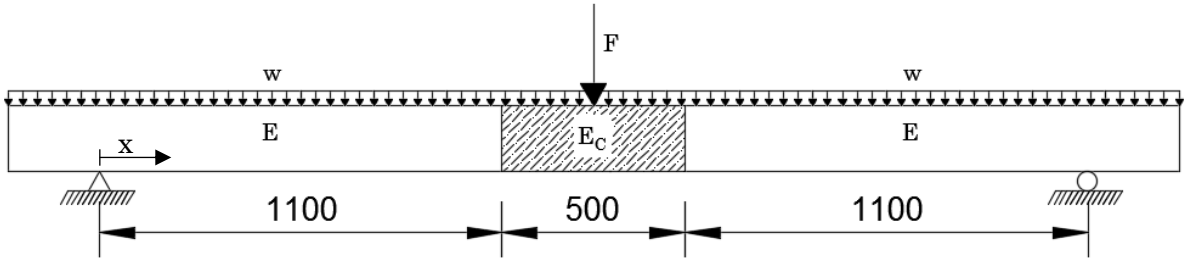

Figure 61: Beam model proposed to include the effect of pre-cracking.

The beam model was divided into two sections in order to apply Equations (7-1) to (7-4). Section one was assumed to extend from $0 \leq x \leq 1100mm$ and section two from $1100mm \leq x \leq 1350mm$, due to the beam's symmetry. Boundary and continuity conditions were used to obtain each section's elastic curve. The elastic curve for section one of the beam was calculated as:

$$\delta_1(x) = \frac{-\frac{wx^4}{24} + \frac{9wx^3}{40} + \frac{Fx^3}{12} + \left(-\frac{1081wx}{4800} - \frac{49Fx}{320}\right)\frac{E}{E_C} - \frac{7139wx}{12000} - \frac{121Fx}{400}}{EI} \tag{7-5}$$

The elastic curve obtained for section two is:

$$\delta_2(x) = \frac{-\frac{wx^4}{24} + \frac{9wx^3}{40} + \frac{Fx^3}{12} - \frac{6561wx}{8000} - \frac{729Fx}{1600}}{E_C I} + \frac{\left(-\frac{1331w}{3200} - \frac{11891wE}{48000E_C} - \frac{1331F}{6000} - \frac{539FE}{3200E_C}\right)\frac{E_C}{E} + \frac{1991w}{3000} + \frac{7805F}{20000}}{E_C I} \tag{7-6}$$

where: $\delta_i(x)$ is the vertical displacement of a beam section at a position x, w is the self-weight of the reinforced beam, F is the applied central load, E is the concrete's elastic modulus, E_c is the concrete's cracked elastic modulus, and I is the moment of inertia of the cross section with respect to y. A post-calculation check was performed to confirm the vertical displacement, at a value of $x = 1100mm$, was equal for both Equations (7-5) and (7-6).

The damage model was implemented by reducing the cracked elastic modulus of each beam type until a mid-span displacement of 3mm was obtained, using Equation (7-6). The force *(F)* used in this equation was the average applied pre-cracking force obtained at the 3mm mid-span displacement *($F_{app,\delta=3mm}$)* in Section 6.1.1. The average applied force *(F)*, used in Equation (7-6), is provided in Table 22. The self-weight loading *(w)* for each beam type was calculated using the average density obtained by the creep beam control cubes.

Table 22: Applied loadings used in each beam type's damage model.

	Pre-cracking Test Results		Damage Model Parameters	
	$M_{app,\delta=3mm}$ [kN.m]	$F_{app,\delta=3mm}$ [kN]	F [kN]	w [kN/m]
SFRC Beam 4	11.90	17.63	17.58	1.93
SFRC Beam 5	11.83	17.53		
Combined Beam 4	9.48	14.04	14.06	1.87
Combined Beam 5	9.50	14.07		
RC Beam 4	9.41	13.94	13.50	1.88
RC Beam 5	8.82	13.07		

The applied force assumption made in the damage model resulted in a simplified average stiffness *(k_a)* for each beam type. This stiffness is shown schematically in Figure 62. It can be seen that the beam's stiffness before cracking *(k_e)* and during unloading *(k_u)* is higher than that assumed. This discrepancy is a shortcoming due to the non-linear behaviour of RC and SFRC.

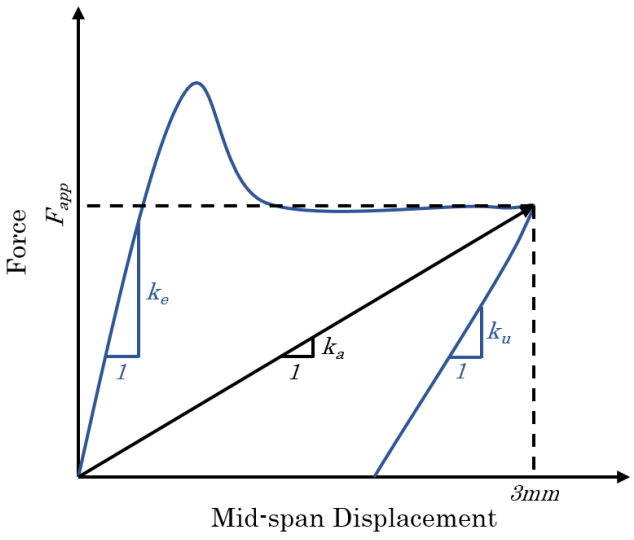

Figure 62: Beam stiffness comparisons.

Once each beam type's cracked elastic modulus had been solved, a damage factor *(ω)* was defined as:

$$E_c = E(1 - \omega) \tag{7-7}$$

where: E_c and E are the cracked and uncracked elastic moduli, respectively. The elastic moduli and damage factors, obtained with Equation (7-7), are presented in Table 23.

Table 23: Cracked concrete elastic moduli and damage factors for reinforced beam types.

Beam Type	E [GPa]	E_c [GPa]	Damage Factor
SFRC	37.50	7.24	0.807
Combined	37.50	5.74	0.847
RC	37.50	5.51	0.853

The damage factors obtained for the three different types of concrete beams were fairly similar. The damaging effect of pre-cracking was slightly larger on both the RC and combined beams than the SFRC beams.

7.1.2 Creep Load Model

The same approach, as used in the damage model in Section 7.1.1, was used in creating a creep load model. The main difference between the two models was the beam's loading. The damage model used a central point load *(F),* while the creep model has two point loads *(P),* each 250mm away from the mid-span. The beam model used for the creep load model can be seen in Figure 63. The beam's self-weight was again considered. Equations (7-1) to (7-4) were used to obtain the various relationships over the length of the beam.

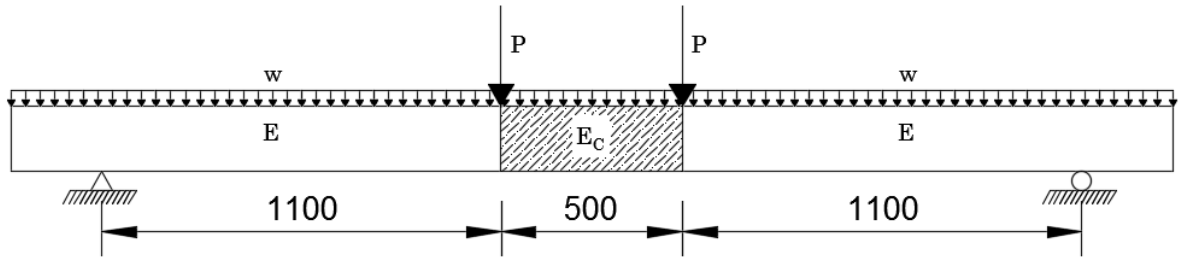

Figure 63: Beam model used for the creep load model.

The applicable boundary and continuity conditions were used to solve the constants arising from the integration method. The elastic curve equation obtained for section one of the creep beam model, $0 \leq x \leq 1100mm$:

$$\delta_1(x) = \frac{-\frac{wx^4}{24} + \frac{9wx^3}{40} + \frac{Px^3}{6} + \left(-\frac{1081wx}{4800} - \frac{11Px}{40}\right)\frac{E}{E_C} - \frac{7139wx}{12000} - \frac{121Px}{200}}{EI} \tag{7-8}$$

The equation obtained for section two of the creep beam model, $1100mm \leq x \leq 1350mm$:

$$\delta_2(x) = \frac{-\frac{wx^4}{24} + \frac{9wx^3}{40} + \frac{11Px^2}{20} - \frac{6561wx}{8000} - \frac{297Px}{200}}{E_C I} + \frac{\left(-\frac{1331w}{3200} - \frac{11891wE}{48000E_C} - \frac{1331P}{3000} - \frac{121PE}{400E_C}\right)\frac{E_C}{E} + \frac{1991w}{3000} + \frac{121P}{125}}{E_C I} \tag{7-9}$$

where: $\delta_i(x)$ is the vertical displacement of a beam section at a position x, w is the self-weight of the reinforced beam, P is the applied long-term load, E is the concrete's elastic modulus, E_c is the concrete's cracked elastic modulus, and I is the moment of inertia of the cross section with respect to y. A post-calculation check was performed to confirm the vertical displacement, at a value of $x = 1100mm$, was equal for both Equations (7-8) and (7-9).

Equation (7-9) was used along with the cracked modulus obtained in Section 7.1.1 to predict the long term deflections due to the sustained loading. The Age Adjusted Effective Modulus (AAEM) model was used to modify the elastic moduli value over time. This is discussed in greater detail in Section 7.2.

An initial comparison between the creep model predicted and measured instantaneous elastic displacements was made for each beam type. The self-weight was not included in the creep load model, as the first dial gauge readings already included the initial elastic displacement caused by the beam's self-weight. The measured instantaneous elastic displacement therefore only resulted from the sustained loading. The variables used in predicting the instantaneous elastic displacement of all the beam types are presented in Table 24.

Table 24: Parameters used to calculate instantaneous elastic displacement due to loading.

Beam Type	E [GPa]	E_c [GPa]	P [kN]	w [kN/m]
SFRC	37.50	7.24	4.87	0
Combined	37.50	5.74	4.17	0
RC	37.50	5.51	3.75	0

The elastic displacement values obtained for the creep model $(\delta_{e,s,mod})$, as well as the average measured values $(\delta_{e,s,exp})$ from Section 6.1.1, can be seen in Table 25. The model displacements were between 32% and 69% larger than the experimental values. This was however expected due to the average beam stiffness assumption made in the damage model. The gradient of the selected stiffness, was less than that of the beam's unloading stiffness. The reloading stiffness of each beam was expected to be similar to that of the unloading stiffness. The consistency of the results was therefore a positive outcome.

Table 25: Average instantaneous elastic displacements due to the sustained flexural load.

Beam Type	$\delta_{e,s,mod}$ [mm]	$\delta_{e,s,exp}$ [mm]
SFRC	1.30	0.77
Combined	1.35	0.93
RC	1.25	0.95

The largest difference in the instantaneous elastic displacement values was that of the SFRC. This additional difference is hypothesised to be the result of the unloading and reloading behaviour of SFRC. Research performed by Babafemi (2015) and Nieuwoudt (2016) investigated SFRC's reloading behaviour. This research is presented in Figure 64. Both investigations revealed that the reloading stiffness of SFRC is greater than its

unloading stiffness. This could therefore be an additional reason for the lesser measured instantaneous elastic displacement value.

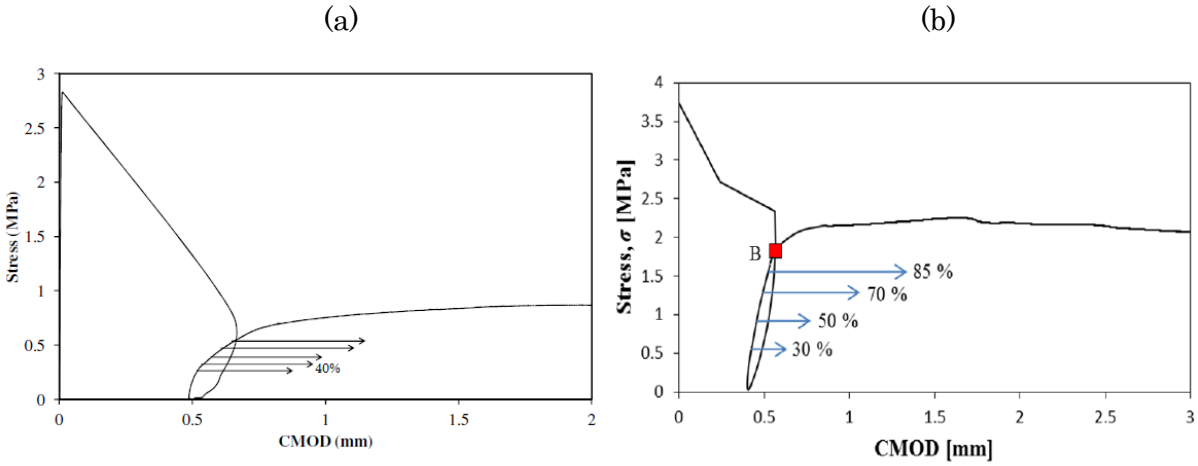

Figure 64: Unloading and reloading response of SFRC, (a) Babafemi (2015), (b) Nieuwoudt (2016).

7.2 Creep Deflection Prediction

7.2.1 *fib* AAEM Model

The *fib* Model Code (2010) was used for the prediction of creep of normal concrete. In this code, concrete is considered as an aging linear viscoelastic material. This is however only applicable at service stress levels less than or equal to 40%. At higher stresses concrete typically behaves non-linearly. On the basis of this assumption, the elastic modulus of concrete at any time *(t)*, and time of loading *(t_0)*, can be estimated with:

$$E_{eff}(t,t_0) = \frac{E}{1+\varphi_c(t,t_0)} \tag{7-10}$$

where: $E_{eff}(t,t_0)$ is the concrete's effective modulus of elasticity, E is the concrete's modulus of elasticity, and $\varphi_c(t,t_0)$ is the creep coefficient. The creep coefficient can be calculated from:

$$\varphi_c(t,t_0) = \varphi_{bc}(t,t_0)+\varphi_{dc}(t,t_0) \tag{7-11}$$

where: $\varphi_{bc}(t,t_0)$ is the basic creep coefficient, and $\varphi_{dc}(t,t_0)$ is the drying creep coefficient. The basic creep coefficient can be calculated with:

$$\varphi_{bc}(t,t_0) = \beta_{bc}(f_{cm})\cdot\beta_{bc}(t,t_0) \tag{7-12}$$

with

$$\beta_{bc}(f_{cm}) = \frac{1.8}{(f_{cm})^{0.7}} \tag{7-13}$$

$$\beta_{bc}(t,t_0) = \ln\left(\left(\frac{30}{t_{0,adj}} + 0.035\right)^2 \cdot (t-t_0) + 1\right) \tag{7-14}$$

with

$$t_{0,adj} = t_0 \cdot \left(\frac{9}{2 + t_0^{1.2}} + 1\right)^1 \tag{7-15}$$

where: f_{cm} is the mean compressive cylinder strength at 28 days. The drying creep coefficient of concrete may be estimated from:

$$\varphi_{dc}(t,t_o) = \beta_{dc}(f_{cm}) \cdot \beta(RH) \cdot \beta_{dc}(t_0) \cdot \beta_{dc}(t,t_0) \tag{7-16}$$

with

$$\beta_{dc}(f_{cm}) = \frac{412}{(f_{cm})^{1.4}} \tag{7-17}$$

$$\beta(RH) = \frac{1 - \frac{RH}{100}}{\sqrt[3]{0.1 \cdot \frac{h_c}{100}}} \tag{7-18}$$

$$\beta_{dc}(t_0) = \frac{1}{0.1 + {t_{0,adj}}^{0.2}} \tag{7-19}$$

$$\beta_{dc}(t,t_0) = \left(\frac{t-t_0}{\beta_h + (t-t_0)}\right)^{\gamma(t_0)} \tag{7-20}$$

with

$$\gamma(t_0) = \frac{1}{2.3 + \frac{3.5}{\sqrt{t_{0,adj}}}} \tag{7-21}$$

$$\beta_h = 1.5 \cdot h_c + 250 \cdot \alpha_{f_{cm}} \leq 1500 \cdot \alpha_{f_{cm}} \tag{7-22}$$

with

$$\alpha_{f_{cm}} = \left(\frac{35}{f_{cm}}\right)^{0.5} \tag{7-23}$$

where: RH is the relative humidity of the ambient environment, and the nominal size of the member $h_c = 2A_c/u$, where A_c is the concrete's cross-sectional area and u is the exposed perimeter in contact with the environment. The age of concrete is highly dependable on its temperature. The effect of elevated or reduced temperatures on the maturity of concrete can be taken into account by adjusting the appropriate concrete age with:

$$t_T \text{ or } t_{0,T} = \sum_{i=1}^{n} \Delta t_i \cdot exp\left(13.65 - \frac{4000}{273 + T(\Delta t_i)}\right) \quad (7\text{-}24)$$

where: t_T or $t_{0,T}$ are the temperature adjusted concrete ages which supersede t or t_0 used in the prior equations, Δt_i is the number of days that a temperature T prevails, and $T(\Delta t_i)$ is the temperature during the time period Δt_i.

7.2.2 Verification of RC Beam Creep Test

The *fib* AAEM model was applied to the creep load model for the RC beams. This was performed in order to verify the use of the *fib* model in this research. The *fib* model Equations (7-10) to (7-24) were used to modify the normal and cracked elastic moduli over time t. The beams were kept wrapped in wet blankets to aid curing. This meant that the average curing temperature of the concrete was unknown. For this reason three hypothetical average curing temperatures were used in the *fib* model, namely: 13°C, 16°C; and 19°C. The temperature in the climate controlled room remained constant at 22°C for the 120 days of testing. These temperature readings were used in adjusting the concrete's age with Equation (7-24). The beam's total perimeter was used in calculating h_c, as all the sides were exposed to the environment. The 28 day NC compressive cube strength obtained in Section 5.1 was multiplied by a factor of 0.8 in order to obtain the equivalent cylindrical strength (BS EN 1992-1-1, 2004). Table 26 summarises the values used in the RC beams' *fib* model.

Table 26: Variables used for the RC beams in the *fib* AAEM model.

	f_{cm} [MPa]	t_0 [days]	RH	h_c [mm]
RC Beams	34.1	49	55%	128.6

The reference mid-span displacement, due to the sustained load and distributed load, was calculated using the initial cracked and uncracked elastic moduli, see Table 27. Intervals of 2 days were then used in the time-dependent creep coefficient and applied to both the cracked and uncracked elastic moduli. The vertical mid-span displacement was solved, using Equation (7-9), for each effective elastic moduli. The reference displacement was then subtracted from this value to calculate the resultant displacement due to creep.

Table 27: Initial elastic moduli and long-term loads used to model the RC beam creep test.

	E [GPa]	E_c [GPa]	P [kN]	w [kN/m]
RC Beams	37.50	5.51	3.75	1.88

The resulting curve was plotted for each hypothetical curing temperature, along with the physical cracked reinforced beam creep results. The curves obtained are presented in Figure 65.

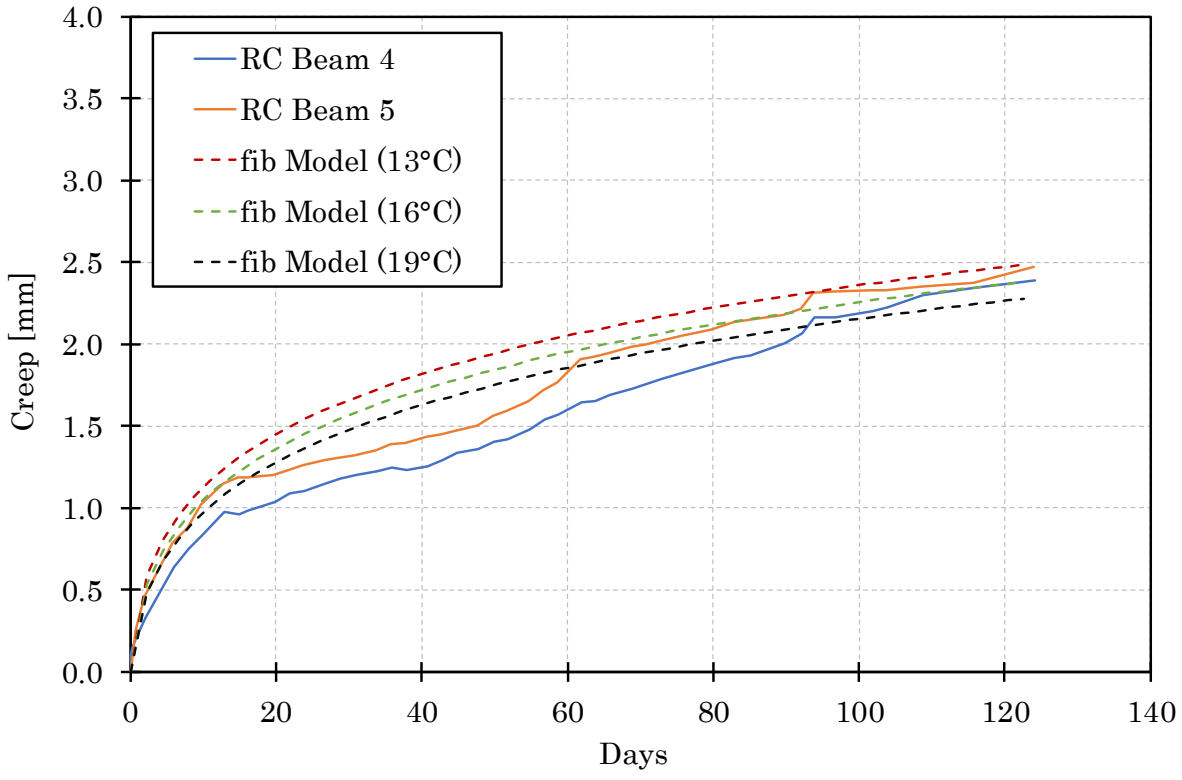

Figure 65: Creep results of both the physical and modelled cracked RC beams.

The results obtained with the use of the *fib* and creep load models accurately predicted the creep of the RC beams. The hypothetical curing temperature of 16°C was found to be

the best fit for the model. As the beams were cured in late autumn, this value was a good representative of the average expected temperature. The 16°C curing temperature was therefore assumed for both the SFRC and the combined beams. The use of the *fib*'s AAEM method for creep deflection prediction in this research was thus verified.

7.3 Constitutive Creep Model of SFRC and Combined Beams

7.3.1 *fib* AAEM Model Adaption to Include Pull-out Creep Behaviour

An additional creep coefficient factor for the fibre pull-out creep of cracked SFRC is proposed. The use of this factor works on the same principle of that used in the AAEM method. Specifically, the factor is used to furthermore reduce the elastic modulus of cracked SFRC, in order to take into account the increased creep.

The CMODs obtained from the uniaxial tensile creep tests in Section 6.3 were used in calibrating the factors for each steel fibre dosage. A power trendline was plotted for each CMOD curve, as presented in Figure 66. This allowed the prediction of the CMOD due to fibre pull-out creep *($CMOD_{fpc}$)*, as a function of time.

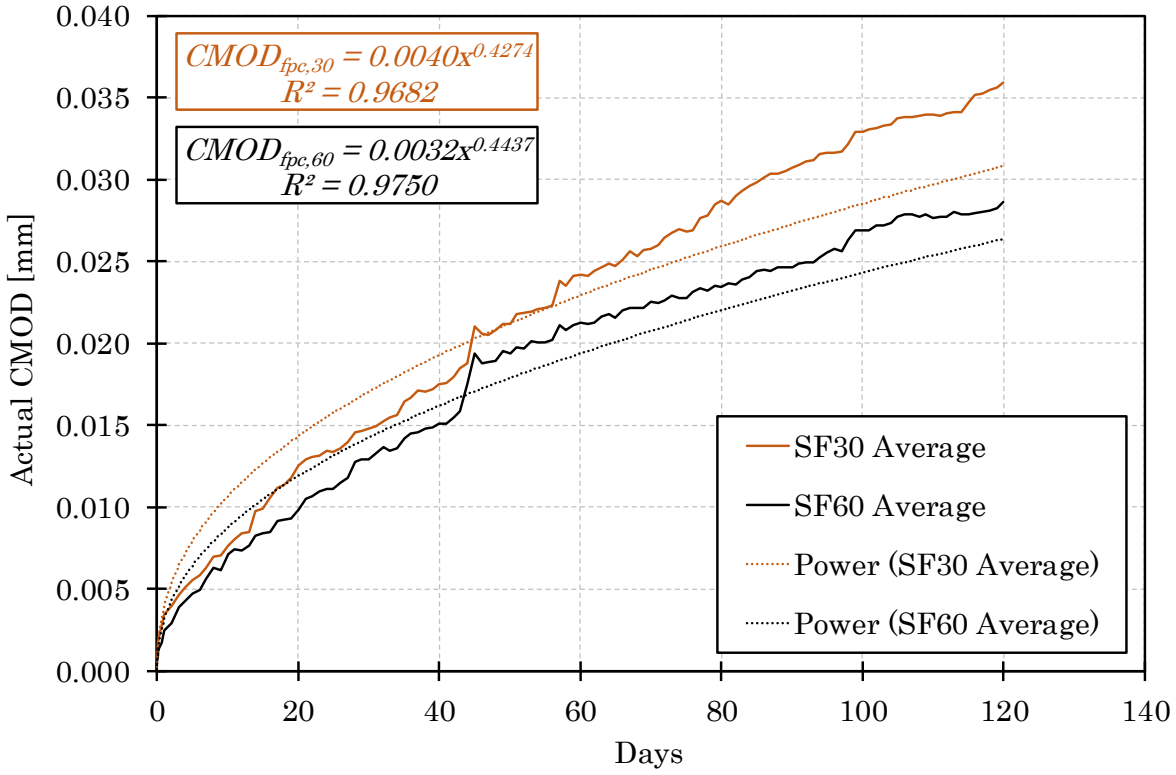

Figure 66: Power equations obtained for the rate of CMOD due to fibre pull-out.

The regression values demonstrated a favourable fitted response for both trendlines. The fit is expected to improve with time as the specimens reach an expected asymptotic creep response. Each fibre pull-out creep coefficient was calibrated by dividing the $CMOD_{fpc}$ equations by uniaxial tensile creep CMOD values obtained in Section 6.3. These values included: the permanent CMOD due to pre-cracking $(CMOD_p)$, the instantaneous elastic CMOD due to the sustained loading $(CMOD_{e,s})$, and a combination of the two. It was found that average instantaneous elastic CMOD provided the best results. For this reason the fibre pull-out creep coefficient $\varphi_{fpc}(t,t_0)$ is presented as:

$$\varphi_{fpc}(t,t_0) = \frac{CMOD_{fpc}(t,t_0)}{CMOD_{e,s}} \tag{7-25}$$

where: $CMOD_{fpc}(t,t_0)$ is the rate of fibre pull-out creep, in which $(t_T - t_{0,T}) = x$. The adapted *fib* AAEM model is therefore presented as:

$$E_{c,eff}(t,t_0) = \frac{E_c}{1 + \varphi_C(t,t_0) + \varphi_{fpc}(t,t_0)} \tag{7-26}$$

where: $E_{c,eff}(t,t_0)$ is the cracked SFRC effective modulus of elasticity, E_c is the cracked SFRC modulus of elasticity; $\varphi_c(t,t_0)$ is the conventional creep coefficient, and $\varphi_{fpc}(t,t_0)$ is the fibre pull-out creep coefficient.

Equations (7-10) to (7-26) were used to modify the normal and cracked elastic moduli over time t. Table 28 summarises the values used in the SFRC and combined beam's *fib* model.

Table 28: *fib* AAEM model variables used for the SFRC and combined beams.

Beam Type	f_{cm} [MPa]	t_0 [days]	RH	h_c [mm]	Curing Temp.
SFRC	40.8	49	55%	128.6	16°C
Combined	36.7	49	55%	128.6	16°C

The same method used in Section 7.2.2 was applied in calculating the resultant displacement due to creep. Intervals of 2 days were again used in the time-dependent creep coefficient and applied to both cracked and uncracked elastic moduli. It must be stressed that the adapted model, i.e. Equation (7-26), was only applied to the cracked concrete's elastic modulus. Table 29 presents the variables used in the creep load model.

Table 29: Initial elastic moduli and long-term loads used to model the SFRC and combined beam creep tests.

Beam Type	E [GPa]	E_c [GPa]	P [kN]	w [kN/m]
SFRC	37.50	7.24	4.87	1.93
Combined	37.50	5.74	4.17	1.87

The creep curves were plotted for the current *fib* model, the proposed adapted model, and the physical cracked reinforced beam creep results. The curves acquired for the SFRC beams are presented in Figure 67.

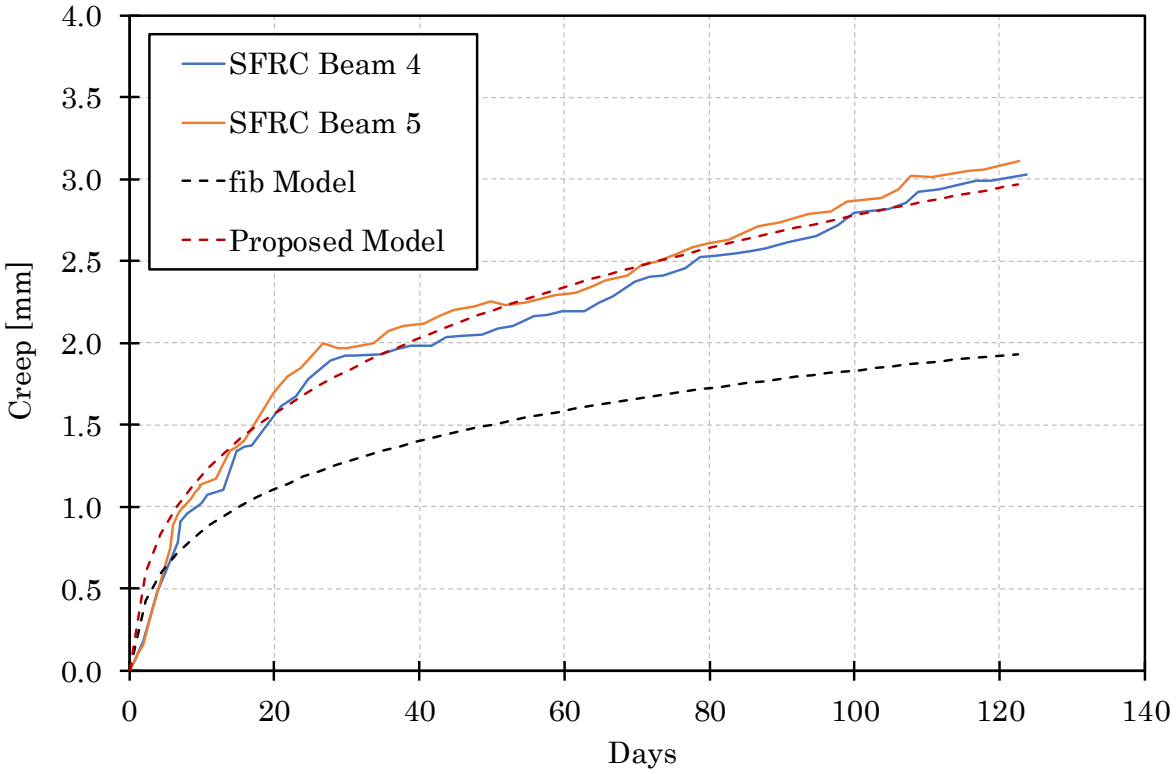

Figure 67: Creep results of the physical and modelled cracked SFRC beams.

Figure 67 demonstrates the inaccurately of the current *fib* model in predicting the creep of SFRC. The proposed adapted model however, showed an excellent estimation of the total creep experienced by both SFRC beams. A creep increase of 53% at 120 days was calculated, due to the additional fibre pull-out behaviour of SFRC. This validates the importance of taking this behaviour into account.

Table 30 presents the long-term predicted creep deflections for both the current *fib* model and the proposed adapted model. The increase due to the additional fibre pull-out creep is also displayed. It can be seen that the time-dependent behaviour of SFRC increases significantly as time progresses.

Table 30: Predicted creep defections for the SFRC beams.

	SFRC Beam's Predicted Creep Deflections		
	fib Model [mm]	Proposed Model [mm]	% Increase
1 Year	2.47	4.14	68%
5 Years	3.12	6.55	110%
10 Years	3.34	7.99	140%
30 Years	3.63	11.22	209%

The two physical creep curves as well as the *fib* and proposed adapted model of the combined beams, are presented in Figure 68.

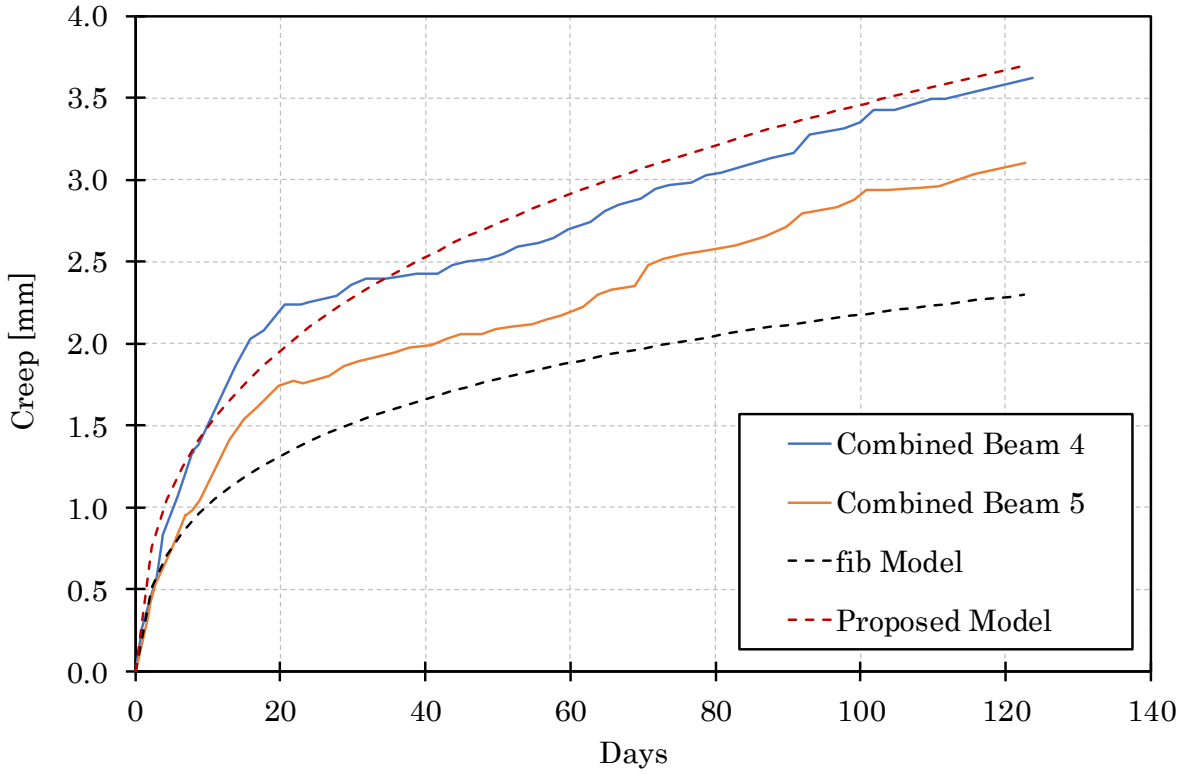

Figure 68: Creep results of the physical and modelled cracked combined beams.

A creep increase of 38% at 120 days, between the *fib* model and the proposed model, was calculated. The proposed model accurately predicted the creep of Combined Beam 4, but was less accurate for Combined Beam 5. This disparity however, can be expected from a material as variable as SFRC. The encouraging detail of this was that the proposed model did not underestimate the measured creep.

The long-term creep deflections for the combined beams are presented in Table 31. The *fib* model and proposed model predictions, along with the increase due to fibre pull-out are shown. The increases observed in the combined beams are similar to those obtained by the SFRC beams.

Table 31: Predicted creep defections for the combined beams.

	Combined Beam's Predicted Creep Deflections		
	fib Model [mm]	Proposed Model [mm]	% Increase
1 Year	2.94	5.16	76%
5 Years	3.72	8.15	119%
10 Years	3.97	9.93	150%
30 Years	4.32	13.85	221%

The models presented in this chapter show that it is possible to introduce a creep coefficient factor to include the fibre pull-out behaviour of cracked SFRC. It is however noted that this is simply a preliminary model and that considerably more research is required in order to verify this method. Factors including different loading conditions, fibre dosages and reliability still need to be addressed. The results presented in this chapter however, show that ultimately introducing a design method for predicting the long-term deflections of SFRC is achievable.

7.4 Concluding Summary

In this chapter the models used to predict the creep of cracked SFRC were presented. The models were based on the Bernoulli–Euler beam theory, the current *fib* Model Code's AAEM, and the results of Chapters 5 and 6. A damage model was created to quantify the impact of pre-cracking on each beam type. This model was then modified into the creep load model, in order to calculate the displacements due to the sustained flexural loading.

The use of the current *fib* model in this research was also verified for reinforced concrete. An adapted model to include the behaviour of fibre pull-out was then proposed. This model was calibrated using the uniaxial tensile creep results in Chapter 6. The adapted model accurately predicted the creep of both the SFRC and combined beams.

Chapter 8

Conclusions and Recommendations

8.1 Conclusions

An investigation of the mechanical and time-dependent behaviour of SFRC was performed in this research study. The uniaxial tensile and flexural creep behaviour of SFRC under a sustained load of 40% of the maximum applied loading was examined. The results obtained in these tests were used to develop a design model predicting the time-dependent behaviour of cracked SFRC in flexure.

The conclusions drawn from the experimental investigations made in this study are presented in the following sections.

8.1.1 Mechanical Behaviour

- The notched beam tests provided tensile design values expected of SFRC. The residual tensile strength values obtained were however highly variable, shown by the large coefficient of variances (>20%). This indicated that substantial variations in fibre distribution were present in the notched beam specimens.
- The RC beams performed satisfactorily in the reinforced beams tests and demonstrated the flexural behaviour predicted by BS EN 1992-1-1 (2004).
- Both the SFRC and combined beam specimens obtained maximum bending moments lower than that designed for in the *fib* Model Code (2010). This indicates that the notched beams were not good representations of the tensile resistances obtained for both the SFRC and combined beams.
- The SFRC and combined beams displayed lower ductility than the RC beams, as was presented in the cracking patterns.

8.1.2 Time-dependent Behaviour

- The SFRC, RC and combined beams obtained average flexural creep deformations of 3.07mm, 2.43mm and 3.36mm respectively after 4 months of loading. It can therefore be concluded that similarly designed beams obtain 26% larger creep deflections than RC, if SFRC is used. This value is 38% for a beam with a combination of steel reinforcements.
- The increase in average CMOD, obtained after 4 months, in comparison to the average instantaneous elastic CMOD was 80% and 105% for the SF60 and SF30 mixes respectively. It can therefore be deduced that the extra 30kg/m^3 of extra fibres present in the SF60 mix resulted in an overall reduction of 25% in fibre pull-out creep.

8.1.3 Time-dependent Modelling

- The *fib* Model Code's AAEM method successfully predicted the creep of the cracked RC beams.
- A preliminary design model for the prediction of cracked SFRC was obtained. This model was generated using a combination of three models, namely: a damage model, an adjusted *fib* model, and a creep load model. The damage model successfully calculated cracked elastic modulus and damage factors used to quantify the effects of flexural pre-cracking. The *fib's* current model for predicting of creep of normal concrete, by reducing the concrete's elastic modulus, was adjusted to include the fibre pull-out behaviour of cracked SFRC. This model was calibrated using the results obtained in the uniaxial tensile creep tests. The time-dependent elastic moduli was used in the creep load model in order to calculate the cracked SFRC creep deformations due to the sustained loading.

8.2 Recommendations for Future Work

From the results and insights obtained during this research project, the following aspects are recommended for further investigation.

- In Chapter 5 it was hypothesised that the SFRC notched beam casting procedure used, i.e. a poker vibrator, was the primary reason for the large coefficient of variance values obtained. It would thus be worthy to conduct an investigation into the effect of different casting procedures on the coefficient of variance values, as well as the fibre distributions and orientations obtained at the notched beam's crack.

- The SFRC and combined beams in this study both obtained experimental bending moments less than those predicted in the flexural design model. The tensile resistance obtained in the notched beam tests were thus not good representations of those obtained in the reinforced beam tests. It is anticipated that the different cross-sectional properties of the beams influenced the tensile resistances. It would therefore be advised for future studies to investigate this effect and introduce a possible factor to account for this discrepancy.

- Chapter 7 presented a preliminary design model predicting the time-dependent behaviour of cracked SFRC beams in flexure. This model however is only applicable to SFRC beams with the loadings presented in this research. It would therefore be valuable to test the method of obtaining the design model with varied factors such as, loading conditions, sustained load levels, and fibre dosages.

This research study found that the adapted AAEM method can accurately predict the long-term deflections for SFRC and combined beams. The recommendations are provided to refine the study in future.

References

ASTM E8/E8M. 2013. Standard Test Methods for Tension Testing of Metallic Materials. *An American National Standard*. (C):1–27.

Atrushi, D.S. 2003. Tensile and Compressive Creep of Early Age Concrete: Testing and Modelling. The Norwegian University of Science and Technology.

Babafemi, A.J. 2015. Tensile Creep of Cracked Macro Synthetic Fibre Reinforced Concrete. University of Stellenbosch.

Bentur, A. 1991. Microstructure, interfacial effects and micromechanics of cementitious composites. In *Advances in Cementitious Materials*. 523–547.

Bentur, A. & Mindess, S. 2007. *Fibre Reinforced Cementitious Composites*. Second ed.

Van Bergen, S., Pouillon, S., et al. 2016. Experiences From 14 Years of Creep Testing of Steel and Polymer Fiber Reinforced Concrete. *International RILEM Workshop on creep behaviour in cracked section of Fibre Reinforced Concrete*. (March).

BS EN 12350-2. 2009. Testing fresh concrete. Slump-test. *British Standards Institute*.

BS EN 12390-13. 2013. Testing hardened concrete. Part 13: Determination of the secant modulus of elasticity in compression. *British Standards Institute*.

BS EN 12390-3. 2002. Testing hardened concrete. Part 3: Compressive strength of test specimens. *British Standards Institute*.

BS EN 14651. 2005. Test method for metallic fibred concrete — Measuring the flexural tensile strength (limit of proportionality (LOP), residual). *British Standards Institute*. 3:1–17.

BS EN 1992-1-1. 2004. Eurocode 2: Design of concrete structures. Part 1-1: General rules and rules for buildings. *British Standards Institute*.

BS ISO 1920-8. 2009. Testing of concrete - Part 8: Determination of drying shrinkage of concrete for samples prepared in the field or in the laboratory. *British Standards Institute*.

Cunha, V. 2010. Steel fibre reinforced self-compacting concrete - from micro-mechanics to composite behaviour. University of Minho.

Fantilli, A.P., Mihashi, H., et al. 2009. Multiple cracking and strain hardening in fiber-reinforced concrete under uniaxial tension. *Cement and Concrete Research*.

fib. 2010. *Model Code 2010 First Complete Draft Volume 1*. International Federation for Structural Concrete.

Garcia-Taengua, E., Llano-Torre, A., et al. 2016. Effect of residual strength parameters on FRC flexural creep: Multivariate analysis. *International RILEM Workshop on creep behaviour in cracked section of Fibre Reinforced Concrete*. (March).

Ghoddousi, P., Ahmadi, R., et al. 2010. Fiber pullout model for aligned hooked-end steel fiber. *Canadian Journal of Civil Engineering*. 37:1179–1188.

Gilbert, R.I. & Nejadi, S. 2004. An Experimental Study of Flexural Cracking in Reinforced Concrete Members Under Sustained Loads. The University of New South Wales.

Gustavo J. 2005. High-performance fiber-reinforced cement composites: An alternative for seismic design of structures. *ACI Structural Journal*. 102(5):668–675.

Jarratt, R. 2011. Construction of In-situ Cast Flat Slabs using Steel Fibre Reinforced Concrete. University of Stellenbosch.

Kusterle, W. 2016. Flexural Creep Tests on Beams - 8 Years of Experiance with Steel and Synthetic Fibres. *International RILEM Workshop on creep behaviour in cracked section of Fibre Reinforced Concrete*. (March).

Löfgren, I. 2005. Fibre-reinforced Concrete for Industrial Construction - a fracture mechanics approach to material testing and structural analysis. Chalmers University of Technology.

Mouton, C.J. 2012. Investigating the tensile creep of steel fibre reinforced concrete. University of Stellenbosch.

Nakov, D., Markovski, G., et al. 2016. Creeping effect of SFRC elements under specific type of long term loading. *International RILEM Workshop on creep behaviour in cracked section of Fibre Reinforced Concrete*. (March).

Neville, A.M. 1970. *Creep of concrete: Plain, reinforced, and prestressed*. North Holland Publishing Company.

Nieuwoudt, P.D. 2016. Time-dependent Behaviour of Cracked Steel Fibre Reinforced Concrete. University of Stellenbosch.

Nieuwoudt, P.D., Babafemi, A.J., et al. 2017. The response of cracked steel fibre reinforced concrete under various sustained stress levels on both the macro and single fibre

level. *Construction and Building Materials*. 156:828–843.

Ou, Y., Tsai, M., et al. 2012. Compressive Behavior of Steel-Fiber-Reinforced Concrete with a High Reinforcing Index. *Journal of Materials in Civil Engineering*. 24(2):207–215.

RILEM TC 162-TDF. 2002. Test and design methods for steel fibre reinforced concrete. *Materials and Structures*. 35(249):262–278.

Robberts, J.M. & Marshall, V. 2010. *Analysis and Design of Concrete Structures*. Nuclear Structural Engineering.

Robins, P., Austin, S., et al. 2002. Pull-out behaviour of hooked steel fibres. *Materials and Structures*. 35(251):434–442.

SANS 6892-1. 2010. Metallic materials - Tensile testing Part 1 - Method of test at room temperature. *South African Bureau of Standards*.

Swamy, R.N. & Mangat, P.S. 1974. Inluence of fiber geometry on the properties of steel fiber reinforced concrete. *Cement and Concrete Research*. 4:451–465.